

Contents

1	Introduction	4
2	Pixel detectors	5
3	1.1 Signal formation	5
4	1.2 Charge Coupled Devices	7
5	1.3 Hybrid pixels	7
6	1.4 CMOS MAPS and DMPAS	9
7	1.4.1 DMAPS: large and small fill factor	10
8	1.4.2 A modified sensor	11
9	1.5 Analog front end	13
10	1.5.1 Preamplifier	13
11	1.6 Readout logic	14
12	Use of pixel detectors	17
13	2.1 Tracking in HEP	17
14	2.1.1 Hybrid pixels at LHC and at SuperKEKB	18
15	2.1.2 First attempts to MAPS	21
16	2.2 Other applications	23
17	2.2.1 Applicability to FLASH radiotherapy	24
18	TJ-Monopix1	29
19	3.1 The sensor	30
20	3.2 Front end	32
21	3.2.1 ALPIDE-like	33
22	3.3 Readout logic	34
23	Arcadia-MD1	38
24	4.1 The sensor	38
25	4.1.1 Two different FE flavor	39
26	4.2 Readout logic and data structure	39
27	4.2.1 Matrix division and data-packets	39
28	Characterization	43
29	5.1 TJ-Monopix1 characterization	43
30	5.1.1 Threshold and noise: figure of merit for pixel detectors	43
31	5.1.2 Linearity of the ToT	47
32	5.1.3 Calibration of the ToT	48
33	5.1.4 Changing the bias	52

35	5.1.5 Measurements with radioactive sources	53
36	5.1.6 Dead time measurements	56
37	5.2 ARCADIA-MD1 characterization	57
38	6 Test beam measurements	62
39	6.1 Apparatus description	62
40	6.1.1 Accelerator	62
41	6.1.2 Mechanical carriers	64
42	6.2 Measurements	65
43	Bibliography	69
44	Characterization of monolithic CMOS pixel sensors for charged particle detectors and	
45	for high intensity dosimetry	

⁴⁶ Introduction

⁴⁷ Since the 1980s, when the fabrication of device with very small electrodes (50-100 μm)
⁴⁸ became a practical possibility, pixel detectors have been widely employed for imaging and
⁴⁹ tracking charged particles in the vertex region of experiments at accelerators. Thanks to
⁵⁰ their excellent spatial resolution, today even better than 10 μm , they allow for true three
⁵¹ dimensional space-point determination even at high particle fluxes and in particular for
⁵² the identification of secondary vertices of short-lived particles such as τ and B mesons.
⁵³ Requirement imposed by accelerators are stringent and they will become even more so
⁵⁴ with the increase of luminosity; in this scenario CMOS Monolithic Active Pixel Sensors
⁵⁵ (MAPS), based on the technology of CMOS cameras, are being developed to improve
⁵⁶ the performance of the hybrid pixel detectors, which currently constitute the state-of-art
⁵⁷ for large scale pixel detector, in particular by reducing the amount of material, power
⁵⁸ consumption and pixel dimension. Indeed, while hybrid pixels are made by two parts, the
⁵⁹ sensor and the electronics, welded together through microconnections, the MAPS integrate
⁶⁰ them all on the same wafer.

⁶¹ Experiments such as ALICE at LHC and STAR at RHIC have already introduced the
⁶² CMOS MAPS technology in their detectors. ALICE Tracking System (ITS2), upgraded
⁶³ during the LHC long shut down in 2019-20, was the first large-area ($\sim 10 \text{ m}^2$) silicon vertex
⁶⁴ detector based on CMOS MAPS. Thanks to the reduction of the material budget, ITS2,
⁶⁵ which uses the ALPIDE chip developed by ALICE collaboration, obtained an amazing im-
⁶⁶ provement both in the position measurement and in the momentum resolution, improving
⁶⁷ the efficiency of track reconstruction for particle with very low transverse momentum (by
⁶⁸ a factor 6 at $p_T \sim 0.1 \text{ GeV}/c$). Further advancements in CMOS MAPS technology are
⁶⁹ being aggressively pursued for the ALICE ITS3 and the Belle II vertex detector upgrades
⁷⁰ (both foreseen around 2026-27), and by the R&D53 collaboration for the upgrade at HL-
⁷¹ LHC, with the goals of further reducing the sensor thickness and improving the readout
⁷² speed of the devices, while keeping power consumption at a minimum.

⁷³ Beside tracking, the development of pixel detectors is a very active field with many
⁷⁴ applications: a noteworthy example of detector originally used in particle physics and later
⁷⁵ employed for medical imaging, in space detectors and for art authentication, is Medipix,
⁷⁶ a hybrid system developed at CERN within the Medipix collaboration. Among medical
⁷⁷ applications, a possible use of CMOS MAPS could be in dosimetry: in the last few years
⁷⁸ the search of radiotherapy oncological treatments with high intensity beams (FLASH
⁷⁹ mode) is requiring new dosimeters, both for the therapies as well as new beam-monitors
⁸⁰ (especially for focused very high energy electron beams), which are capable of deal with
⁸¹ extreme dose rate (up to 40 Gy/s).

⁸² I have studied the characteristics of two ALPIDE-like CMOS MAPS chips and tested
⁸³ them under different front end configuration. The first chip, the TJ-Monopix1 from the
⁸⁴ Monopix series, is a TowerJazz MAPS fabricated in 180 nm CMOS technology with an

active area of $1 \times 2 \text{ cm}^2$ (448×224 pixels) and is one of the prototypes for the Belle II vertex detector upgrade. The second chip, called Main Demonstrator-1, has an active area of $1.28 \times 1.28 \text{ cm}^2$ (512×512 pixels) is produced by LFoundry in 110 nm CMOS technology and designed by the ARCADIA (Advanced Readout CMOS Architectures with Depleted Integrated sensor Arrays) group; it is intended to be a general purpose device with possible use in medical scanners, space experiments, future lepton colliders and also possibly X-ray applications with thick substrates. The main differences between the two chips are in the output signal type and in the readout sequence of the matrix. Concerning the former, TJ-Monopix1 returns an analog output information, that is the time over threshold of the pulse, which can be related with the charge released by the particle in the sensor, while MD1 returns only a digital information; regarding the latter, instead, TJ-Monopix1 has a completely sequential readout, while MD1 roughly combines the information of the hits before the readout in order to reduce the data transmission time.

I have set up the test systems for the two chips in the INFN clean laboratories and characterized the devices electrically and with radioactive sources in terms of threshold, noise, dead time and analog response. The mean minimum stable threshold evolved through different generation of chips and nowadays it is less than 500 e^- , allowing thinner sensors with smaller signals: TJ-Monopix1 has proven to be in agreement with this trend, having a threshold of $\sim 400 \text{ e}^-$, to be compared with the 2000 e^- signal expected for a minimum ionizing particle in an epitaxial layer of $25 \mu\text{m}$. Moreover, since one of the main challenges of MAPS are the differences between pixels due to process parameters variation across the wafer, which make the sensor response nonuniform, I have measured the threshold and noise dispersion across the matrix, which I found to be 40 e^- and 2 e^- respectively. I have also studied the response of the analog signal recorded by TJ-Monopix1, that is the time over threshold, and performed a calibration of its absolute value using a Fe55 X-ray source. All these measurements are important to verify the design parameters of the chip and to validate the chip simulation.

As conclusion of the measurement campaign, we have tested TJ-Monopix1 at very high intensity using the electron beam of the new ElectronFlash accelerator designed for both medical research and R&D in FLASH-radiotherapy and recently installed at Santa Chiara hospital in Pisa. I have participated in the design of the setup needed for testbeam measurement and I am currently working on the analysis of the data collected.

¹¹⁷ **Chapter 1**

¹¹⁸ **Pixel detectors**

¹¹⁹ Pixel detectors are semiconductor detectors which are segmented in two dimensions: this
¹²⁰ distinguish them from the strip detectors, such that a single plane of detector already
¹²¹ provides both the coordinates of impact of the detected particle. Their operation is based
¹²² on the p-n junction (fig. 1.1). A p-n junction is built by bringing in contact two n
¹²³ and p doped silicon crystals. At the boundary, recombination of both charge carriers
¹²⁴ occurs forming a region, the depletion zone, which is free of charge carriers. The charged
¹²⁵ donors⁺ and acceptor⁻, that remain ionised in the n-type and p-type regions, features a
¹²⁶ space charge and create an electric field across the junction, causing a drift current in the
¹²⁷ opposite direction to the diffusion one, through which the junction reaches an equilibrium
¹²⁸ state. Assuming a constant space change, the electric field is linear and reach a maximum
¹²⁹ at the boundary of the *p* and *n* layers.

¹³⁰ **1.1 Signal formation**

¹³¹ When a charged particle passes through a pixel and loses energy by ionization only a
¹³² part of that energy is used to generate electron-hole pairs, since another part is used for
¹³³ other processes, as lattice excitation. The average energy needed to create a pair at 300 K
¹³⁴ in silicon is $w_i = 3.65 \text{ eV}$, that is more than the mean ionization energy because of the
¹³⁵ interactions with phonon, since for a minimum ionizing particle (MIP) the most probable
¹³⁶ value (MPV) of charge released in the semiconductor is $0.28 \text{ keV}/\mu\text{m}$, hence the number
¹³⁷ of electrons-vacuum pairs is:

$$\langle \frac{dE}{dx} \rangle \frac{1}{w_i} \sim 80 \text{ e/h} \sim \frac{1.28 \cdot 10^{-2} fC}{\mu\text{m}} \quad (1.1)$$

¹³⁸ Because of the splitting of the energy depositon between the two different processes, the
¹³⁹ number $N_{e/h}$ of couples generated undergoes fluctuations that usually follow a Poisson
¹⁴⁰ distribution; thus the fluctuations of $N_{e/h}$ is equal to $\sigma_{e/h} = \sqrt{N_{e/h}}$. Under the constraint
¹⁴¹ of complete absorption of a particle, the energy resolution improves of a factor \sqrt{F} , where
¹⁴² F is called the Fano factor and determines the ultimate limit of energy resolution for
¹⁴³ semiconductors. F is a function of the material and temperature and for silicon is equal
¹⁴⁴ to ~ 0.115 .

¹⁴⁵ In order to avoid a loss signal, it is fundamental that pairs e/h are produced in the
¹⁴⁶ depleted region of the semiconductor, where the probability of recombination with charge
¹⁴⁷ carriers is low. For this reason pixel detectors are commonly reverse biased: a positive
¹⁴⁸ bias is given to the *n* electrode and a negative to the *p* in order to grow the depletion zone

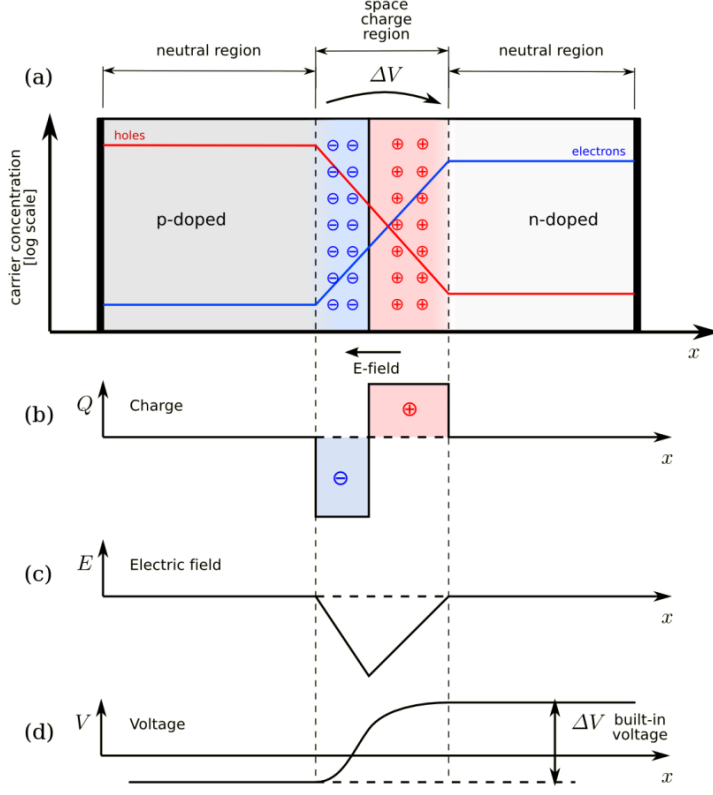


Figure 1.1: The structure of a p-n junction. (a) structure, (b) space charge density, (c) electric field distribution and (d) potential distribution.

in the epitaxial layer within the bulk. The width of the depletion region depends on the external bias V_{ext} , the resistivity ρ and also with the dopant:

$$d_n \sim 0.55 \sqrt{\frac{\rho}{\Omega cm} \frac{V_{ext}}{V}} \mu m \quad d_p \sim 0.32 \sqrt{\frac{\rho}{\Omega cm} \frac{V_{ext}}{V}} \mu m \quad (1.2)$$

Thus, high resistivity wafers ($100 \Omega cm - k\Omega cm$) are typically preferred because they allow bigger depletion zone with smaller voltage bias.

The charges created within the sensor are separated by an electric field and collected at their respective electrodes (p for holes and n for electrons)¹; by the drift of these charges, a signal i_e is generated on the electrode e as stated by the Shockley-Ramo's theorem:

$$i_e(t) = -q v(t) E_{WF,e} \quad (1.3)$$

where $v(t)$ is the instantaneous velocity of the charge q and E_{WF} is the weighting field, that is the field obtained biasing the electrode e with 1V and all the others with 0V. The drift velocity of the charge depends on the electric field and on the mobility of the particle:

$$v = \mu(E) E \quad (1.4)$$

where $\mu(E)$ is a function of the electric field and is linear in E only for small E : at higher values the probability of interactions with optical phonons increases, the mobility drops

¹Even if in principle both the electrode can be used to read the signal, for pixel detectors, where the number of channel and the complexity of readout are high, only one is actually used. In strip and pad detectors, instead, is more common a dual-side readout

and this leads to a saturation of the velocity (fig. 1.2). Typical values for electrons and holes mobility in silicon at room temperature are $\mu_n \sim 1450 \text{ cm}^2/\text{Vs}$, $\mu_h = 500$.

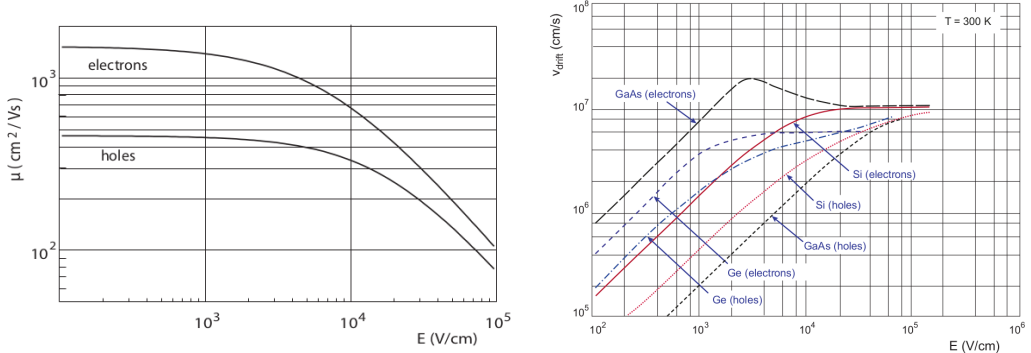


Figure 1.2: (a) Dependence of the mobility on the electric field. (b) Drift velocity at room temperature in different semiconductors

1.2 Charge Coupled Devices

In CCDs the charge is created in a very thin active epitaxial layer (typically 10 μm , maximally about 30 μm) and then locally stored in a potential minimum which is created by a MOS structure. The size of the CCD cells is typically in the range 10 μm to 20 μm such that spatial resolutions are of the order of a few micrometres. The collected charges are moved stepwise from electrode to electrode (thus so called 'bucket chain') by applying a potential with a clock with frequency of \sim MHz; despite of such high frequency, the readout chain is completely sequential and this makes the entire process comparatively slow (tens of ms). A particular type of CCD, the pnCCDs, are typically used to detect low energy (<10 keV) x-ray photons for their homogeneous spatial detection efficiency of photons. The pnCCDs have a sideward depletion similar to silicon drift chambers that makes the electric field stronger, compared with the normal CCDs. The pnCCDs designed for photon imaging are often fabricated with high Z materials, to increase absorption efficacy.

1.3 Hybrid pixels

Hybrid pixels, which currently are the state-of-art technology for large scale pixel detectors in most particle physics experiments, are made of two parts welded together through microconnection (bump bond): the sensor and the electronics (fig. 1.3a). They provide a practical system where the sensor and the ASIC (application specific integrated circuit) can be optimized separately, which makes them really fast, capable of handling with rate up to GHz. However a disadvantage of hybrid pixels is that they must be connected before testing. For reasons related with the historical development, the n⁺-in-n sensors were the first to be used; they demanded double-sided processing which guarantees the detector functionality both before and after the type inversion of the n⁻ doped bulk into p-type after high quantity of radiation. The pn-diode is initially on the unstructured backside of the sensor, while after, the depletion zone grows from the electrode side into the bulk. This ensures that the signal can be sensed on the pixels even if the substrate is no longer fully depleted, even though the bias voltage required for a sufficient depletion increases,

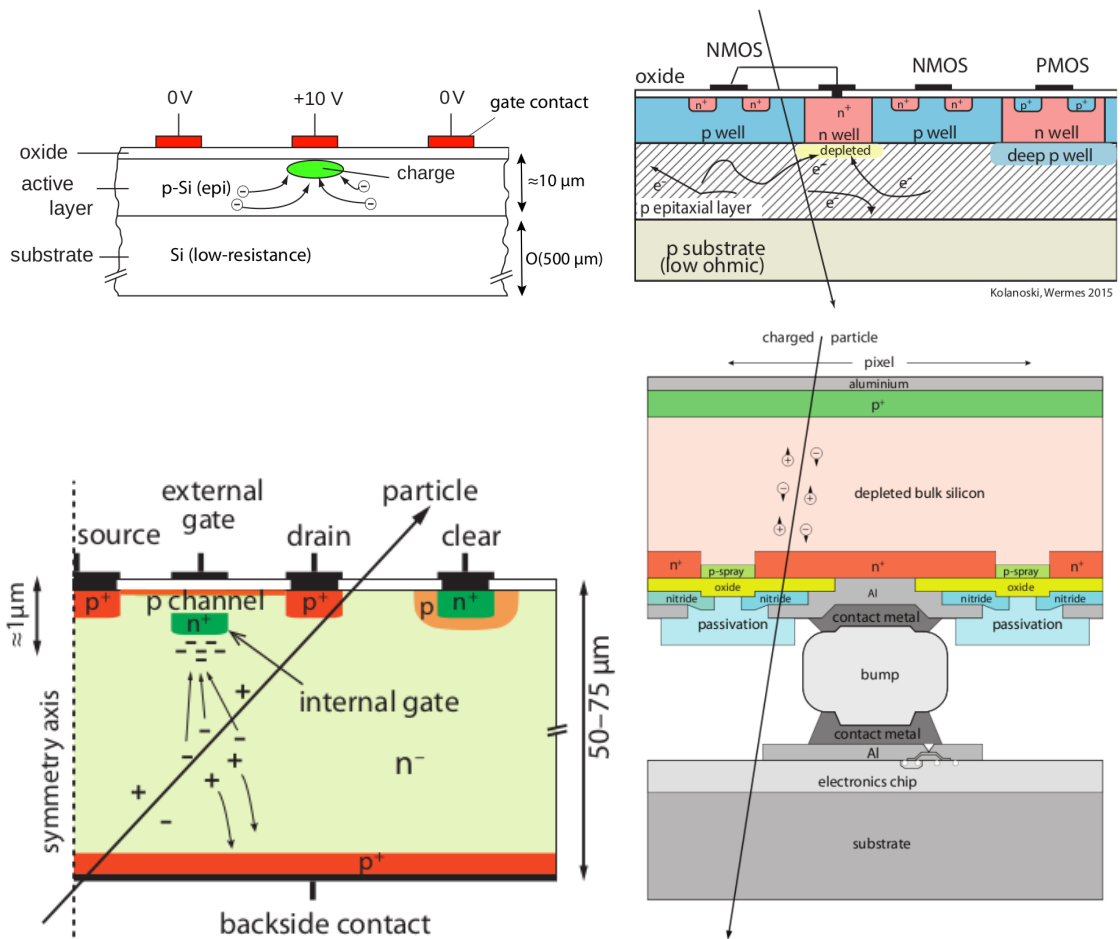


Figure 1.3: Concept cross-section of hybrid pixel (a) and of a DEPFET (b)

190 liming the detector lifetime up to a few years. With the availability of high quality p-
191 substrate material ($\gtrsim 2 \text{ k}\Omega\text{cm}$) the fabrication of n-in-p type sensors, which does not invert
192 anymore, became the preferred choise leading also a huge advance in cost reduction due
193 to no more need of double sided. However, the particular and sophisticated procedure to
194 bond sensor and ASIC makes them difficult to produce, delicate (especially when exposed
195 to high levels of radiation) and also expensive.

196 DEPFET are the first attempt towards the integration of the front end (FE) on the
197 sensor bulk: they are typically mounted on a hybrid structure but the sensor also in-
198 tegrates the first amplification stage. Each pixel implements a MOSFET (metal-oxide-
199 semiconductor field-effect transistor) transistor (a p-channel in fig. 1.3b): a hole current
200 flows from source to drain which is controlled by the external gate and the internal gate
201 together. The internal gate is made by a deep $n+$ implant towards which electrons drift
202 after being created in the depletion region; the accumulation of electrons in the region
203 underneath the n implant changes the gate potential and controls the transistor current;
204 the removal of the signal charge from the internal gate is called "Clear". DEPFET typ-
205 ically have a good S/N ratio: this is principally due to the amplification on-pixel, which
206 guarantees any charge losses, and to the large depletion region. They can be operated in-
207 dividually or integrated in the readout nodes of other detectors, as for example silicon drift
208 chambers, but they always need to be connected to an ASIC with a readout circuit on it.
209 In recent years, the sensor development was driven by an intensive R&D and prototyping
210 for x-ray imagers and the ILC vertex detector.

211 1.4 CMOS MAPS and DMPAS

212 Monolithic active pixels accommodate on the same wafer both the sensor and the FE
213 electronics, with the second one implanted on top within a depth of about $1 \mu\text{m}$ below
214 the surface. MAPS have been first proposed and realized in the 1990s and their practical
215 usage has been enabled by the development of the electronic sector, which guarantees the
216 halving of CMOS transistors dimension at least every two years, as stated by the Moore's
217 law. As a matter of fact the dimension of components, their organization on the pixel
218 area and logic density are important issues for the design and for the layout. Compared
219 to CCDs, the readout time is dramatically reduced by the in-pixel amplification and
220 discrimination, typically followed by a sparsified readout not requiring the signal to be
221 transported anymore over thousands of pixels; as aside effect, the radiation tolerance is
222 also greatly increased by sensing the signal charge directly within its own pixel.

223 A critical parameter for accelerator experiments is the material budget, which repre-
224 sents the main limit factor for momentum measurement resolution in a magnetic field;
225 since hybrid pixels are thicker (\sim hundreds of μm) than monolithic ones (even less than
226 $100 \mu\text{m}$). Using the latter the material budget can be down by a third: typical values for
227 hybrid pixels is $1.5 \% X_0$ per layer, while for monolithic $0.5 \% X_0$. Compared to MAPS,
228 among other disadvantages of hybrid pixels there is the bigger power consumption, that
229 requires also a bigger cooling system, leading to a futher increase of material.

230 Monolithic active pixel can be distinguished between two main categories: MAPS and
231 depleted MAPS (DMAPS). MAPS (figure a ??) have typically an epitaxial layer in a from
232 range $1 \mu\text{m}$ to $20 \mu\text{m}$ and, since they are not depleted, the charge is mainly collected by
233 diffusion rather than by drift. This makes the path of charges created in the bulk longer
234 than usual, making them slow (of order of 100 ns). Moreover, the collection can be partial,

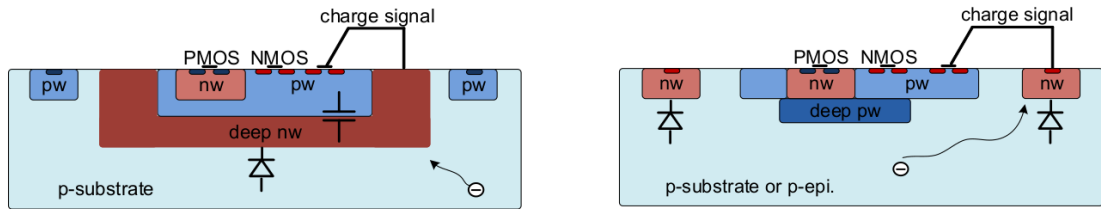


Figure 1.4: Concept cross-section with large and small fill factor

especially after irradiation of the detector (look at ?? for radiation damages), when the trapping probability becomes higher. In figure ?? it is shown as example of CMOS MAPS: the sensor implements an n well as collection diode; to prevent the others n wells (which contain PMOS transistor) of the electronic circuit competing in charge collection and to shield the CMOS circuit from the substrate, additional underlying deep p well are needed. DMAPS are instead MAPS depleted with d typically in $\sim 25 \mu\text{m}$ to $150 \mu\text{m}$ (eq. 1.2) which extends from the diode to the deep p-well, and sometimes also to the backside (in this case if one wants to collect the signal also on this electrode, additional process must be done).

1.4.1 DMAPS: large and small fill factor

There are two different sensor-design approaches (figure 1.4) to DMAPS:

- large fill factor: a large collection electrode that is a large deep n-well and that host the embedded electronics
- small fill factor: a small n-well is used as charge collection node

To implement a uniform and stronger electric field, DMAPS often uses large electrode design that requires multiple wells (typically four including deep n and p wells); with this layout the total capacity of the sensor increases because of the addition of a new term (fig. 1.5), which contributes to the total amplifier input capacity ($\sim 100 \text{ fF}$). In addition to the capacity between pixels (C_{pp}) and between the pixel and the backside (C_b), a non-negligible contribution comes from the capacities between wells (C_{SW} and C_{WW}) needed to shield the embedded electronics. These capacities affect the thermal and $1/f$ noise of the charge amplifier and the τ_{CSA} too:

$$ENC_{thermal}^2 \propto \frac{4}{3} \frac{kT}{g_m} \frac{C_D^2}{\tau_{sh}} \quad \tau_{CSA} \propto \frac{1}{g_m} \frac{C_D}{C_f} \quad (1.5)$$

where g_m is the transconductance, τ_{sh} is the shaping time. Among the disadvantages coming from this large input capacity there is a coupling between the sensor and the electronics resulting in cross talk noise on neighbouring electrodes; indeed, since digital switching in the FE electronics does a lot of oscillations, this problem is especially connected with the intra wells capacities. So, larger charge collection electrode sensors provide a uniform electric field in the bulk that results in short drift path and so in good collection properties, especially after irradiation, when trapping probability can become an issue.

The small fill-factor variant, instead, benefits from a small capacity (5 fF to 20 fF), but suffers from a non uniform electric field and from all the issue related to that (slowness and high trapping probability). As we'll see these two different types of sensor require

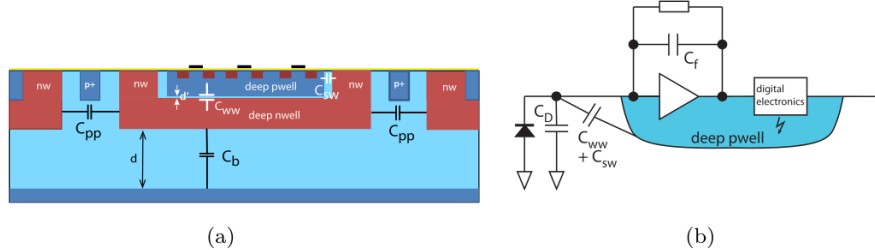


Figure 1.5: C_{pp} , C_b , C_{WW} , C_{SW}

	small fill factor	large fill factor
small sensor C	✓ (< 5 fF)	✗ (~ 100 200 fF)
low noise	✓	✗
low cross talk	✓	✗
velocity performances	✓	✗ (~100 ns)
short drift paths	✗	✓
radiation hard	✗	✓

Table 1.1: Small and large fill factor DMAPS characteristics

267 different amplifier: the large electrode one is coupled with a charge sensitive amplifier,
268 while the small one with a voltage amplifier (sec 1.5.1).

269 1.4.2 A modified sensor

270 A process modification, developed by CERN in collaboration with the foundries, which
271 has become the standard solution to combine the characteristics of a small fill factor
272 sensor (small input amplifier capacity) and of a large fill factor sensor (uniform electric
273 field), is the one carried out for ALICE upgrade about ten years [1]. A compromise
274 between the two sensors could also be making smaller pixels, but this solution requires
275 reducing the electronic circuit area, so a completely new pixel layout should be though.
276 The modification consists in inserting a low dose implant under the electrode and one of
277 its advantage lies in its versatility: in fact, both standard and modified sensor are often
278 produced for testing.

279 Before the process modification, the depletion region extends below the diode towards
280 the substrate, and it does not extend much laterally, even if a high bias is applied to the
281 sensor (fig. 1.6). After the modification, two distinct pn junctions are built: one between
282 the deep p well and the n⁻ layer, and the other between the n⁻ and the p⁻ epitaxial
283 layer, extending to the whole area of the sensor. Since deep p well and the p-substrate are
284 separated by the depletion region, the two p electrodes can be biased separately² and this
285 is beneficial to enhance the vertical electric field component. The doping concentration is
286 a trimmer parameter: it must be high enough to be greater than in the epitaxial layer in
287 order to prevent the punchthrough between p-well and the substrate, but it must also be
288 low enough to allow the depletion for reasonable bias values.

²This is true in general, but it can be denied if other doping characteristics are implemented, and we will see that this is the case of TJ-Monopix1

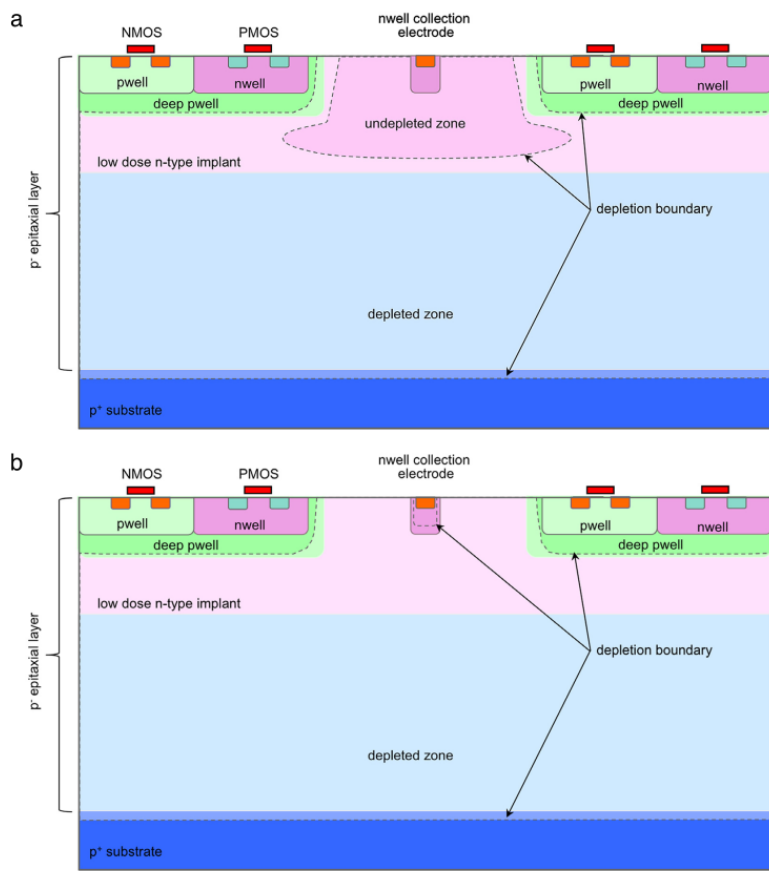


Figure 1.6: A modified process for ALICE tracker detector: a low dose n implant is used to create a planar junction. In (a) the depletion is partial, while in (b) the pixel is fully depleted.

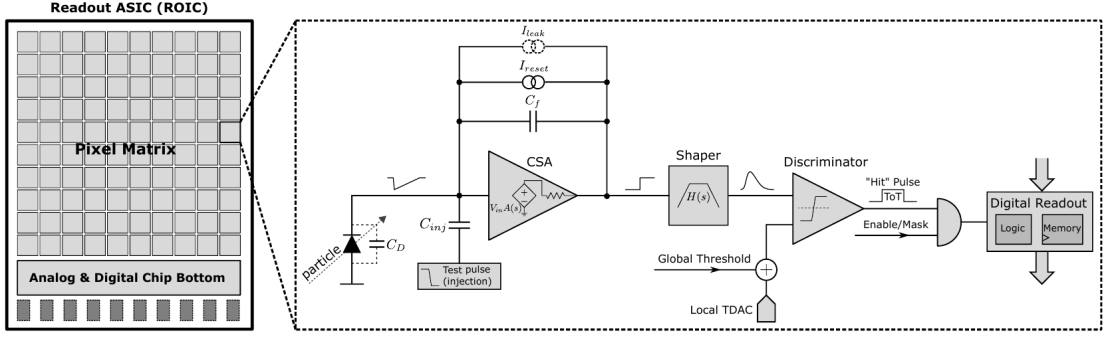


Figure 1.7: Readout FE scheme: in this example the preamplifier is a charge sensitive one (CSA) but changing the capacitive feedback into a resistive one, this can be converted in a voltage or current amplifier.

289 1.5 Analog front end

290 After the creation of a signal on the electrode, the signal enters the front end circuit
 291 (fig.1.7), ready to be molded and transmitted out of chip. Low noise amplification, fast
 292 hit discrimination and an efficient, high-speed readout architecture, consuming as low
 293 power as possible, are the goal of the readout integrated electronics (ROIC). The main
 294 parts of the analog front end chain are a preamplifier (that often is the only amplification
 295 stage) with a reset to the baseline mechanism and a leakage current compensation, a shaper
 296 (a band-pass filter) and finally a discriminator. The whole chain must be optimized and
 297 tuned to improve the S/N ratio. It is very important both not to have a large noise
 298 before the amplification stage in order to not multiply that noise, and chose a reasonable
 299 threshold of the discriminator to cut noise-hits much as possible.

300 1.5.1 Preamplifier

301 Even if circuits on the silicon crystal are only constructed by CMOS, a preamplifier can
 302 be processed as an operational amplifier (OpAmp) where the gain is determined by the
 303 input and feedback impedance (first step in figure 1.7):

$$G = \frac{v_{out}}{v_{in}} = \frac{Z_f}{Z_{in}} \quad (1.6)$$

304 Depending on whether a capacity or a resistance is used as feedback, respectively a
 305 charge or a voltage amplifier is used: if the voltage input signal is large enough and has
 306 a sharp rise time, the voltage sensitive preamplifier is preferred. Consequently, this flavor
 307 doesn't suit to large fill factor MAPS whose signal is already high enough: $v_{in} = Q/C_D \approx$
 308 $3\text{ fC}/100\text{ pF} = 0.03\text{ mV}$, but it's fine for the small fill factor ones: $v_{in} = Q/C_D \approx 3\text{ fC}/3\text{ pF} \approx$
 309 1 mV .

310 In the case of a resistor feedback, if the signal duration is longer than the discharge
 311 time ($\tau = R_S C_D$) of the detector the system works as current amplifier, as the signal
 312 is immediately transmitted to the amplifier; in the complementary case (signal duration
 313 longer than the discharge time) the system integrates the current on the C_D and operates
 314 as a voltage amplifier.

315 1.6 Readout logic

316 The readout logic includes the part of the circuit which takes the FE output signal, pro-
 317 cesses it and then transmit it out of pixel and/or out of chip; depending on the situation
 318 of usage different readout characteristics must be provided. To store the analogical in-
 319 formation (i.e. charge collected, evolution of signal in time, ...) big buffers and a large
 320 bandwidth are needed; the problem that doesn't occur, or better occur only with really
 321 high rate, if one wants record only digital data (if one pixel is hit 1 is recorded, and if not
 322 0 is recorded).

323 A common compromise is to store the time over threshold (ToT) of the pulse in clock
 324 cycle counts; this needs of relatively coarse requirement as the ToT can be trimmed down
 325 to use only a dozen bits but, being correlated (and hopefully linear) with the deposited
 326 charge, it provides a sufficient information. The ToT digitalization usually takes advantage
 327 of the distribution of a clock (namely BCID, bunch crossing identification) on the pixels'
 328 matrix. The required timing precision is better than ~ 25 ns, that corresponds to the period
 329 between bunch collisions at LHC; for such reason a reasonable BCID-clock frequency for
 pixels detector is 40 MHz.

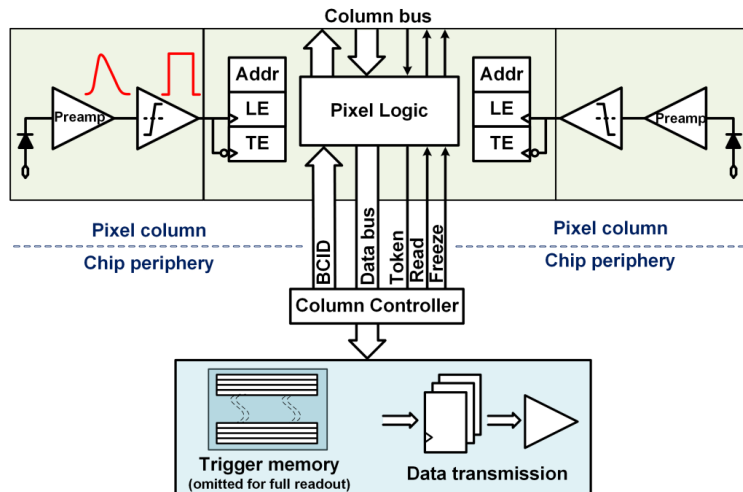


Figure 1.8: Column drain R/O scheme where ToT is saved

330
 331 Moreover, the readout architecture can be full, if every hit is read, or triggered, if a
 332 trigger system decides if the hit must be stored or not. On one hand the triggered-readout
 333 needs buffers and storage memories, on the other the full readout, because there is no
 334 need to store hit data on chip, needs an high enough bandwidth. A triggered readout is
 335 fundamental in accelerator experiments where the quantity of data to store is very large
 336 and some selection has to be applied by the trigger: to give an order of magnitude, at LHC
 337 more than 100 TBit/s of data are produced, but the storage limit is about 100 MBit/s
 338 [2](pag. 797). Typically, the trigger signal is processed in a few μs , so the pixel gets it
 339 only after a hundred clock cycles from the hit arrival time: the buffer depth must be able
 340 to handle such high trigger latency.

341 After having taken out the data from the pixel, it has to be transmitted to the end
 342 of column (EoC) where a serializer delivers it out of chip, typically to an FPGA. There
 343 are several ways of transmitting data from a pixel to the EoC: one of the most famous
 344 is the column-drain read out, developed for CMS and ATLAS experiments [3]. All the

345 pixels in a double-column share a data bus and only one pixel at a time, according to
 346 a priority chain, can be read. The reading order circuit is implemented by shift register
 347 (SR): when a hit arrives, the corresponding data, which can be made of timestamp and
 348 ToT, is temporarily stored on a RAM until the SR allows the access to memory by data
 349 bus. Even if many readout architectures are based on the column-drain one, it doesn't suit
 350 for large size matrices. The problem is the increasing number of pixels on a column would
 351 also raise the number of pixels in the priority chain, which would result in a slowdown of
 352 the readout.

353 If there isn't any storage memory, the double-column behaves as a single server queue
 354 and the probability for a pixel of waiting a time T greater than t , with an input hit rate
 355 on the column μ and an output bandwidth B_W is [4]:

$$P(T > t) = \frac{\mu}{B_W} e^{-(B_W - \mu)t} \quad (1.7)$$

356 To avoid hit loss (let's neglect the contribution to the inefficiency of the dead time τ due
 357 to the AFE), for example imposing $P_T > t \sim 0.001$, one obtains $(B_W - \mu) t_t \sim 6$, where
 358 t_t is the time needed to transfer the hit; since t_t is small, one must have $B_W \gg \mu$, that
 means a high bandwidth [4].

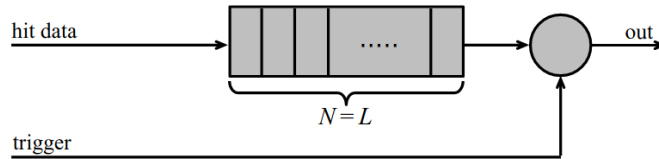


Figure 1.9: Block diagram of a pipeline buffer: N is the dimension of memory buffer and L is the trigger latency expressed in BCID cycles

359 Eq.1.7 is actually an approximation, since each pixel sees a different bandwidth de-
 360 pending on the position on the queue: the first one sees the full bandwidth, while the next
 361 sees a smaller one because it can be occasionally blocked by the previous pixel. Then,
 362 the bandwidth seen by the pixel i is $B_i = B - \sum_j \mu_j$, where μ_j is the hit rate of the j th
 363 pixel. The efficiency requirement on the bandwidth and the hit rate becomes: $B_{W,i} > \mu_i$,
 364 where the index i means that the constraint is for a single pixel; if all the N pixels on a
 365 column have the same rate $\mu = N\mu_i$, the condition reduces to $B_W > \mu$. The bandwidth
 366 must be chosen such that the mean time between hits of the last pixel in the readout chain
 367 is bigger than that. In order to reduce the bandwidth, a readout with zero suppression
 368 on pixel is typically employed; this means that only information from channels where the
 369 signal exceeds the discriminator threshold are stored.

371 If, instead, the signal is locally stored until a trigger signal arrives, the input rate to
 372 column bus μ' is reduced compared to the hit rate μ as: $\mu' = \mu \times r \times t$, where r is the
 373 trigger rate and t is the bunch crossing period. In this situation there is a more relaxed
 374 constraint on the bandwidth, but the limiting factor is the buffer depth: the amount of
 375 memory designed depends both on the expected rate μ and on the trigger latency t as
 376 $\propto \mu \times t$, which means that the higher the trigger latency the lower the hit rate to cope
 377 with.

378 In order to have an efficient usage of memory on pixels' area it's convenient grouping
 379 pixels into regions with shared storage. Let's compare two different situations: in the first
 380 one a buffer is located on each pixel area, while in the second one a core of four pixels

³⁸¹ share a common buffer (this architecture is commonly called FE-I4).

Consider a 50 kHz single pixel hits rate and a trigger latency of 5 μs , the probability of

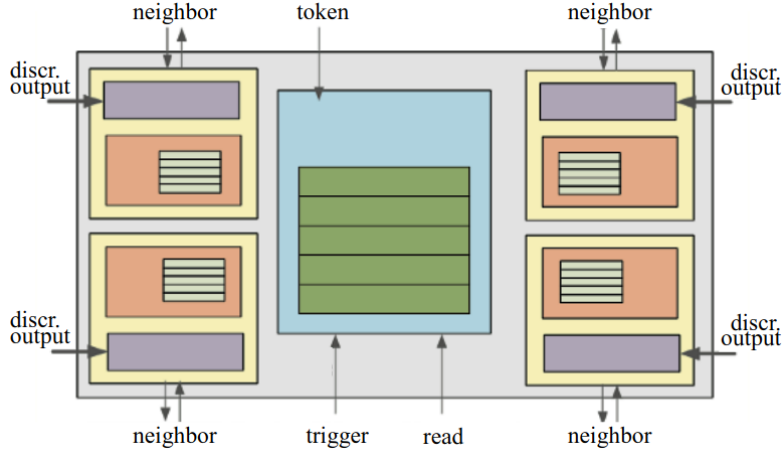


Figure 1.10: Block diagram of the FE-I4 R/O. Read and memory management section is highlighted in light blue; latency counters and trigger management section are highlighted in green; hit processing blocks are highlighted in purple; ToT counters and ToT management units are highlighted in orange

³⁸²

³⁸³ losing hits is:

$$P(N > 1|\nu) = 1 - P(N = 0|\nu) - P(N = 1|\nu) = 1 - e^{-\nu}(1 + \nu) \approx 2.6\% \quad (1.8)$$

³⁸⁴ where I have assumed a Poissonian distribution with mean $\nu = 0.25$ to describe the counts
³⁸⁵ N.

³⁸⁶ To get an efficiency ϵ greater than 99.9 % a 3 hit depth buffer is needed:

$$P(N > 3|\nu) = 1 - \sum_{i=0}^3 P(N = i|\nu) < 0.1\% \quad (1.9)$$

³⁸⁷ Consider the second situation: if the average single pixel rate is still 50 kHz, grouping four
³⁸⁸ pixels the mean number of hits per trigger latency is $\nu = 0.25 \times 4 = 1$. To get an efficiency
³⁸⁹ of 99.9% (eq. 1.9) a buffer depth of 5 hits in the four-pixels region, instead of 3 per pixels,
³⁹⁰ is needed.

391 **Chapter 2**

392 **Use of pixel detectors**

393 The relation between the development of cameras and that of pixel detectors dates back
394 to 1969, when the idea of CCDs, for which Boyle and Smith were awarded the Nobel Prize
395 in Physics in 2009, revolutionized photography allowing light to be captured electronically
396 instead of on film. Even though the CMOS technology already existed at the time the
397 CCDs spread, the costs of productions were too high to allow the diffusion of these sensors
398 for the following 20 years. From that moment on, the fast diffusion of CMOS was mainly
399 due to the less cost than CCD, and the less power supply required. Nowadays CCDs
400 are still preferred over MAPS in astronomy, where the astronomical sources' rate are low
401 enough to cope with slow readout time (tens of ms).

402 The principal use cases of pixel detectors are particle tracking and imaging: in the
403 former case individual charged particles have to be identified, in the latter instead an
404 image is obtained by the usually un-triggered accumulation of the impinging radiation.
405 Also the demands on detectors performance depends on their usage, in particular tracking
406 requires high spatial resolution, fast readout and radiation hardness.

407 **2.1 Tracking in HEP**

408 At first the physics world overlooked the CCDs, and all pixel in general, as against the
409 gaseous detector for tracking: there was no need to replace these ones which had a sufficient
410 good resolution ($100\text{ }\mu\text{m}$). Since 1974, with the measurement of the invariant mass of the
411 J/Psi and the affirmation of the quark model, all experiments start to look for better
412 spatial resolutions in order to achieve the possibility of reconstructing short lived particle.

413 Historically, the first pixel detector employed in particle physics was a CCD: it was
414 installed in the spectrometer at the CERN's Super Proton Synchrotron (SPS) by the
415 ACCMOR Collaboration (Amsterdam, CERN, Cracow, Munich, Oxford, RAL) at mid
416 1980s, with the purpose of studying the (at the time) recently-discovered charm particles.
417 The second famous usage of CCDs took place at SLAC in the Large Detector (SLD) during
418 the two years 1996-98, where the CCD technology was adopted instead of the microstrip
419 detectors for their excellent spatial resolution (cell size $22 \times 22\text{ }\mu\text{m}^2$ giving a resolution of
420 $\sim 5\text{ }\mu\text{m}$) thanks to the sufficient time for readout between two successive collisions (160 ms).

421 From that period on, particle tracking in HEP experiments have been transformed
422 radically. It became mandatory to build an inner vertex detector, with the following tasks:

- 423 • pattern recognition with the identification of particle tracks at large backgrounds and
424 pile-up

- measurement of vertices (primary and secondary)
- multi-track and vertex separation in the core of jets
- measurement of specific ionization
- momentum measurement combining with other detectors informations

In 1991, the more demanding environments led to the development of hybrid pixel detectors: a dedicated collaboration, RD19, was established at CERN with the specific goal of defining a semiconductor micropattern detector with an incorporated signal processing at a microscopic level. In those years a wide set of prototypes of hybrid pixel has been manufactured; among the greatest productions a mention goes to the huge ATLAS and CMS vertex detectors. From the middle of 2013 a second collaboration, RD53, has been established with the new goal of finding a pixel detector suitable for the phase II in future upgrades of those experiments. Even if the collaboration is specifically focused on the design of hybrid pixel readout chips (aiming to 65 nm technique), also other options have been taken in account and many test have been done on MAPS. Requirements imposed by LHC are stringent and they will become even more with the increase of luminosity at HL-LHC: for example, a dose and radiation of 5 Mrad and 10^{16} NIEL are expected after 5 years of operation. Time resolution, material budget and power consumption are also issues for the upgrade: to distinguish different events from different bunches a time resolution better than 25 ns for a bunch crossing frequency of 40 MHz is required, a material budget lower than 2% and a power consumption lower than 500 mW/cm^2 are required.

Amidst the solutions proposed 3D silicon detector, invented by Sherwood Parker in 1995, and MAPS are the most promising. In 3D sensors the electrode is a narrow column of n-type implanted vertically across the bulk instead of being implanted on the wafer's surface. The charge produced by the impinging particle is then drifted transversally within the pixel, and, as the mean path between two electrode can be sufficient low, the trap probability is not an issue. Even if 3D detector are adequately radiation hard and are a strong contender for hybrid pixel modules, especially in the innermost pixel detector layer, their fabrication process is currently low volume, making them unlikely to cover large areas.

2.1.1 Hybrid pixels at LHC and at SuperKEKB

ATLAS

With CMS, ATLAS is one of two general-purpose detectors at the LHC and has the largest volume detector ever constructed for a particle collider (46 m long and 25 m in diameter). The Inner Tracker (ITk) consists of three different systems all immersed in a magnetic field parallel to the beam axis whose main components are: the pixel, the micro-strips and transition radiation trackers. Concerning the pixel detector, they installed a 3-layer hybrid pixel detector in 2007 and an additional one inserted within the original detector envelope and therefore called insertable B-layer (IBL) in 2014. 92 million pixels are divided in 4 barrel layers and 3 disks in each end-cap region, covering a total area of 1.9 m^2 and having a 15 kW of power consumption.

As stated by the ATLAS collaboration the pixel detector is exposed by an extreme particle flux: "By the end of Run 3¹, the number of particles that will have hit the

¹Run 3 start in June 2022

467 innermost pixel layers will be comparable to the number it would receive if it were placed
 468 only a few kilometres from the Sun during a solar flare". Considering that the particle
 469 density will increase even more with HL-LHC, radiation hardness is definitively target to
 470 achieve. The most ambitious goal is employ a MAPS-based detector for the inner-layer
 471 barrels, and for this reason the RD53 collaboration is designing many MAPS prototypes
 472 (as for example TJ-Monopix1, which I will talk about in chapter 3) and performing test.
 473 Up to now this possibility will be eventually implemented during the second phase of the
 474 HL-LHC era, as at the start of high-luminosity operation the selected option is the hybrid
 475 one. The sensor will be bonded with ITkPix, the first full-scale 65 nm hybrid pixel-readout
 476 chip developed by the RD53 collaboration. Regarding the sensor, a valuable option is
 477 using 3D pixels, which have already proved themselves in ATLAS, for the IBL, where they
 478 were introduced in a limited acceptance range and introduced a new readout integrated
 479 circuit called FE-I4. Also the complexity of the readout will be raised, as the number of
 480 pixels will be increased of a factor about 7, passing from 92 millions to 6 billion.

481 CMS

482 The CMS hybrid pixel detector has been upgraded in 2017, when, with the replacement
 483 of a piece of the beam pipe, a layer has been added to the detector at 3 cm from it.
 484 124 million pixels are divided between the barrel pixel detector (BPIX) and the forward
 485 disks (FPIX), with sensors which are different from each other and produced by different
 486 foundries. The sensors have an area equal to 100 μm by 150 μm and have been produced
 487 on 285 μm to 300 μm thick wafers.

488 The time resolution is 25 ns, and the information coming from the detector are stored on
 489 chip for the Level-1 trigger latency ($\sim 4 \mu\text{s}$). The upgrade baseline ROIC was redesigned for
 490 the outer 3 layers, replacing analog signal readout with on-chip ADCs and digital readout
 491 at higher rate. reads out the pulse height information for each pixel.

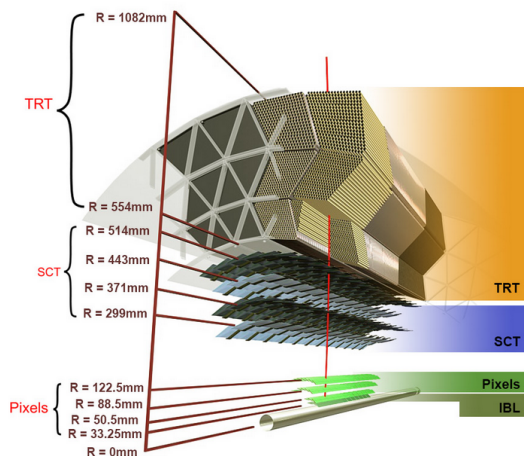


Figure 2.1: ATLAS tracker detector

492 LHCb

493 LHCb is a dedicated heavy-flavour physics experiment that exploits pp interactions at
 494 14 TeV at LHC. It was the last experiment to upgrade the vertex detector, the Vertex

495 Locator (VELO), replacing the silicon-strip with 26 plane pixel detector (because of the
 496 fixed target geometry) in May 2022. As the instantaneous luminosity in Run3 is increased
 497 by a factor $\lesssim 10$, much of the readout electronics and of the trigger system have been
 498 developed in order to cope with the large interaction rate. To place the detector as close as
 499 possible to the beampipe and reach a better track reconstruction efficiency and resolution,
 500 the VELO has a surprising feature: during the injection of LHC protons it is parked at
 501 3 cm from the beams and only when the stability is reached it is moved at ~ 5 mm. Readout
 502 speed is a priority for the detector that uses a triggerless readout at 40 MHz collision rate,
 503 producing 20 Gbps per ROIC. The Velopix, which is the hybrid system designed for LHCb,
 504 is made bonding sensors, each measuring 55×55 micrometers, 200 μm -thick to a 200 μm -
 505 thick ASIC specially developed for LHCb and coming from the Medipix family (sec. ??),
 506 which can handle hit rates up to 900 MHz per chip. Since the detector is operated under
 507 vacuum near the beam pipe, the heat removal is particularly difficult and evaporative CO₂
 508 microchannel cooling are used.

509 **BelleII**

510 Due to the high background level coming from the nanobeam used at SuperKEKB in
 511 order to achieve a such high luminosity ($4.7 \times 10^{34} \text{ cm}^{-2}/\text{s}$), silicon strip cannot be used
 512 in the inner layer of the tracker. The occupancy is too high to allow the usage of strips up
 513 to 40 mm from the beam pipe. Moreover for a precise reconstruction of B-decay vertices,
 514 the usage of thin detector is mandatory at the low energy (4 GeV to 7 GeV) of the beam,
 in order to minimize the multiple scattering of particles. The current vertex detector of

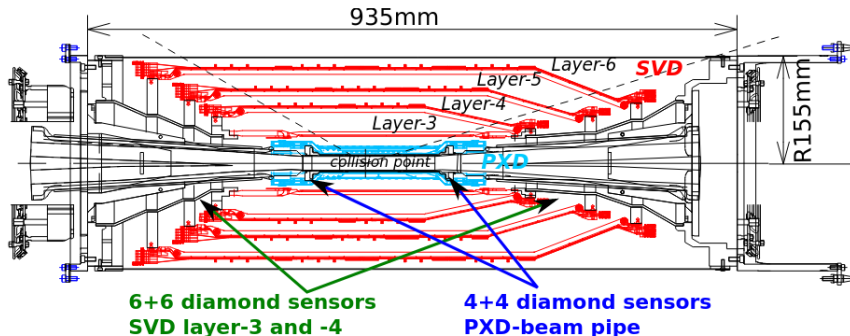


Figure 2.2: Belle2 vertex detector. Since an accidental beam background enhancement can damage the VXD, diamond detectors are installed in order to monitor it.

515
 516 BelleII, VXD, is made of a pixel detector (PXD), fabricated with 2 layers of DEPFET-
 517 based pixels, and 4 layers of a double-sided silicon strip detectors (SVD)[5]. Due to the
 518 small capacitance of the collection node, DEPFET presents a high signal-to-noise ratio
 519 (in 30-50) thanks to the low intrinsic noise and to the large signal achieved with the fully
 520 depleted bulk: pixels are thinned to 75 μm in the active region, then a MIP is supposed
 521 to create a signal of $\sim 6000 \text{ e}^-$, while the typical noise of DEPFET is around 200 e^- . The
 522 ASIC read out is still based on a rolling shutter logic, with an integration time of 20 μs .
 523 In order to reduce the data-storage memory PXD hits are only used to improve spatial
 524 resolution of tracks: the SVD informations are used by the High Level Trigger (HLT) to
 525 look for regions of interest in the pixel ladders just by extrapolating back the tracks found
 526 in the tracker detector, and this method allows to store only data belonging to these areas;



Figure 2.3: (a) Block-diagram of the ULTIMATE-2 sensor. (b) The HFT pixel detector of STAR;

527 the PXD hits are then used in offline track fit to improve the vertex resolution.

528 MAPS have been proposed for the replacement of VXD during the Long Shut Down
 529 2 (LSD2) foreseen around 2026-27; the new vertex detector, VTX, should be made of 5
 530 layers fabricated by the optimized Belle II pixel sensor (OBELIX), a detector based on
 531 TJ-Monopix have been selected (look at chapter ??). The main advantages VTX should
 532 bring are a obvious improving in the track and vertex resolution (14 μm before upgrade,
 533 $\lesssim 10 \mu\text{m}$ expected after upgrade) and a reduction in the X_0 (da.. a..), a higher background
 534 tolerance because of the smaller sensor than strips dimension and a low bandwidth due to
 535 the on-chip sparsification.

536 2.1.2 First attempts to MAPS

537 MIMOSA at EUDET and STAR

538 MIMOSA [6][7] (standing for Minimum Ionizing MOS Active pixel sensor), designed in
 539 2008, prefigured the architecture of MAPS for coming vertex detector being the first large
 540 scale sensor to be employed as detector. MIMOSA-26 equiped the final version of EUDET
 541 high resolution beam telescope both at CERN-SPS and at DESY while the MIMOSA-
 542 28 devices are used for the first MAPS-based vertex detector at the STAR experiment.
 543 MIMOSA-26 is fabricated in a 350 nm, and a module features 1152 columns, split into
 544 18 independent groups, and 576 rows, with square pixels having a side of 18.4 μm lenght;
 545 the epitaxial layer is not fully depleted and the charge collection is mostly by diffusion,
 546 resulting in charge sharing between pixels and collection time bigger than 100 ns.

547 The readout is done in a rolling shutter mode and it is the first MAPS integrating on
 548 chip the zero suppression: the chip is an Active Pixels (APS) and therefore it incorporates
 549 the amplification on pixel, while the signal discrimination and zero-suppression logic are
 550 placed at the EoC, where is also placed a memory. The chip is an Active Pixels (APS)
 551 and therefore it incorporates the amplification on pixel, while the signal discrimination
 552 and zero-suppression logic are placed at the EoC: the readout is done in a rolling shutter

553 mode with a frame integration time that can be lowered down to 85 ms, and a memory
554 allowing to store up to six hits is.

555 The EUDET telescope, equipped with six sensor planes, requires highly granular and
556 thin pixel detectors in order to achieve an excellent track resolution (around 2 μm) even at
557 the rather low particle energies of up to 6 GeV. The STAR experiment at the Relativistic
558 Heavy Ion Collide (RHIC) accelerator at the Brookhaven National Laboratory (BNL) is
559 the first to include MAPS in the vertex detector[8]. The main tracking detector in STAR is
560 a TPC with radii 60-190 cm embedded in a 0.5 T solenoidal magnetic field, that provides
561 a pointing resolution of approximately 1 mm. The pixel detector, PXL, is a part of a
562 3-detector system, Heavy Flavor Tracker (HFT), that has been added to the pre-existing
563 STAR apparatus just before the 2014 Run in order to improve the impact parameter
564 resolution and to enable the direct reconstruction of hadronic decays of heavy flavor mesons
565 and baryons. The Heavy Flavor Tracker (HFT) is composed by the Silicon Strip Detector
566 (SSD), the Intermediate Silicon Tracker (IST) and the Pixel Detector (PXL); the first
567 one is placed at 22 cm from the beam pipe and consists of double sided strips with 95 μm
568 inter-strip pitch, the second one, placed at 14 cm, is made of single sided silicon pads
569 with $600 \mu\text{m} \times 6 \text{ mm}$ pitch and the last one made by two layers is placed at 2.8 cm and 8 cm
570 fabricated with ULTIMATE2 (also known as MIMOSA-28), a successor of MIMOSA-26
571 sensor, with pitch 20.7 μm and thinned down to 50 μm . An area of 0.16 m^2 are covered
572 by 400 MAPS sensor, corresponding to 356 millions of pixels divided into array size of 928×960 .
573 Each pixel includes circuitry for readout, amplification, and Correlated Double
574 Sampling (CDS) for signal extraction and noise subtraction and the frame integration time
575 is 185.6 μs ; after the subtraction the signal to noise ratio is ~ 30 , with a noise between
576 10-12 electrons and a signal of 1000 e^- . Thanks to the HFT system and the PXL, STAR
577 achieved a track pointing resolution 46 μm for 750 MeV/c kaons, and better than 30 μm for
578 particle momenta bigger than 1 GeV/c: this performance enabled the study of D-meson
579 production with a high significance signal.

580 **ALPIDE at ALICE**

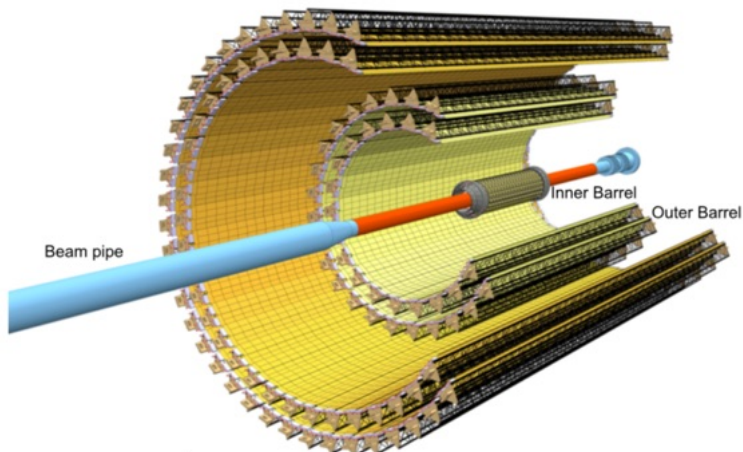


Figure 2.4

581 The ALICE (A Large Ion Collider Experiment) tracking detector consists of the Inner
582 Tracking System (ITS), the gaseous Time Projection Chamber (TPC) and the Transition

583 Radiation Detector (TRD), all embedded in a magnetic field of 0.5 T. The ITS is made
584 by six layers of detectors, two for each type, from the interaction point outwards: Silicon
585 Pixel Detector (SPD), Silicon Drift Detector (SDD) and Silicon Strip Detector (SSD).
586 Contrary to the others LHC experiments, ALICE tracker is placed in a quite different
587 environments, which enables the usage of a MAPS-based detector: the expected dose
588 assorbed by the tracker is expected to be smaller by two order of magnitude and the rate
589 of interactions is few MHz instead of 40 MHz, even though the number of particles coming
590 out from each interaction is very high (the SPS is invested by a density of particles of
591 $\sim 100 \text{ cm}^{-2}$). The reconstruction of very complicated events with a large number of particle
592 is then a challenge, hence to segment and to minimize the amount of material, which may
593 cause secondary interaction futher complicating the event topology, is considered a viable
594 strategy.

595 ITS2, upgraded during the LHC long shut down in 2019-20, was the first large-area
596 ($\sim 10 \text{ m}^2$ covered by 2.5 Gpixels) silicon vertex detector based on CMOS MAPS. The
597 detector employes the ALPIDE chip, developed by ALICE collaboration, fabricated in the
598 180 nm CMOS Imaging Sensor process of TowerJazz, whose design takes full advantage
599 of process feature which allows full circuitry within the pixel matrix. Thanks to the
600 reduction in the material budget, ITS2 obtained an amazing improvement both in the
601 position measurement and in the momentum resolution, especially improving the efficiency
602 of track reconstruction for particle with very low transverse momentum (by a factor 6 at pT
603 $\sim 0.1 \text{ GeV}/c$). Further advancements in CMOS MAPS technology are being aggressively
604 pursued for the ALICE ITS3 vertex detector upgrades (foreseen around 2026-27), with
605 the goals of reducing the sensor thickness and improving the readout speed (which now is
606 completely asynchronous) of the devices, while keeping power consumption at a minimum.

607 Beside tracking, ALICE has been studing the possibility of exploiting the extreme
608 granularities of MAPS for calorimeter application. In a detector of this type, the energy
609 measurement would come out from the counts of particles traversing the active layers,
610 resulting then in a digital calorimeter. A prototype of such a calorimeter fabricated with
611 the MIMOSA23 chips and containing 39 million pixels devided in 24 layers, alternated
612 with 24 layers of tungsten, have been tested with electron beams and exhibited an en-
613 ergy resolution better than standard hadronic calorimeters, with a stochastic terms of
614 $30\%/\sqrt{E(\text{GeV})}$, a constant term of 2.8% and noise term of 0.063 GeV. Moreover, the
615 passive cooling via the tungsten structure has proven to be sufficient for the higher level of
616 heat produced by the chip with respect the conventional sensor while keeping the structure
617 compact.

618 2.2 Other applications

619 Historically for imaging pourpose the CCDs were the favoured device: they can be used as
620 single photon counter or integrating and collecting the charge released by more impinging
621 particles. The utilisation in the first case is similar to the tracking one, except that the
622 requirements are less tight, so much that two noteworthy of microchips originally meant
623 for detectors in particle physics at the LHC, and later employed in other fields are Medipix
624 and Timepix. They are read-out chips developed by the Medipix Collaborations since early
625 1990s. For two decades, different Medipix generations have been produced, having a rough
626 correlation with the feature size used: Medipix2 (1999) used 250 nm feature size CMOS
627 while Medipix3 (2005) 130 nm. For photons imaging other materials with higher atomic

628 charge than silicon could be prefered, as a high photon absorption efficiency is needed: it
629 was for this reason that Medipix2 was bump bonded to identically segmented sensors of
630 both silicon and GaAs.

631 The applications in scientific imaging vary from astrophysics and medical imaging and
632 dosimetry to more exotic domains as studies of protein dynamics, material science, art
633 authentication and archaeology. One of the most important employment of Medipix is as
634 X-ray single photon counting in industrial and medical radiography and in 3D computed
635 tomography². Thanks to a New-Zealand company, the MARS Bioimaging detector has
636 been fabricated, which is capable of resolving the photons energy and produce 3D coloured
637 images. Besides tracking in HEP (I have already cited the use of Timepix3 is in the beam
638 telescope of the LHCb VELO), an important use of Timepix is in dosimetry. [Timepix](#)
639 [Detector for Imaging in Ion Beam Radiotherapy- articolo e qualche info.](#) A small-Timepix
640 detector with the dimension of a USB can also be found at the International Space Station,
641 where it is exploited for radiation, principally made of heavy-ion, monitoring.

642 2.2.1 Applicability to FLASH radiotherapy

643 A possible new application of pixels detector is dosimetry or beam monitoring of charge
644 particles in high intensity radiography. Recently³ a promising method for RT at ultra high
645 dose rate (at least 40 Gy/s) and for this reason called FLASH-RT[9], instead of CONV-RT
646 (0.03 Gy/s), came out. However, finding dosimeters suitable at ultra high dose rate is still
647 an open issue since almost all standard online dosimeters have shown saturation problems.

648 Radiotherapy

649 The radiological treatment is a common method used in 60% of tumors both as palliative
650 care and as treatment. It can be given before, after or during a surgery, (Intra operative
651 radiation therapy-IORT) and many different types of radiations (photons, electrons,
652 protons and ions, which mainly are hydrogen and carbon) can be used to irradiate the
653 affected tissues. Exploiting the ionizing energy loss, that can be parametrized by the
654 Linear Energy Transfer (LET), a biological damage can be delivered to the tissue: while α
655 and β particles are high LET radiations with values in $100 \text{ keV}/\mu\text{m}$ to $200 \text{ keV}/\mu\text{m}$, x-rays
656 and gamma-rays are low LET radiations with values in range $0.2 \text{ keV}/\mu\text{m}$ to $2 \text{ keV}/\mu\text{m}$. If
657 x-ray photons, with energy in 4 MeV to 25 MeV are used, the ionization is caused by the
658 Compton electrons and is more in the superficial layers of the tissue due to the exponential
659 attenuation of the beam. The hadrons energy loss, instead, is strongly localized in
660 the last region of the track, that is the Bragg peak, such as the the treatment typically
661 requires the scanning of the target. The Relative Biological Effectiveness (RBE) of ions
662 near the Bragg peak depends on their mass, and in particular it increases with the ion's
663 mass; even though, too heavy ions generally increases the damage produced also in the
664 entrance region. Carbon is considered the optimum between the two trends.

665 Electrons, instead, of energy in range of a dozen of MeV tend to spread out on a
666 bigger region of a few centimeters in both the diameter and thickness. Using Very High

²The analysis of the direction dependence of X-ray absorption is performed, for example, in order to obtain an image in Computed Tomography (CT)

³The first evidences has been observed on mice experiments in 1966 and in 2014 by the group of Favaudon and Vozenin. After this, many tests on cats and pigs have been performed, and also there has been a clinical trial on a cutaneous tumor-patient

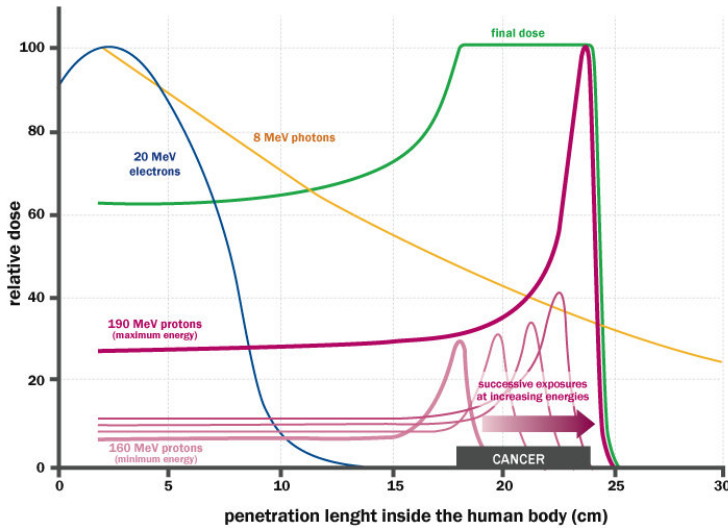


Figure 2.5: The Spread Out Bragg Peak (SOBP) curve (green), which is a constant dose distribution, is obtained from the superposition of many Bragg peak of hadrons with different energy.

	CONV-RT	FLASH-RT
Dose rate	0.03 Gy/s	40 Gy/s
Intra pulse dose rate	100 Gy/s	106 Gy/s
Treatment duration	~minutes	\lesssim 500 ms
Dose Per Pulse	0.3 mGy	1 Gy to 10 Gy
Pulse width	3 μ s	\sim 2 μ s

Table 2.1: Typical value of treatment parameters

667 Energy Electrons (VHEE) has been taken into account for irradiation of deeper tissues,
 668 however, to date, the FLASH effect has been tested and demonstrated only using low-energy
 669 electrons.

670 **FLASH effect**

671 This treatment takes advantages of biological differences between tumors and healthy
 672 tissues: it is characterized by reducing normal tissue toxicity and maintaining equivalent
 673 tumor damage. The response to dose can be described by the survival fraction probability,
 674 describing the fraction of surviving cell as a function of the dose:

$$S(D) = S(0) e^{-(\alpha D + \beta D^2)} \quad (2.1)$$

675 where α and β respectively represents the rate of cell killing by single ionizing events and
 676 by double hits. Hence, at high doses the density of damages increases and the cells repair
 677 becomes more difficult. Even if the FLASH effect is not yet completely understood and
 678 the underlying mechanisms are not clear, it looks like there are two different recipes which
 679 are involved:

- 680 • **The dose rate:** higher dose rate produce bigger damages (fig. 2.6(a)) since this
 681 prevent cells from sparing.
- 682 • **The presence or absence of oxygen:** while hypoxic cells are very resistant to radi-
 683 ation, normal oxygenated cells are highly radiosensitive. This is because if molecules
 684 containing O_2 break due to the impinging radiation, then the oxygen can build Re-
 685 active Oxygen Species (ROS) (fig.2.6(b))

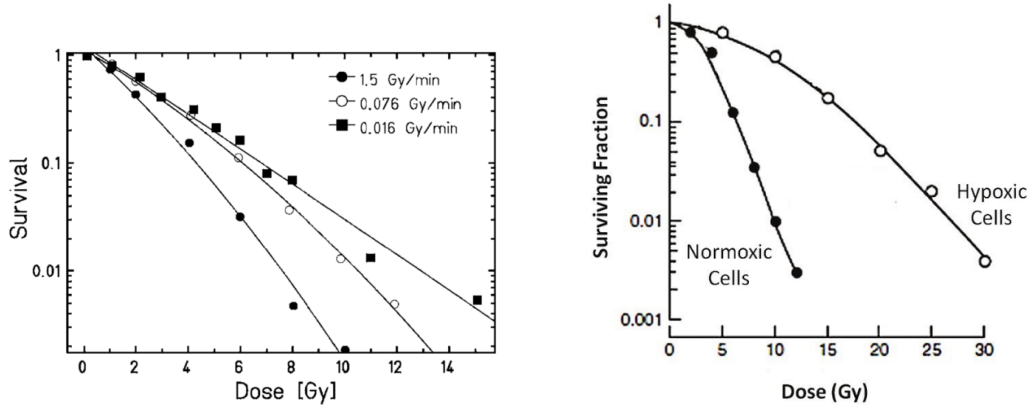


Figure 2.6: (a) Survival curve for different dose rate and (b) for different oxygen cell content

686 The Tumor Control Probability (TCP) and the Normal Tissue Complication (NTC) func-
 687 tions parametrize respectively the efficiency of damaging on the tumor after having released
 688 a certain dose and the probability of not affecting the healthy tissues. The intermediate
 689 zone between the increase of the TC and of the NTC is called therapeutic window, and
 690 the wider it is and the more effective the treatment is.

691 Dosimetric problems

692 Up to now, all online dosimeters have shown saturation problems at high DDP, differently
 693 from radiochromic films, which are the standard passive dosimeters and have shown a
 694 dose-rate independence up to 100 Gy/s. Even though the linear response in wide dynamic
 695 range, they do not provide any online dosimetric informations, since the time required to
 696 extract the physical value from the reading is not instantaneous⁴.

697 Ionization Chambers (ICs), which are the online reference dosimeter also according
 698 to law protocols, at high level of radiation (already at dose per pulse two orders of mag-
 699 nitude lower than the ones used for FLASH-RT) show both problems of saturation and
 700 recombination. When a high density of ions and electrons is produced in the gas, a high
 701 counter electric field opposed to the drift one might be generated; if a neutral region build
 702 up, both the recombination of i/e pairs, with a subsequent photoemission and abrupt dis-
 703 charge can happen. A correction factors, k_{sat} , can be introduced for sufficient low level of
 704 radiation and in this case a precise dose measurement can still be done: under conventional
 705 operation, with Dose Per Pulse (DDP) lower than 1 mGy the correction factor is <5%.

706 Concerning the conventional semiconductor, if exposed to high dose rate, they suffer
 707 of saturation problems just as the ICs, but thin sensors as silicon MAPS are expected

⁴The radiation produces a polymerization of an active layer, resulting in a different density of coloration.

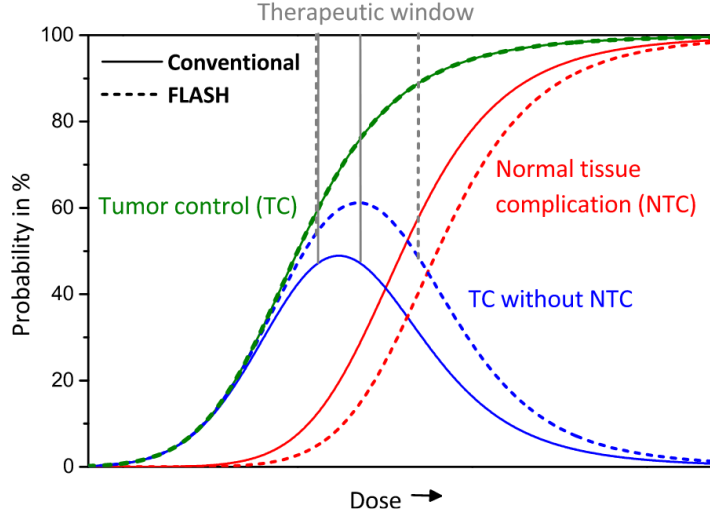


Figure 2.7: Illustration of dependence of TCP, NTCP and therapeutic window on dose, for CONV-RT ad FLASH-RT.

708 to reduce the saturation problem. Indeed a thin planar sensor could allow for a constant
 709 electric field even at high dose rate which, together with the short mean path the e/h must
 710 cover to get the electrode (the epitaxial layer typically is $\sim 30 \mu\text{m}$), could result in a non-
 711 saturated response of the signal. Besides the thinness, also the small capacity typical of
 712 MAPS is beneficial for reducing the readout time: a reduced C_d enables for a fast discharge
 713 and then for a fast readout. Finally, the high spatial resolution requirement obviously
 714 imposed by beam monitor is one of the main reasons which makes MAPS attractive.
 715 Among the semiconductors, also diamond detectors present a high promising alternative
 716 thanks to their high radiation hardness, response stability and linearity in a wide range.
 717 Also other detector types, such as plastic scintillators, optical fiber and alanine dosimeters
 718 have been proposed for high dose environments and many groups are going on studies on
 719 their applicability on FLASH-RT.

720 In reference [10] are presented some results related with saturation problems at high
 721 DDP of different types of detectors. The dosimeters tested and their value at which satura-
 722 tion becomes are reported in table 2.2, while in figure 2.8 are reported the measurements.
 723 The DrR is then defined as the ratio between the signal response of each dosimeters at a
 724 fixed DDP of 1 cGy/p and is called dosimeter reading ratio (DrR):

$$DrR = \frac{R}{R|_{Dp=1cGy/p}} = \frac{R}{R_{ref}} \quad (2.2)$$

725 Then, for a saturation not affected by saturation problems DrR should be a straight line
 726 with a slope equal to 1; since the reference measurements of dose has been performed with
 727 radiochromic films (GAFCHROMIC EBT-XD), whose dose indipendence has been tested⁵
 728 in range from 0 Gy to 15 Gy, the dotted black line in figure 2.8 represents the reference
 729 measurment done with it.

⁵The radiochromic films calibration has been obtained by irradiating the films with dose values in range from 0 Gy to 15 Gy, by positioning the films in a polymethylmethacrylate (PMMA) phantom at R_{100} depth, corresponding to 10 cm

Commercial detector	Detector type	saturation [Gy/p]
PTW TW34045 Advanced Markus EC	ionization chamber	0.3
PTW TM60017 Dosimetry Diode E	silicon diode	0.15
PTW TW60019 microDiamond	diamond	0.15
DoseVue DoseWireTM Series 100	scintillator fiber	11-26

Table 2.2: Results obtain in [10]

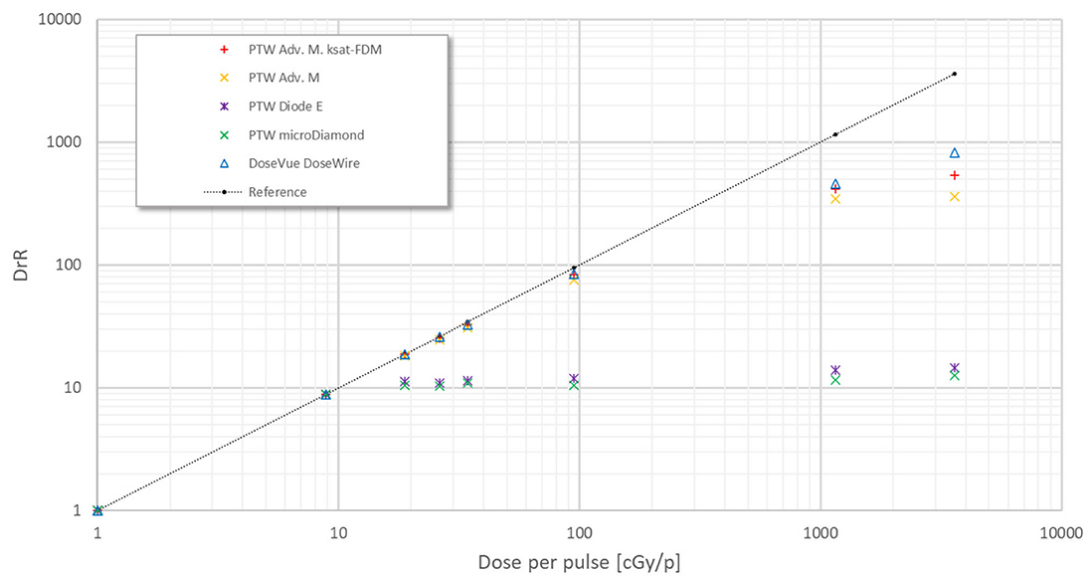


Figure 2.8: Saturation problems underlyed in [10].

730 **Chapter 3**

731 **TJ-Monopix1**

732 TJ-Monopix1 is a small electrode DMAPS with fast R/O capability, fabricated by Tow-
 733 erJazz foundry in 180 nm CMOS imaging process. It is part, together with prototypes
 734 from other series such as TJ-MALTA, of the ongoing R&D efforts aimed at developing
 735 DMAPS in commercial CMOS processes, that could cope with the requirements at ac-
 736 celerator experiments. Both TJ-Monopix and TJ-MALTA series [11], produced with the
 737 same technology by TowerJazz (the timeline of the foundry products is shown in figure
 738 3.1), are small electrode demonstrators and principally differ in the readout design: while
 739 Monopix implements a column-drain R/O, an asynchronous R/O without any distribution
 740 of BCID has been used by TJ-Malta in order to reduce power consumption.



Figure 3.1: Timeline in TowerJazz productions in 180 nm CMOS imaging process

741 Another Monopix series, but in 150 nm CMOS technology, has been produced by
 742 LFoundry [12]. The main differences between the LF-Monopix1 and the TJ-Monopix1
 743 (summarized in table 3.2), lay in the sensor rather than in the readout architecture, as
 744 both chips implements a fast column drain R/O with ToT capability [13][14]. Concerning
 745 the sensors, either are based on a p-type substrate, but with slightly different resistivities;
 746 in addition LFoundry pixels are larger, thicker and have a large fill factor (the very deep n-
 747 well covers ~55% of the pixel area). The primary consequence is that LF-Monopix1 pixels
 748 have a higher capacity resulting in higher consumption and noise. As I discussed in section
 749 1.4.1, the fact that LF-Monopix has a large fill factor electrode is expected to improve its
 750 radiation hardness. Indeed, a comparison of the performance of the two chips showed that
 751 TJ-Monopix suffers a comparatively larger degradation of efficiency after irradiation, due
 752 to the low electric field in the pixel corner; on the other hand, a drawback of the large fill
 753 factor in LF-Monopix is a significant cross-talk.

	LF-Monopix1	TJ-Monopix1
Resistivity	$>2 \text{ k}\Omega\text{cm}$	$>1 \text{ k}\Omega\text{cm}$
Pixel size	$50 \times 250 \mu\text{m}^2$	$36 \times 40 \mu\text{m}^2$
Depth	$100\text{-}750 \mu\text{m}$	$25 \mu\text{m}$
Capacity	$\sim 400 \text{ fF}$	$\sim 3 \text{ fF}$
Preamplifier	charge	voltage
Threshold trimming	on pixel (4-bit DAC)	global threshold
ToT	8 bits	6 bits
Consumption	$\sim 300 \text{ mW/cm}^2$	$\sim 120 \text{ mW/cm}^2$
Threshold	$1500 e^-$	$\sim 270 e^-$
ENC	$100 e^-$	$\sim 30 e^-$

Table 3.1: Main characteristics of Monopix1 produced by TowerJazz and LFoundry [13][14]

754 The TJ-Monopix1 chip contains, apart from the pixels matrix, all the required support
 755 blocks used for configuration and testing:

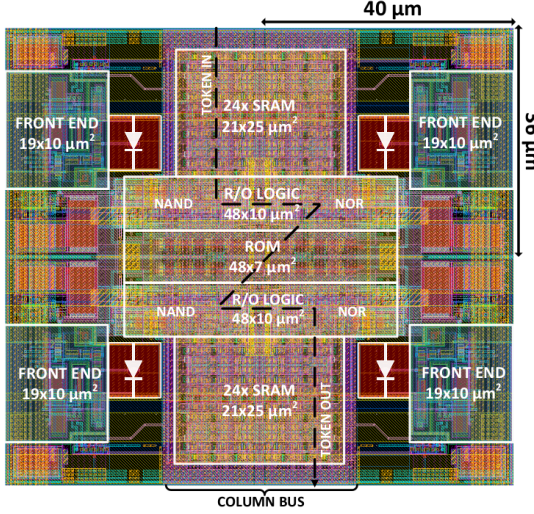
- 756 • the whole matrix contains 224×448 pixels, yielding a total active area approximately
 757 equal to 145 mm^2 over a total area of $1 \times 2 \text{ cm}^2$;
- 758 • at the chip periphery are placed some 7-bit Digital to Analog Converter (DAC), used
 759 to generate the analog bias voltage and current levels and to configuire the FE;
- 760 • at the EoC is placed a serializer to transferred datas immediately, indeed no trigger
 761 memory is implemented in this prototypes;
- 762 • the matrix power pads are distributed at the sides
- 763 • four pixels which have analog output and which can be monitored with an oscillo-
 764 scope, and therefore used for testing

765 Pixels are grouped in 2×2 cores (fig. 3.2a): this layout allows to separate the analog
 766 and the digital electronics area in order to reduce the possible interference between the
 767 two parts. In addition it semplifies the routing of data as pixels on double column share
 768 the same column-bus to EoC. Therefore pixels can be addressed through the physical
 769 column/row or through the logical column/row, as shown in fig. 3.2b: in figure is also
 770 highlighted the token propagaion path, whose I will discuss later.

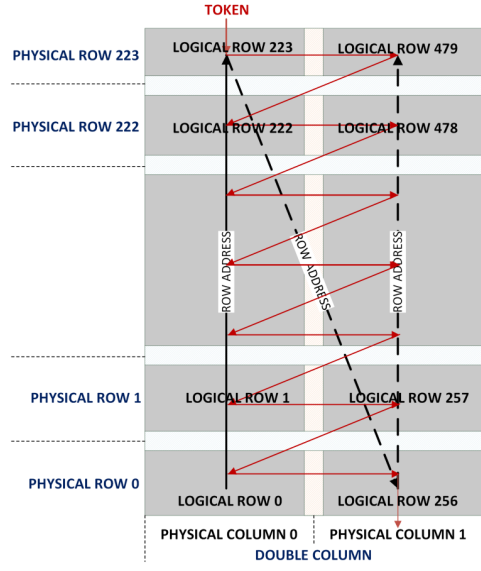
771 Concerning the integration6.5 of the chip in a readout path, TJ-Monopix1 chips have
 772 been wire-bonded on a dedicated carrier board , the Printed Circuit Board (PCB). Two
 773 other board between the DAQ and the chip: the General Purpose Analog Card (GPAC),
 774 which provides power supply channels, current/voltage bias sources and I/O buffer, and
 775 the MIO3 FPGA, which strictly interacts with the DAQ.

776 3.1 The sensor

777 As already anticipated, TJ-Monopix1 has a p-type epitaxial layer and a n doped small
 778 collection electrode ($2 \mu\text{m}$ in diameter); to avoid the n-wells housing the PMOS transistors
 779 competing for the charge collection, a deep p-well substrate, common to all the pixel FE



(a) Layout of a core containing 4 pixels. The analog FE and the digital part are separated in order to reduce cross-talk be



(b)

Parameter	Value
Matrix size	$1 \times 2 \text{ cm}^2$
Pixel size	$36 \times 40 \mu\text{m}^2$
Depth	$25 \mu\text{m}$
Electrode size	$2 \mu\text{m}$
BCID	40 MHz
ToT-bit	6
Power consumption	$\sim 120 \text{ mW/cm}^2$

Table 3.2

area, is used. TJ-Monopix1 adopts the modification described in section 1.4.2 that allows to achieve a planar depletion region near the electrode applying a relatively small reverse bias voltage. This modification improves the efficiency of the detector, especially after irradiation, however a simulation of the electric field in the sensor, made with the software TCAD (Technology Computer Aided Design), shows that a nonuniform field is still produced in the lateral regions of the pixel compromising the efficiency at the corner. Two variations to the process have been proposed in order to further enhance the transversal component of electric field at the pixel borders: on a sample of chip, which includes the one in Pisa, a portion of low dose implant has been removed, creating a step discontinuity in the deep p-well corner (fig. 3.3); the second solution proposed[MOUSTAKAS THESY, PAG 58] consists in adding an extra deep p-well near the pixel edge. A side effect of the alteration in the low dose implant is that the separation between the deep p-well and the p-substrate becomes weak to the point that they cannot be biased separately to prevent the punchthrough.

Moreover, to investigate the charge collection properties, pixels within the matrix are split between bottom top half and bottom half and feature a variation in the coverage of the deep p-well: the electronics area can be fully covered or not. In particular the pixels

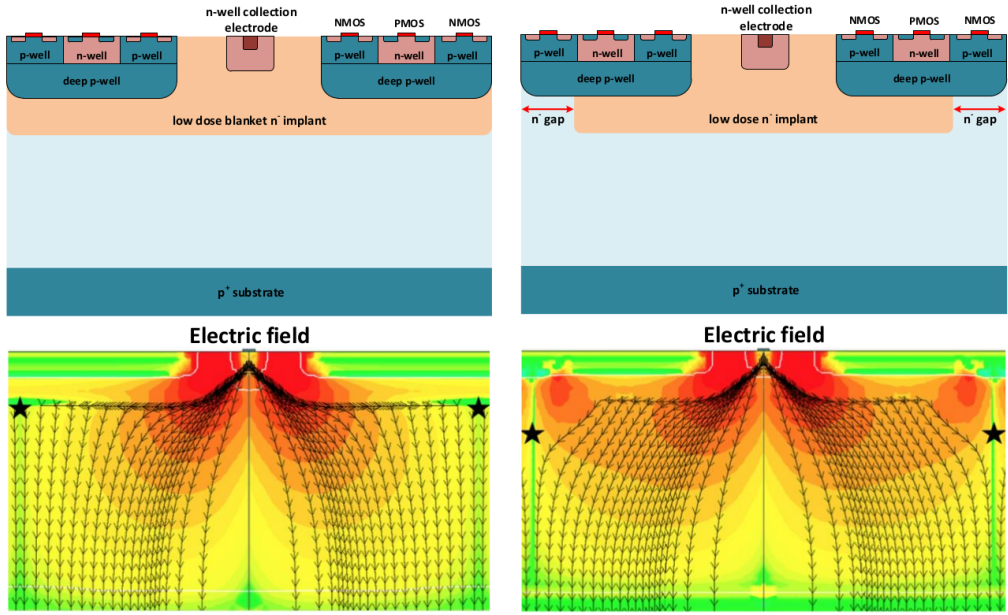


Figure 3.3: (a) The cross-section of a monolithic pixel in the TJ-Monopix with modified process; additionally in (b) a gap in the low dose implant is created to improve the collection of charge due to a bigger lateral component of the electric field. this point in figure is indicated by a star . transversal component of the electric field drops at the pixel corner

797 belonging to rows from 0 to 111 are fully covered (FDPW) and pixels belonging to rows
 798 from 112 to 223 have a reduced p-well (RDPW), resulting in a enhancement of the lateral
 799 component of the electric field.

800 3.2 Front end

801 One of the main advantage of this chip is the small collection electrode, which results in a
 802 small capacitance ($C_{in}=3\text{ fF}$) allowing for high input signal amplitude and single stage of
 803 amplification, which obviously improves the signal to noise ratio performance of the FE.
 804 Assuming a fully depleted epitaxial layer of $25\text{ }\mu\text{m}$, which corresponds approximately to
 805 a $20\text{ }\mu\text{m}$ of deep sensing volume, a MIP should produce $\sim 1600\text{ e}^-$, then:

$$V_{in} = \frac{1600\text{ e}^- \times 1.6 \cdot 10^{-19}\text{ C}}{3\text{ fF}} = 85\text{ mV} \quad (3.1)$$

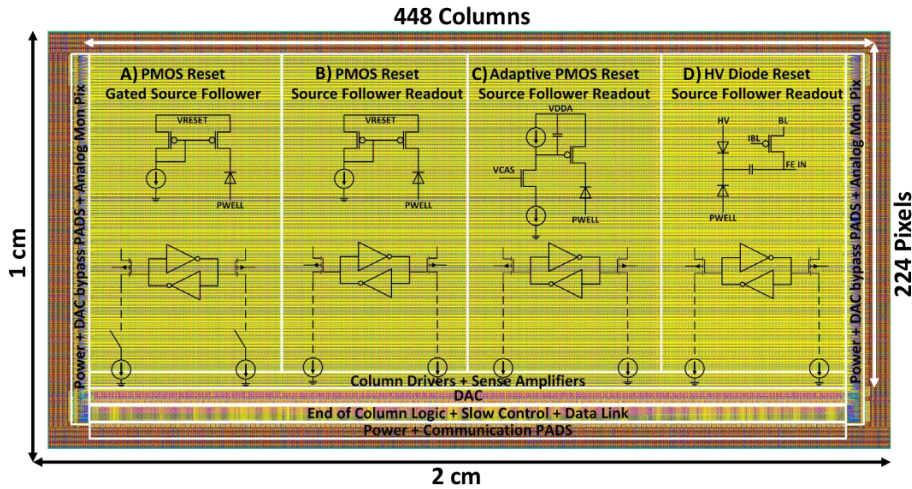
806 Secondly, a reset mechanism which slowly discharges the detector capacitance must be
 807 included in the circuit:

$$V_{in} = \frac{Q_s}{C_{in}} e^{-t/R_b C_{in}} \quad (3.2)$$

808 where R_b is the equivalent reset element. The general constraint which must be satisfied
 809 is that the discharge time $\tau = R_b C_{in}$ must be slower than the characteristic time of
 810 the amplifier, otherwise a signal loss could occurs. Traditionally the reset can be
 811 implemented in two different way: with a forward biased diode, that might be implemented
 812 by a simple p+ diffusion inside the well of the collection electrode n, or with a PMOS
 813 transistor. Despite of the semplicity of the diode reset, since it is a non-linear element,
 814 the discharge would depend on the quantity of charge Q generated on the n electrode,

815 prejudicing the linearity of the analog output (Q-ToT). To solve the issue, a PMOS reset
 816 is the method preferred in design such TJ-Monopix1 with analog output; the PMOS
 817 transistor, indeed, can acts as a constant current source and then used to discharge the
 818 sensor. Although the PMOS reset is capable of providing a constant current, it has to be
 819 manually re-tuned every time in order to restore the input DC baseline voltage; to do that
 820 a low-frequency feedback is used.

821 The matrix is split in four sections, each one corresponding to a different flavor of the
 822 FE, implemented in order to test more options.



823 Figure 3.4: TJ-Monopix1 has been developed in four different flavor. The flavor PMOS
 824 reset (B) is considered as the reference one.

825 All the flavors implement a source-follower double-column bus readout: the standard
 826 variation is the flavor B, that features a PMOS input reset (refered as "PMOS reset").
 827 Flavor A is identical to flavor B except for the realization of the source follower (it is a
 828 gated one): in the circuit of the gated versione there is a transistor more that operates on
 829 the baseline and on the feedback mechanism; this aim to reduce the power consumption
 830 and results in a higher signal baseline, and then in a lower effective threshold. C instead
 831 implements a novel leakage compensation circuit, with a PMOS reset configuration. More-
 832 over the collection electrode can be either DC-coupled to the readout electronics, as in
 833 flavors A, B, C, or AC-coupled through a metal-oxide-metal (MOM) capacitor, as in D
 834 is AC-coupled. The latter one allows applying a high bias voltage to the electrode n and
 835 for this reason the flavor D is also called "HV flavor". Unfortunately the "HV" suffer
 836 from a signal loss, which can achieve even the 50%, due to the additional parasitic capac-
 837 ity introduced at the input node. The HV voltage above which the breakdown begins is
 838 ~ 50 V; however at values bigger than 20 V, the gain does not increase anymore, since the
 839 depletion zone is already fully depleted.

838 3.2.1 ALPIDE-like

840 ALPIDE chips, developed by the ALICE collaboration, implemented a standard FE to the
 841 point that many CMOS MAPS detectors used a similar FE and are called "ALIPDE-like".
 842 Considering that both TJ-Monopix1 and ARCADIA-MD1 have an ALPIDE-like FE, I am
 843 going to explain the broad principles of the early FE stage. The general idea is of the
 844 amplification to transfer the charge from a bigger capacity[15], C_{source} , to a smaller one,

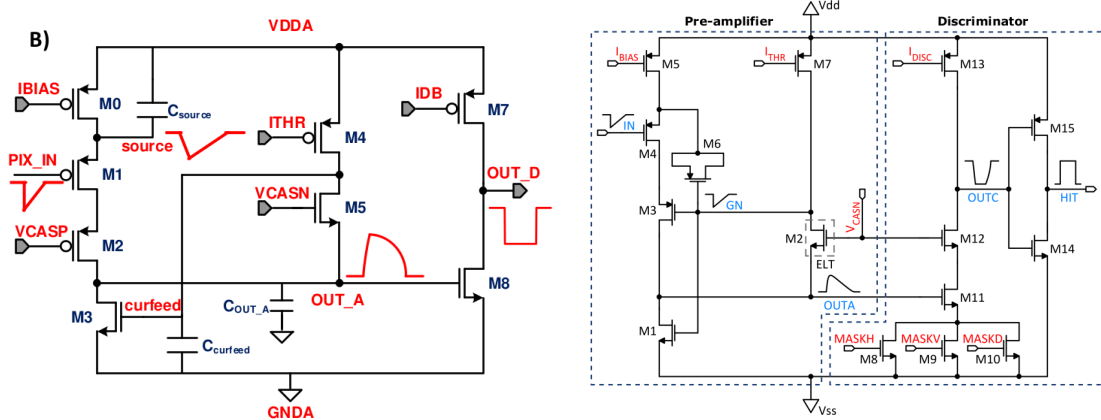


Figure 3.5

844 C_{out} : the input transistor M1 with current source IBIAS acts as a source follower and this
 845 forces the source of M1 to be equal to the gate input $\Delta V_{PIX_IN} = Q_{IN}/C_{IN}$.

$$Q_{source} = C_{source} \Delta V_{PIX_IN} \quad (3.3)$$

846 The current in M2 and the charge accumulates on C_{out} is fixed by the one on C_{source} :

$$\Delta V_{OUT_A} = \frac{Q_{source}}{C_{OUT_A}} = \frac{C_{source} \Delta V_{PIX_IN}}{C_{OUT_A}} = \frac{C_{Source}}{C_{OUT_A}} \frac{Q_{IN}}{C_{IN}} \quad (3.4)$$

847 A second branch (M4, M5) is used to generate a low frequency feedback, where VCASN
 848 and ITHR set the baseline value of the signal on C_{OUT_A} and the velocity to goes down
 849 to the baseline. **IL RUOLO DI CURVFEED NON L'HO CAPITO.** Finally IDB defines
 850 the charge threshold with which the signal OUT_A must be compared: depending on if
 851 the signal is higher than the threshold or not, the OUT_D is high or low respectively.

852 The actual circuit implemented in TJ-Monopix1 is shown in figure 3.5: the principal
 853 difference lays in the addition of disableing pixels' readout. This possibility is uttermost
 854 important in order to reduce the hit rate and to avoid saturating the bandwidth due to the
 855 noisy pixels, which typically are those with manufacturing defects. In the circuit transis-
 856 tors M8, M9 and M10 have the function of disabling registers with coordinates MASKH,
 857 MASKV and MASKD (respectively vertical, orizontal and diagonal) from readout: if all
 858 three transistors-signals are low, the pixel's discriminator is disabled. Compared with a
 859 configurable masking register which would allow disableing pixels individually, to use a
 860 triple redundancy reduces the sensistivity to SEU but also gives amount of intentionally
 861 masked ("ghost") pixels. This approach is suitable only for extremely small number N of
 862 pixel has to be masked: if two coordinate projection scheme had been implemented, the
 863 number of ghost pixels would have scale with N^2 , if instead three coordinates are used,
 864 the N's exponential is lower than 2 (fig. 3.6)

865 Foto dell'oscilloscopio per far vedere cosa fanno i parametri

866 3.3 Readout logic

867 TJ-Monopix1 has a triggerless, fast and with ToT capability R/O which is based on a
 868 column-drain architecture. On the pixel are located two Random Access Memory (RAM)
 869 cells to store the 6-bit LE and 6-bit TE of the pulse, and a Read-Only Memory (ROM)

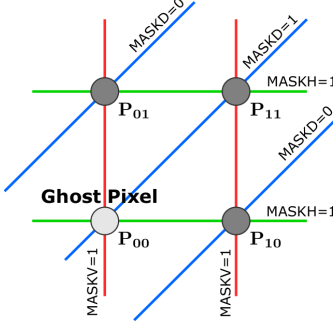


Figure 3.6

Parameter	Meaning	
IBIAS	mainly controls the rise time	yes
IDB	sets the discriminator threshold	yes
ITHR	sets the velocity of the return to the baseline	yes
ICASN	sets the baseline of the signal	yes
VRESET	sets the gain of the preamplifier	yes
IRESET	sets the gain of the preamplifier	no

Table 3.3: FE parameters which must be setted through the DAQ. "Function" means that higher parameter implies higher value

containing the 9-bit pixel address. Excluded these memories, TJ-Monopix1 hasn't any other buffer: if a hit arrives while the pixel is already storing a previous one, the new data get lost. After being read, the data packet is sent to the EoC periphery of the matrix, where a serializer transfers it off-chip to an FPGA (3.7). There a FIFO is used to temporarily stored the data, which is transmitted to a computer through an ethernet cable in a later time.

The access to the pixels' memory and the transmission of the data to the EoC, following a priority chain, is managed by control signals and is based on a Finite State Machine (FSM) composed by four state: no-operation (NOP), freeze (FRZ), read (RD) and data transfer (DTA). The readout sequence (??) starts with the TE of a pulse: the pixel immediately tries to grab the column-bus turning up a hit flag signal called *token*. The token is used to control the priority chain and propagates across the column indicating what pixel that must be read. To start the readout and avoid that the arrival of new hits disrupt the priority logic, a *freeze* signal is activated, and then a *read* signal controls the readout and the access to memory. During the freeze, the state of the token for all pixels on the matrix remains settled: this does not forbid new hits on other pixels from being recorded, but forbids pixels hit from turning on the token until the freeze is ended. The freeze stays on until the token covers the whole priority chain and gets the EoC: during that time new token cannot be turned on, and all hits arrived during a freeze will turn on their token at the end of the previous freeze. Since the start of the token is used to assign a timestamp to the hit, the token time has a direct impact on the time resolution measurement; this could be a problem coping with high hits rate.

The analog FE circuit and the pixel control logic are connected by an edge detector which is used to determine the LE and the TE of the hit pulse(fig. 3.9): when the TE

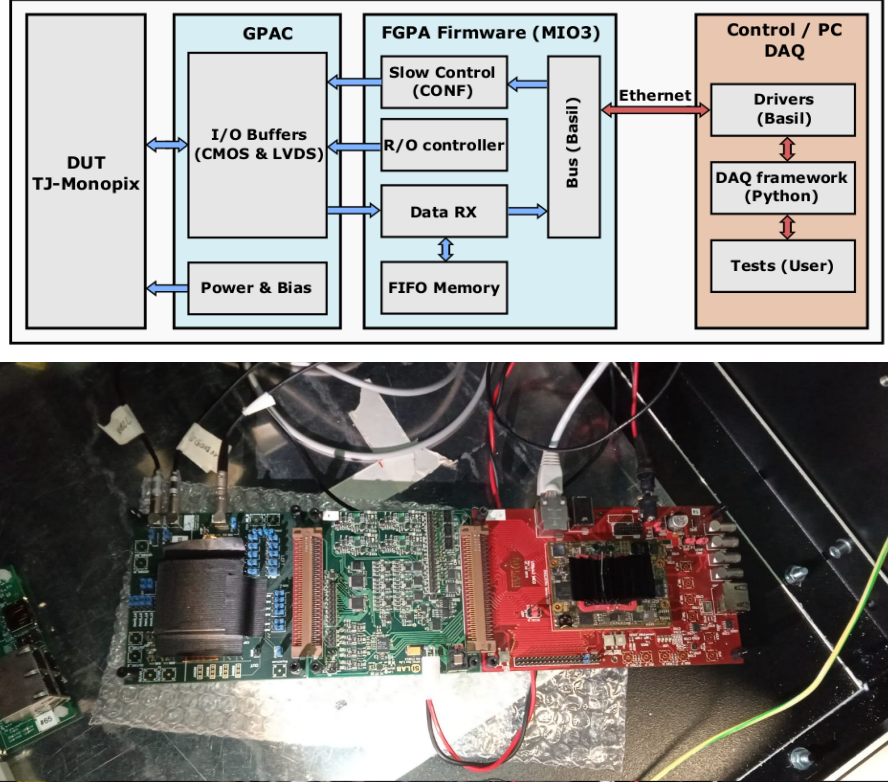
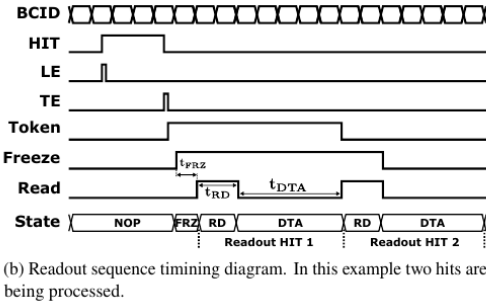


Figure 3.7: Main caption



(b) Readout sequence timing diagram. In this example two hits are being processed.

Figure 3.8: Readout timing diagram: in this example two hits are being processed

is stored in the first latch the edge detector is disabled and, if the **FREEZE** signal is not set yet, the readout starts. At this point the **HIT** flag is set in a second latch and a **Token** signal is produced and depending on the value of **Token** in the pixel can be read or must wait until the **Token in** is off. In figure an OR is used to manage the token propagation, but since a native OR logic port cannot be implemented with CMOS logic, a sum of a NOR and of an inverter is actually used; this construct significantly increases the propagation delay (the timing dispersion along a column of 0.1-0.2 ns) of the token and to speed up the circuit optimized solution are often implemented. When the pixel become the next to be read in the queue, and at the rising edge of the **READ** signal, the state of the pixel is stored in a D-latch and the pixel is allowed to use the data bus; the **TE** and the **HIT** flag latches are reset and a **READINT** signal that enable access of the RAM and ROM cells is produced.

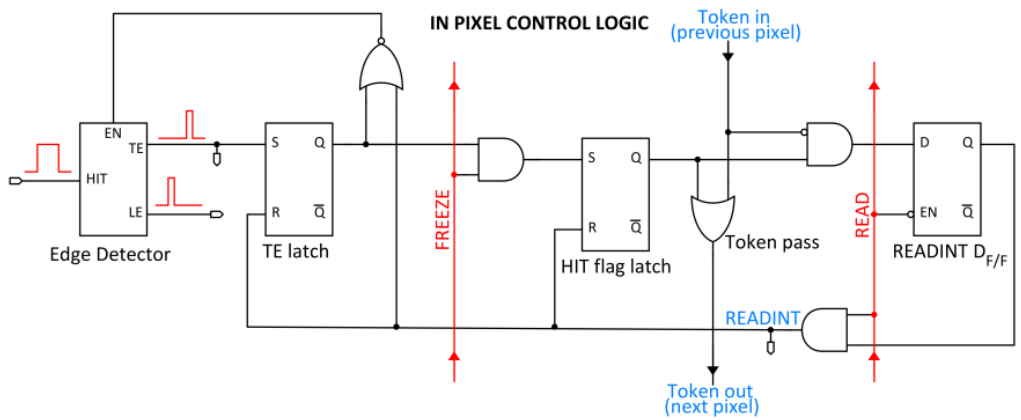


Figure 3.9

906 The final data must provide all the hits' information: the pixel address, the ToT and
907 the timestamp. All those parts are assigned and appended at different time during the
908 R/O chain:

- **Pixel address:** while the double column address (6-bit) is appended by the EoC circuit, the row address (8-bits for each flavor) and the physical column in the doublet (1-bit) are assigned by the in-pixel logic
 - **ToT:** is obtained offline from the difference of 6-bits TE and 6-bits LE, stored by the edge detector in-pixel; since a 40 MHz BCID is distributed across the matrix, the ToT value is range 0-64 clock cycle which corresponds to 0-1.6 μ s
 - **Timestamp:** The timestamp of the hit correspond to the time when the pixel set up the token; it is assigned by the FPGA, that uses the LE, TE and a 640 MHz clock to derive it. For all those hits which arrived while the matrix is frozen, the timestamp is no more correlated with the time of arrival of the particle

When the bits are joined up together the complete hit data packet is 27-bit.

920 **Chapter 4**

921 **Arcadia-MD1**

922 [16] [17]

923 Breve introduzione analoga a Monopix1 in cui descrivo brevemente la "timeline" da
924 SEED Matisse a Md1 e Md2

925 Tutti i minid, siano essi v1 o v2, sono Alpide like. Prima SEED si occupa di stu-
926 diare le prestazioni: concept study with small-scale test structure (SEED), dopo arcadia:
927 technology demonstration with large area sensors Small scale demo SEED(sensor with em-
928 bedded electronic developement) Quanto spazio dato all'elettronica sopra il pwell e quanto
929 al diodo. ..

930 **4.1 The sensor**

931 ARCADIA-MD1 is an LFoundry chip which implements the technology 110 nm CMOS
932 node with six metal layer ??. The standard p-type substrate was replaced with an n-type
933 floating zone material, that is a tecnique to produce purified silicon crystal. (pag 299
934 K.W.).

935 Tra i wafer fabbricati finora ci sono 3 valori di spessore attivo nominale (lo spessore
936 effettivo può variare di qualche micron ripetto a quello nominale): 48um, 100um e 200um.
937 In allegato un'immagine con le cross section.

938 Wafer thinning and backside lithography were necessary to introduce a junction at the
939 bottom surface, used to bias the substrate to full depletion while maintaining a low voltage
940 at the front side.

941 C'è un deep pwell per - priority chain separare l'elettronica dal sensore; per controllare il
942 punchthought è stato aggiunto un n doped epitaxial layer having a resistivity lower than
943 the substrate. It is part of the cathegory of DMAPS Small electrode to enhance the signal

Parameter	Value
Matrix size	$\times \text{ cm}^2$
Pixel size	$25 \times 25 \mu\text{m}^2$
Depth	? μm
Electrode size	$9 \times 9 \mu\text{m}^2$
Power consumption	$\sim \text{ mW/cm}^2$

Table 4.1

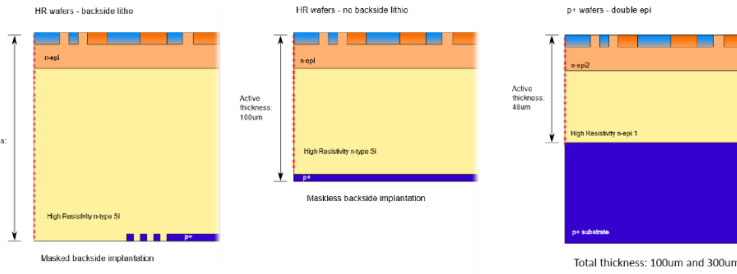


Figure 4.1

944 to noise ratio. It is operated in full depletion with fast charge collection by drift.

945 4.1.1 Two different FE flavor

946 Le differenze tra Alpide e bulk driven sono un po' più complesse di quanto hai scritto.
 947 Si tratta proprio di due architetture diverse. Il primo amplifica il segnale attraverso il
 948 trasferimento di carica tra due capacità. Nel bulk driven invece il guadagno è dato dal
 949 rapporto tra due transconduttanze. Inoltre ci sono altre differenze, il bulk driven è più
 950 sensibile alle cadute di tensione sul ground (che ahimè è esattamente ciò che accade nei
 951 dimostratori che abbiamo ora, a causa dell'anomalo consumo di corrente dal digitale,
 952 altro baco che abbiamo corretto nella terza sottomissione). Anche i livelli di tensione nei
 953 nodi interni dei due front-end differiscono e il meccanismo di clipping che funzionava per
 954 l'Alpide non è applicabile al bulk driven. Di conseguenza abbiamo un bias in più (ICLIP)
 955 nel secondo flavour per controllare il clipping. Nell'Alpide il clipping c'è, ma l'architettura
 956 usata permette di non aver bisogno di un bias esterno, anche se in una versione di Alpide
 957 di ALICE hanno scelto di controllare comunque la corrente di clip esternamente, per una
 958 maggiore flessibilità. Infine alcuni bias che hanno lo stesso nome nei due flavour, perché
 959 svolgono la stessa funzione, differiscono nel valore di configurazione didefault.

960 4.2 Readout logic and data structure

961 In order to achieve the lowest possible power consumption, the matrix is clockless, no
 962 free-running clock, and to save as much area as possible, it will not buffer any hits, and
 963 its readout will thus be triggerless.

964 The Periphery has both an analog part, segmented per Section, and a digital part,
 965 which is instead shared. The analog part hosts the bias cells for the AFE dei pixel, mentre
 966 la parte digitale che è unica per tutti riprocesso le hit che vengono dalle sezioni e 8b10b
 967 encode le parole per data transmission.

968 4.2.1 Matrix division and data-packets

969 The matrix is divided into an internal physical and logical hierarchy: The 512 columns are
 970 divided in 16 section: 512×32 pixels, each section has different voltage-bias + serializzatori.
 971 Each section is devided 512×2 column, and in 32×2 core: in modo che in ogni doppia
 972 colonna ci siano 1Pacchetto dei dati 6 cores. ricordati dei serializzatori: sono 16 ma
 973 possono essere ridotti ad uno in modalità spazio Ed infine regioni da 4×2 . The readout
 974 design must be capable of addressing the following matters Enough bus bandwidth for a

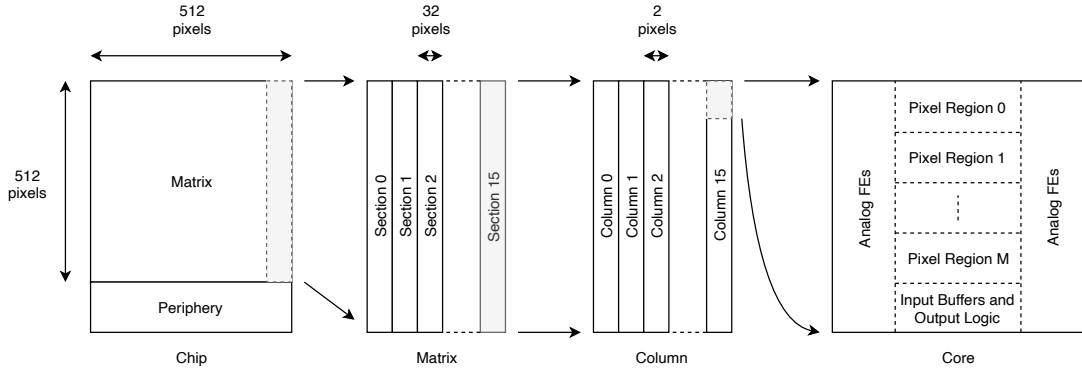


Figure 4.2

hit rate of 100 MHz/cm². Design decisions: Try and send as much data as possible to the periphery (bandwidth) Lowest amount of logic possible (more routability)

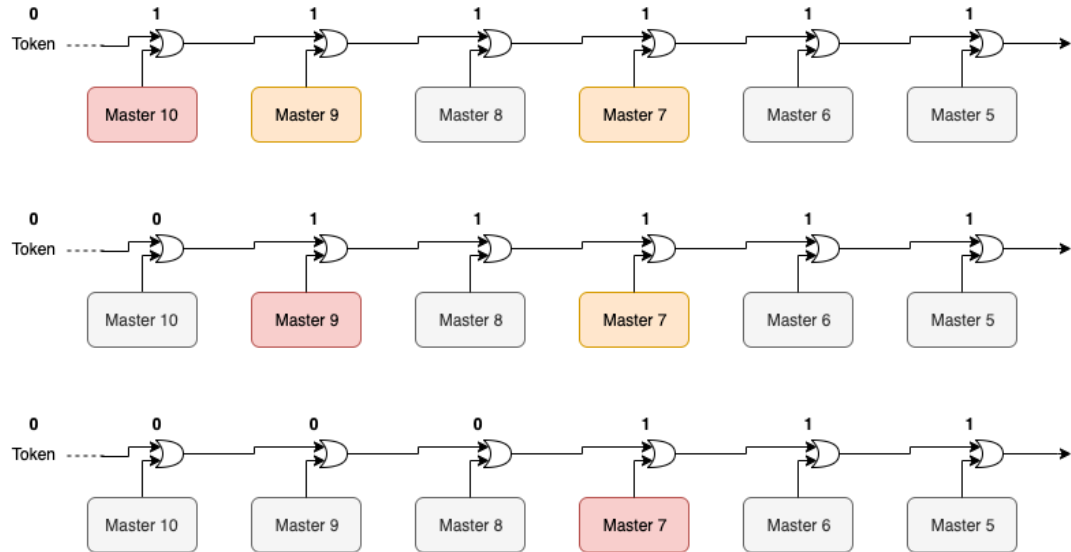


Figure 4.3

Questo divisione si rispecchia in come sono fatti i dati: scrivi da quanti bit un dato è fatto e le varie coordinate che ci si trovano dentro; devi dire che c'è un pixel hot e spieghi dopo a cosa serve, e devi accennare al timestamp

"A core is simply the smallest stepped and repeated instance of digital circuitry. A relatively large core allows one to take full advantage of digital synthesis tools to implement complex functionality in the pixel matrix, sharing resources among many pixels as needed.". pagina 28 della review.

984

985 TABELLA: con la gerarchia del chip Matrix (512x512 pixels) Section (512x32 pixels)
986 Column (512x2) Core (32x2) Region (4x2)

987 Nel chip trovi diverse padframe: cosa c'è nelle padframe e End of section.

988 "DC-balance avoids low frequencies by guaranteeing at least one transition every n
989 bits; for example 8b10b encoding n =5"

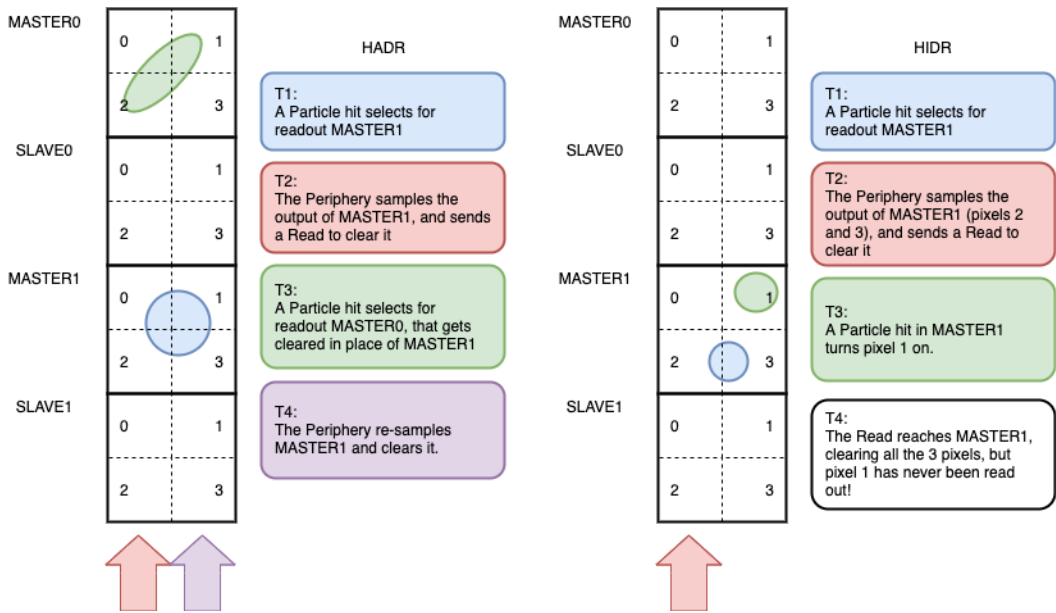


Figure 4.4

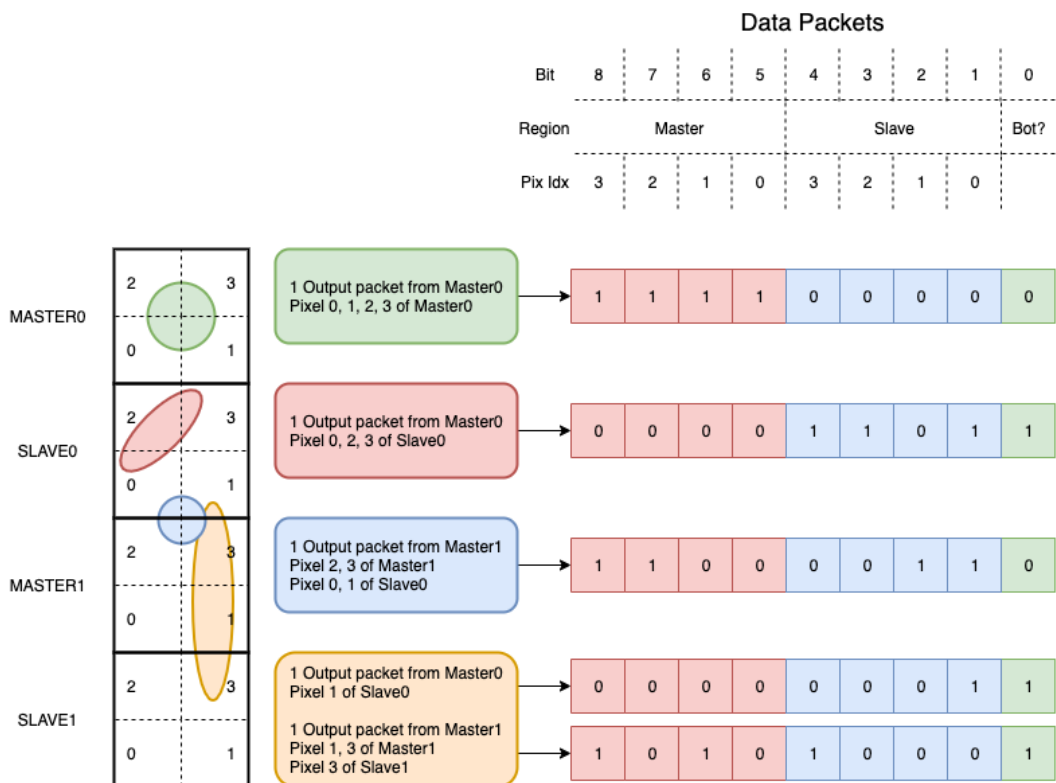


Figure 4.5

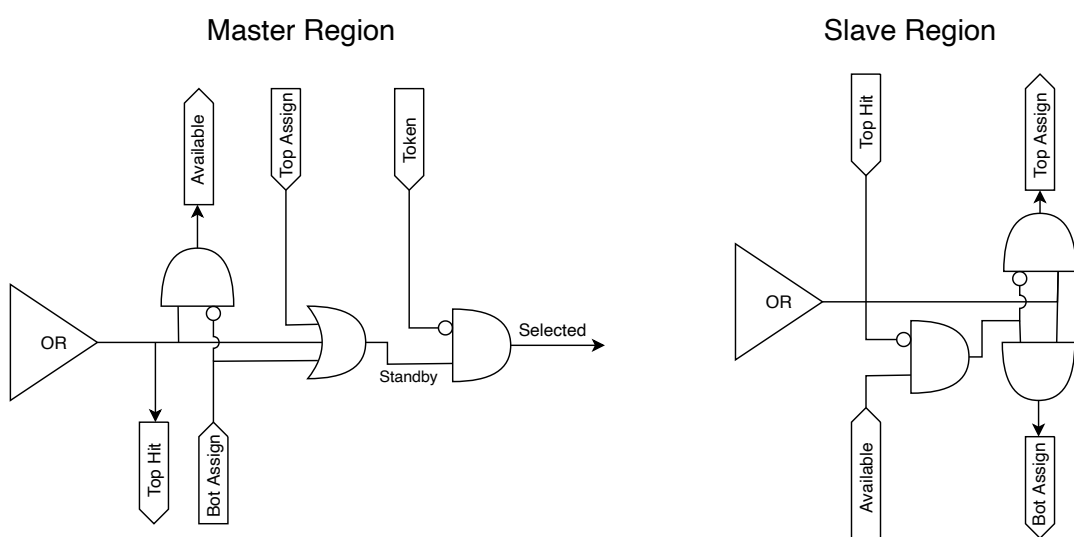


Figure 4.6

990 Chapter 5

991 Characterization

992

- 993 • rifai il conto della lunghezza di attenuazione. Ho trovato (presentazione Luciano
- 994 Mus) 29 um per ka e 37 um per kb.
- 995 • Con il PMOS la configurazione del FE di default è: e richiama i significati delle
- 996 variabili.
- 997 • parla dell HV

998 5.1 TJ-Monopix1 characterization

999 5.1.1 Threshold and noise: figure of merit for pixel detectors

1000 A characterization of threshold and noise is typically necessary since these values have an
1001 impact on the operating conditions and on the performance of the chips, so much that
1002 the signal to threshold ratio may be considered as the figure of merit for pixel detectors
1003 rather than the signal to noise ratio. The mean minimum stable threshold evolved through
1004 different generation of chips: in the 1st generation it was around 2500 e^- while in the 3rd
1005 (corresponding to nowadays chips) is less than 500 e^- . This allows in thinner sensors with
1006 smaller signals: from $16\,000\text{ e}^-$ produced in $200\text{ }\mu\text{m}$, the signal expected moved down to
1007 2000 e^- produced in $25\text{ }\mu\text{m}$. According with this, the threshold of TJ-Monopix1 is around
1008 500 e^- .

1009 Obviously the threshold has to be located between the noise peak around the baseline
1010 and the signal distribution, in particular it has to be low enough to mantain a high signal
1011 efficiency, but also high enough to cut the noise: for a low threshold many pixels can fire
1012 at the same time and a positive feedback can set off a chain reaction eventually, causing
1013 all the other pixels to fire. Thus, the noise sets a lower bound to the threshold: if an
1014 occupancy $\leqslant 10^{-4}$ is required, for example, this correspond to the Gaussian 1-sided tail
1015 fraction for 3.7σ . In this case, if the noise is 100 e^- (resonable), the threshold must be
1016 higher than $3.7 \times 100\text{ e}^-$. Typically this argument sets only a minimal bound to the
1017 threshold since the variation with time and from pixel to pixel have to be taken into
1018 account: the temperature, the annealing (for example, the radiation damages in the oxide
1019 layer causes shift of MOSFET threshold voltage) and the process parameters variation
1020 across the wafer (as for example process mismatch between transistors).

Given that the first stage of amplification is the most crucial, since in the following stages the signal amplitude is high compared to additional noise, the noise is valued at the preamplifier input node. Then, the noise is parameterized as Equivalent Noise Charge (ENC), which is defined as the ratio between the noise N at the output expressed in Volt and the out voltage signal S produced by 1 e⁻ entering in the preamplifier:

$$ENC = \frac{N_{out}[V]}{S_{out}[V/e^-]} = \frac{V_{noise}^{RMS}}{G} \quad (5.1)$$

with G expressed in V/e⁻; as the gain increases, the noise reduces . **Servirebbe una misura**
Considering the threshold dispersion a requirement for the ENC is:

$$ENC < \sqrt{(T/3.7)^2 - T_{RMS}^2(x) - T_{RMS}^2(t)} \quad (5.2)$$

where the T is the threshold setted, T_{RMS} is the threshold variation during time (t) and across the matrix (x); a typical reasonable value often chosen is 5 ENC.

Because of the changing of the 'real' threshold, the possibility of changing and adapting the setting parameters of the FE, both in time and in space is desiderable: these parameters are usually set by Digital to Analog Converter (DAC) with a number of bit in a typical range of 3-7. Unfortunately DAC elements require a lot of space that may be not enough on the pixel area; therefore, the FE parameters are typically global, which means that they are assigned for the whole chip, or they can be assigned for regions the matrix is divided into. The former case corresponds to TJ-Monopix1's design in which 7 bits are used for a total 127-DAC possible values, while the latter corresponds to the ARCADIA-MD1's one, **where quanti bit??**. An other possibility, for example implemented in TJ-Monopix2, is allocate the space on each pixel for a subset of bits, then combinig the global threshold with a fine tuning. If so, the threshold dispersion after tuning is expected to be inversely proportional to the tuning DAC number of bits and thus be improved a lot:

$$\sigma_{THR,tuned} = \frac{\sigma_{THR}}{2^{nbit}} \quad (5.3)$$

where σ_{thr} is the RMS of the threshold spread before tuning.

To measure the threshold and noise of pixels a possible way is to make a scan with different known injected charge: the threshold corresponds to the value where the efficiency of the signal exceeds the 50%, and the ENC is determined from the width of this edge. Following this path, I have used the injection circuit available on the chip to inject 100 pulses for each input charge for a fixed threshold. The injection comes on a capacity at the input of the FE circuit, whose mean value is 230 aF and from which the conversion factor from DAC units to electrons can be obtained: for the PMOS flavor, for example, since the DAC are biased at 1.8 V, the Least significant Bit (LSB) corresponds to a voltage of 14.7 mV from which the charge for LSB 1.43 e⁻/mV and the conversion factor therefore is 20.3 e⁻/DAC. While this value is equivalent for all the PMOS flavor, the HV flavor is expected to have a different conversion factor, ~ 33 e⁻/DAC, beacuse of the different input capacity.

Besides the charge, also the duration and the period of the injection pulse can be set; it is important to make the duration short enough to have the falling edge during the dead time of the pixel (in particular during the FREEZE signal) in order to avoid the undershoot, coming at high input charge, triggering the readout and reading spurious hits. Since the injection circuit is coupled in AC to the FE, if the falling edge of the pulse is sharp enought to produce ad undershoot, this can be seen as a signal.

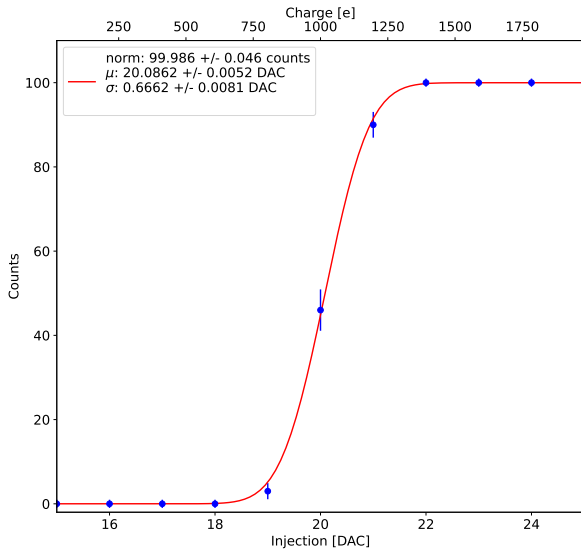


Figure 5.1: S-curve for pixel (10, 10) of the PMOS flavor (flavor 1) with IDB fixed at 40 DAC. The conversion of charge injected from DAC to electrons has been done assuming a conversion factor of 20 e-/DAC.

	PMOS A	PMOS B	PMOS C	HV
Threshold [e-]	401.70 ± 0.15	511.0 ± 1.0	539.66 ± 0.58	403.87 ± 0.19
Threshold dispersion [e-]	32.90 ± 0.11	36.96 ± 0.66	55.54 ± 0.42	44.67 ± 0.15
Noise [e-]	13.006 ± 0.064	16.444 ± 0.086	13.88 ± 0.11	11.68 ± 0.10
Noise dispersion [e-]	1.608 ± 0.044	1.95 ± 0.06	1.906 ± 0.072	1.580 ± 0.068

Table 5.1: Mean threshold and noise parameters for all flavor and their dispersion on the matrix.

Assuming a gaussian noise, the efficiency of detecting the signal can be described through a modification of the error function:

$$f(x, \mu, \sigma) = \frac{1}{2} \left(1 + \operatorname{erf} \left(\frac{x - \mu}{\sigma\sqrt{2}} \right) \right) \quad (5.4)$$

with: where the threshold and the ENC corresponds to the μ and σ . Therefore I perform a fit of the counts detected using the function in equation 5.4. In figure 5.1 there is an example with IDB equal to 40 DAC of fit for a pixel belonging to the flavor B, while in table ?? and figure ?? there are the histograms and the maps of the parameters of the scurve-fit. As expected, the flavor PMOS reset gated (A), thanks to the transistor which change the baseline value, has a lower threshold and noise

Small threshold variations has been observed in the first biasing section (columns from 0 to 14) with IDB=40 DAC; the same structure appears more evident at other different IDBs, as for example 100 DAC Plot of the average threshold per column al variare di IDB. The systematic threshold variation across the biasing group has not a known motivation, but one could certainly be the transistor mismatch of the biasing DAC registers IDB and ICASN, which both adjust the effective threshold (I recall that ICASN regulate the baseline, and in this measurements it was set to the minimin possible value).

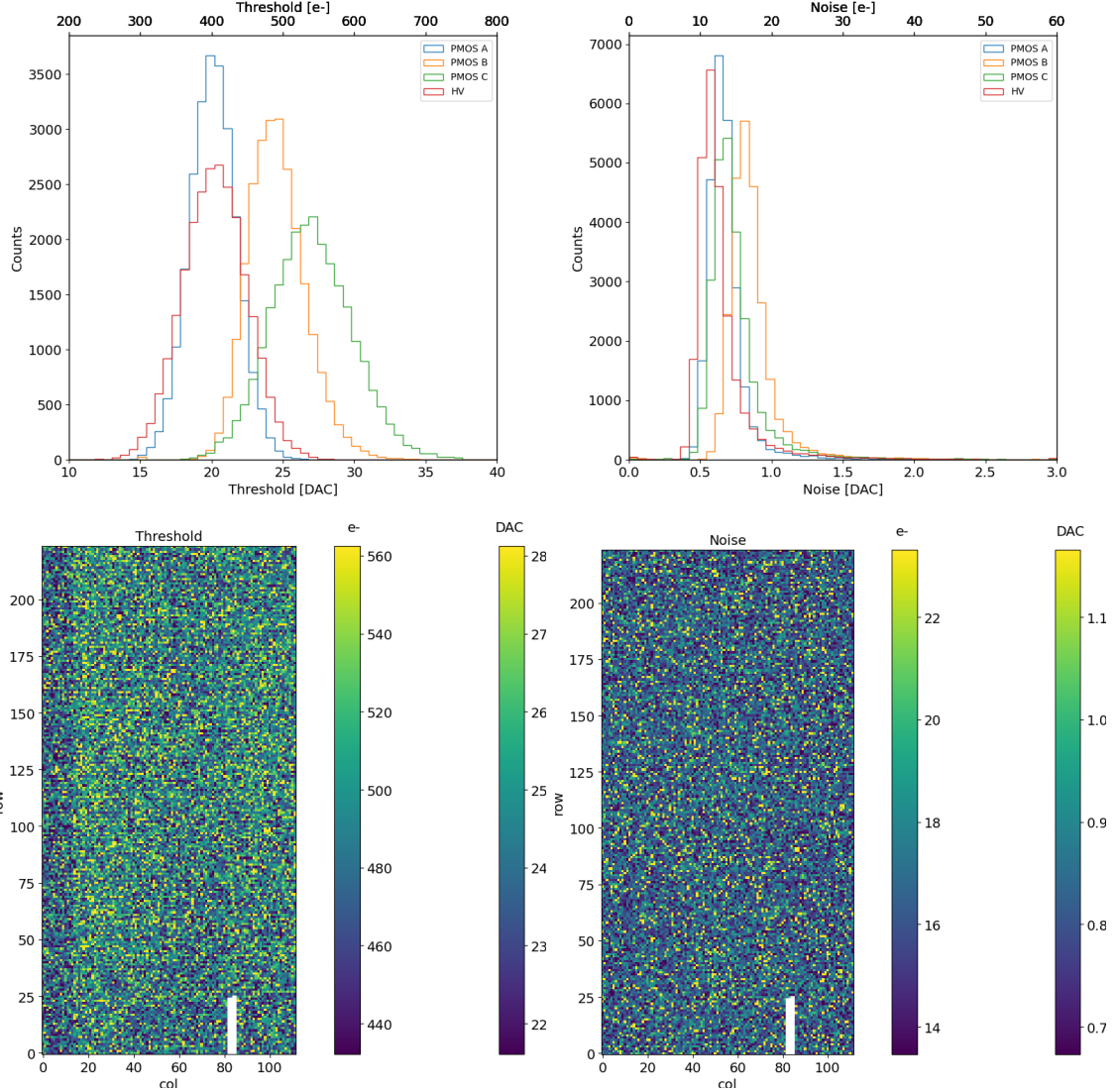


Figure 5.2: Histograms of the threshold (a) and the noise (b) found fitting the s-curve of all flavor with IDB fixed at 40 DAC. Below there are the maps of the threshold (a) and the noise (b), respectively, found fitting the s-curve with IDB fixed at 40 DAC for the PMOS flavor (B). The white pixels have the injection circuit broken.

1076 To verified the trend of the threshold as a function of the front end parameter IDB and
 1077 find its dynamic range, I have permormed different scans changing the IDB: I have injected
 1078 the whole matrix and found the means and the standard deviation of the distributions. The
 1079 results are shown in figure 5.3: the blue points are the mean threhsold found whithin the
 1080 matrix, while in green is shown the width of the threshold distribution, aka the threshold
 1081 dispersion. While the threshold increases, the ENC decreases of $\sim 4 \text{ e-}$,which is $\sim 1/3$ of
 1082 the noise at IDB=40 DAC.

1083 Then, to evaluet the operation and the occupancy of the chip at different threshold
 1084 I have made long acquisitions of noise at different IDB and check how the number of
 1085 pixel masked changes with the threshold. The masking algorithm I have used search for
 1086 pixels with rate $> 10 \text{ Hz}$ and mask them. With such algorithm, in our standard condition,
 1087 IDB=40 DAC, a very low noise hit rate is intentionally achieved masking only dozen of

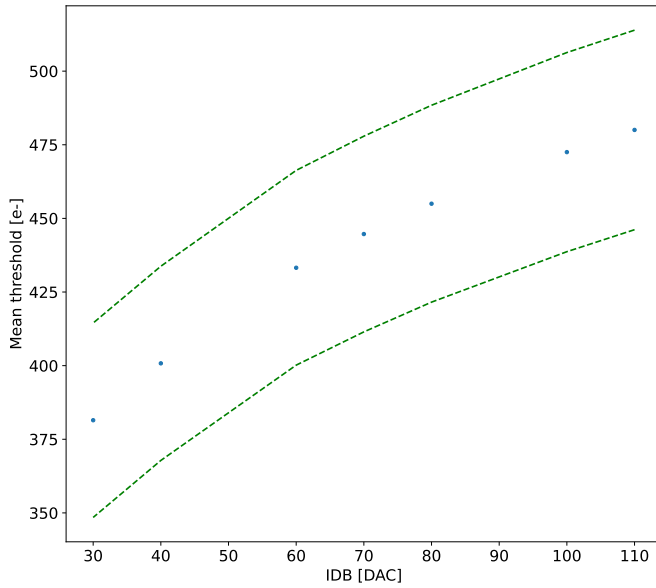


Figure 5.3: Flavor PMOS (B) with Psub-Pwell biased at -6 V. Threshold measured in electrons vs the register which sets the threshold, IDB.

1088 pixels? of the whole flavor, and other quanti are unintentionally masked.

1089 5.1.2 Linearity of the ToT

1090 I have already said in chapter 3 that TJ-Monopix1 returns an output signal proportional to
1091 the charge released by a particle in the epitaxial layer, which is the Time over Threshold;
1092 the ToT is saved as a 6-bit variable and then has a dynamic range equal to 0-64, which
1093 corresponds to 0 μ s to 1.6 μ s assuming a clock frequency of 40 MHz. When a pulse is longer
1094 than 1.6 μ s the counter rolls back to zero and there is no way to distinguish that charge
1095 from a lower one with the same ToT: that is the rollover of the ToT (??(a)).

1096 In order to associate the ToT (in range 0-64) to the charge, a calibration of the signal
1097 is necessary. Assuming the linearity between ToT and the charge, Q can be found:

$$Q [DAC] = \frac{(ToT [au] - q [au])}{m [au/DAC]} \quad (5.5)$$

1098 where m and q are the fitted parameters of the calibration. It is important to keep in mind
1099 that the main application target of TJ-Monopix1 is in the inner tracker detector of HEP
1100 experiments, then the main feature is the efficiency, then a rough calibration of the signal
1101 to charge is fine. The ToT information can be used both to better reconstruct the charge
1102 deposition in cluster in order to improve the track resolution, and for particle identification,
1103 especially for low momentum particles which do not reach the proper detectors.

1104 The study of the output signal is made possible via the injection: since the pulses are
1105 triangular, the ToT is expected to be almost linear depending on the injection charge value.
1106 To verify this statement and study the deviations from linearity I've fit the ToT versus the
1107 charge injected for all pixel within the matrix. In figure ??(b) there is an example of fit
1108 for a pixel belonging to the flavor B, while in figure 5.5 there are the histograms and the

maps of the parameters of the line-fit for all flavors with IDB fixed at 40 DAC. Here again a difference between biasing section appears: since the slope of the ToT is related with the gain of the preamplifier (increasing the gain also increases the ToT), the mismatch is probably due to the transistor contributing to the amplification stage.

Before performing the fit I have calculated the mean value of the ToT of the pulses recorded for each pulse amplitude and I used the mean ToT as value for the fit. The aim of the calibration obviously is finding a relation only in the range 0-64 without taking into account the rolling over hits: therefore, to prevent the rollover data from reducing the mean ToT introducing a bias in the mean value, I cut and I did not consider them. If a signal bigger than the 1.6 μ s is expected in the usage of the detector, the threshold must be raised or the gain reduced, making the expected output signal in range 0-64. In figure ?? (b) are shown both the fits with a line (red) and with a second order polynomial (green): at the bounds of the ToT range values deviate from the line model. Since the deviation is low than 1% and it only interest the region near the 0 and the 64, in first approximation it is negligible.

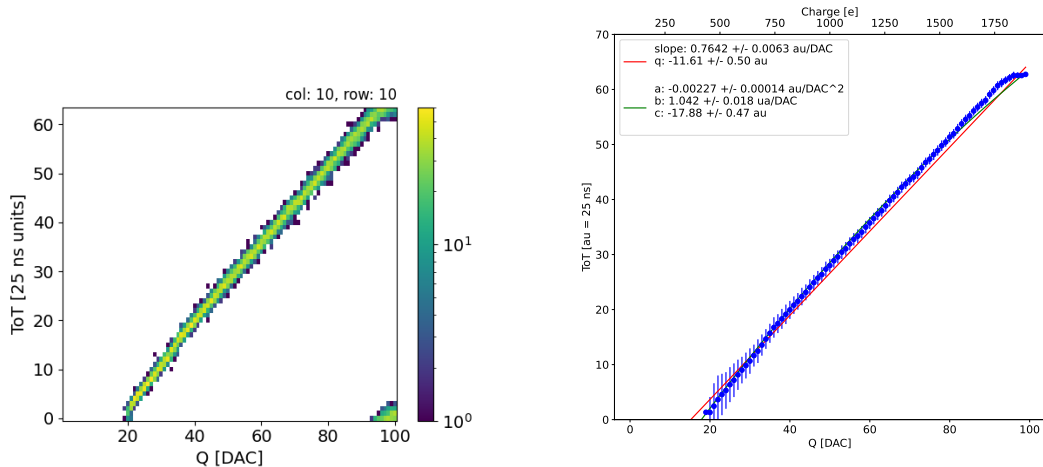


Figure 5.4: The figures refer to pixel (10,10) of the PMOS-reset flavor (1) with IDB fixed at 40 DAC for the PMOS flavor (B). (a) Histogram of the injection pulses: the ToT is in range 0-64 since it is represented by 6 bit, so when achieving the 64 it rolls over back to the zero. (b) Mean ToT vs the the charge: the mean has been calculated cutted the rolling hits.

5.1.3 Calibration of the ToT

Considering that the charge injected in the FE goes to fill capacitor which is different from pixel to pixel, the true charge injected does not correspond to what expected assuming C equal to 230 aF, the nominal value. Accordingly to that, a verification of the value provided and an absolute calibration of this capacity and of the conversion factor F is needed to have a correspondence of the signal in electrons; assuming C 230 aF, F is expected to be $20 \text{ e-}/\text{DAC}$, and is defined as:

$$F [\text{e-} / \text{DAC}] = \frac{1616 \text{ e-}}{Q [\text{DAC}]} \quad (5.6)$$

For this purpose a Fe55 radioactive source has been employed; the Fe55 is an extremely important radionuclide in the calibration of X-ray spectrometers, proportional counter

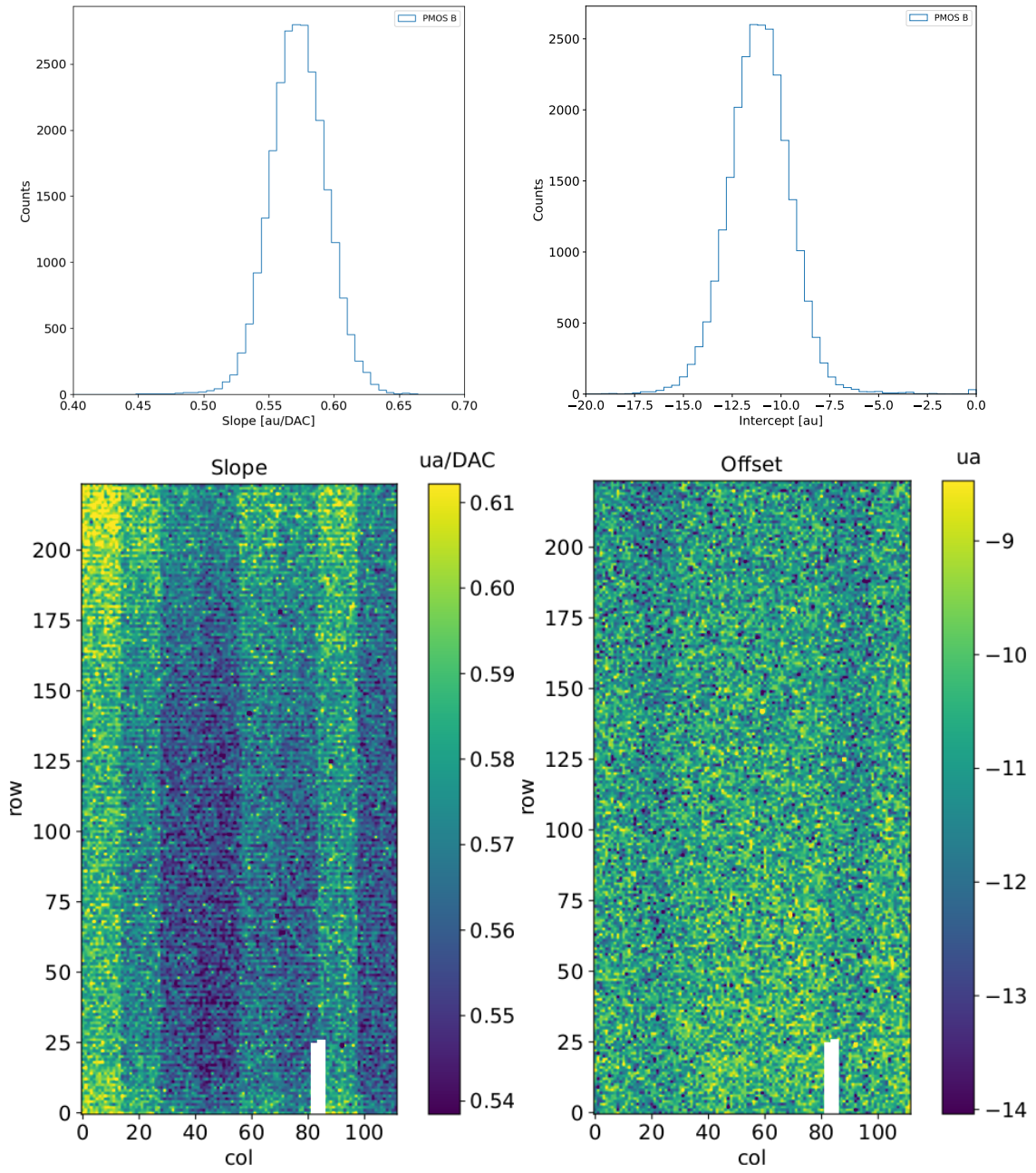


Figure 5.5: Histograms of the calibration parameters, slope (a) and offset (b), found fitting the ToT with a line, for all flavor and with IDB fixed at 40 DAC. Maps of the calibration parameters, slope (a) and offset (b), found fitting the ToT with a line, with IDB fixed at 40 DAC

and scintillator detector since it emits two X-photons during the electron capture decay: the first one (K_{α}) at 5.9 keV and the second one (K_{β}) at 6.5 keV. The K_{α} photon, which does photoelectric effect in the silicium, has an absorption length $\lambda=7 \mu\text{m}$ to $8 \mu\text{m}$, and the probability of being absorbed in the 25 μm thick epitaxial layer is ~ 0.95 . The electron emitted has an energy equal to the photon one, so recalling that the mean energy needed to produce a couple electron-vacuum is 3.65 eV, the signal produced by the Fe55 source is expected to be 1616 e^- . In figures ?? and ?? are shown two histograms of the

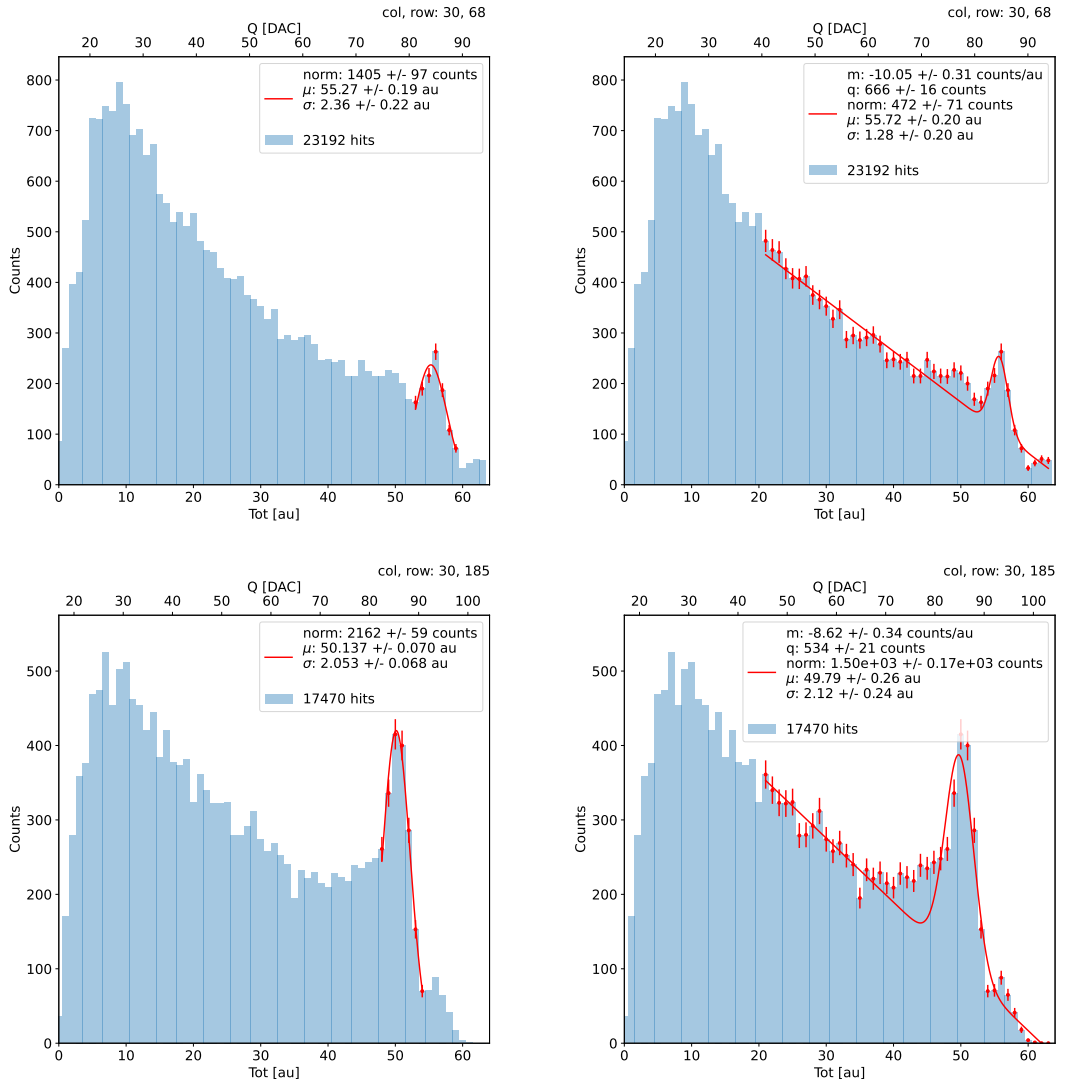


Figure 5.6: due pixel per far vedere la differenza tra i fit. Sottolinea che in rosso ci sono i bin fittati. La doppia scala utilizza le info trovate nel paragrafo precedente per il dato pixel in questione. Per avere una corrispondenza grezza in elettroni basta moltiplicare per 20 e- / dac.

1140 ToT spectrum of the Fe55 source for two different pixels. The peak corresponds to the
 1141 events with completely absorption of the charge produced in the depleted region, while
 1142 the long tail on the left to all the events with partial absorption due to charge sharing
 1143 among neighbors pixels. In order to reduce the charge sharing, the pixel dimension in
 1144 TJ-Monopix2 has been reduced down to $30 \times 30 \mu\text{m}^2$. The events on the right side of the
 1145 peak, instead, corresponds to the K_β photons. Looking at the histograms for pixel (30,
 1146 185) and (30,69) a significant difference in the peak to tail ratio leaps out. This difference
 1147 in the efficiency of detecting the signal can be related with the position of the pixel in
 1148 the matrix: in particular pixels in the upper part of the matrix (rows 112-224) have a
 1149 more prominent peak, while in pixels in the lower part (rows 0-111) there is a higher
 1150 partial absorption. I recall now that there is a slightly difference in the structure of the
 1151 low dose-epi layer (??) among the rows in the matrix, in particular pixels in rows 112-224
 1152 are supposed to have a higher efficiency in the pixel corner.

1153 For the calibration I have need to establish the peak position; to do that I perform a
 1154 fit of the ToT histogram of each pixels. As fit functions I test both the solutions below:

$$f(x, N, \mu, \sigma) = \frac{N}{\sigma\sqrt{2\pi}} e^{-\frac{1}{2}(\frac{(x-\mu)}{\sigma})^2} \quad (5.7)$$

$$f(x, m, q, N, \mu, \sigma) = m x + q + \frac{N}{\sigma\sqrt{2\pi}} e^{-\frac{1}{2}(\frac{(x-\mu)}{\sigma})^2} \quad (5.8)$$

Nel primo caso ho fissato pochi pixel attorno a picco: il range è stato determinato ..

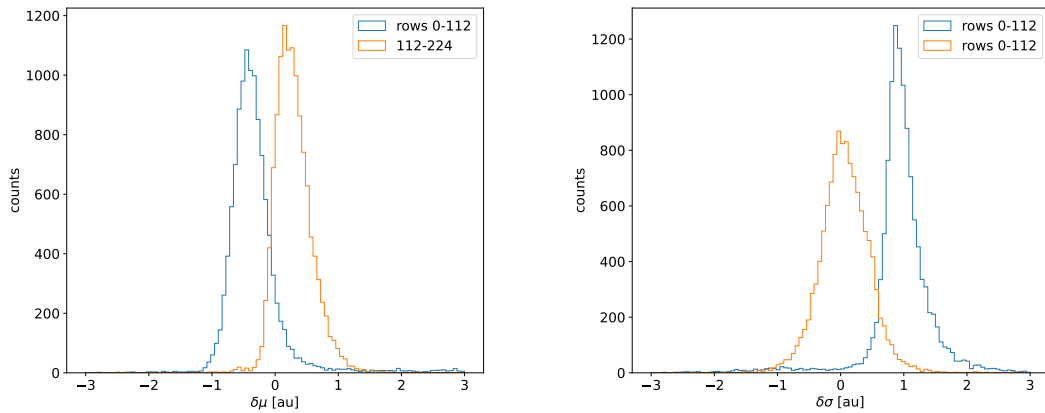


Figure 5.7: Here there are shown the defference between the parameters μ and σ fitted with only a gaussian and with a gaussia plus a line. When $\mu < 0$ the fit function 5.7 has given a worst peak (shifted on the left); when $\sigma < 0$, 5.8 has given a worst peak width (larger sigma)

1155
 1156 **controlla. Nel secondo caso invece il range è.. Controlla sullo script** Even if the difference
 1157 in the peak position between the two cases is not really relevant (5.7) being of the order
 1158 of 0.8-1.5 %, it still introduces a systematic effect moving the peak on the left because of
 1159 the contribution of the tail. Indeed, we know that the sharp edge on the right corresponds
 1160 to the complete absorption of the photon, so excluding the little bump on the right, the
 1161 more the fitted parameter is on the right, the better the fit is. Moreover, there is also
 1162 systematic effect on the peak width, infact the worst fit also gives an overestimation of
 1163 the peak width. Even looking at the χ^2 , the fit function 5.7 seems so be the better choise,
 1164 except for a sample of pixels on the lower part of the matrix, the one with lower efficiency.

1165 Mappa del ferro da cui, come descritto nell'equazione si ricava la capacity. La struttura
 1166 a bande della capacità ha origine nel plot... e quindi nella calibrazione. Andando a vedere
 1167 gli istogrammi di queste due variabili si vedono dei picchi. C'è qualche struttura nella
 1168 matrice che condiziona il funzionamento delle righe? Larghezza della gaussiana: fai il
 1169 discorso a cosa contribuisce ad un picco così largo. è compatibile con quanto ti aspetti?
 1170 The voltage fluctuation around the peak is caused by the number fluctuation of generated
 1171 carriers (Fano noise) and the noise introduced by the detector (sensor and front-end pre-
 1172 amplifier). The ENC can be estimated from the standard deviation of the Kalpha voltage
 1173 distribution. $ENC = \text{sqrt}(\sigma_{\text{misurata}} - \sigma_{\text{aspetti}})$ quella che ti aspetti dal fattore di Fano). E
 1174 è compatibile con quanto trovato? se non fosse compatibile rimaneggia questa frase: tra noise
 1175 is added from the system (test setup) at the analog monitoring pixel output.

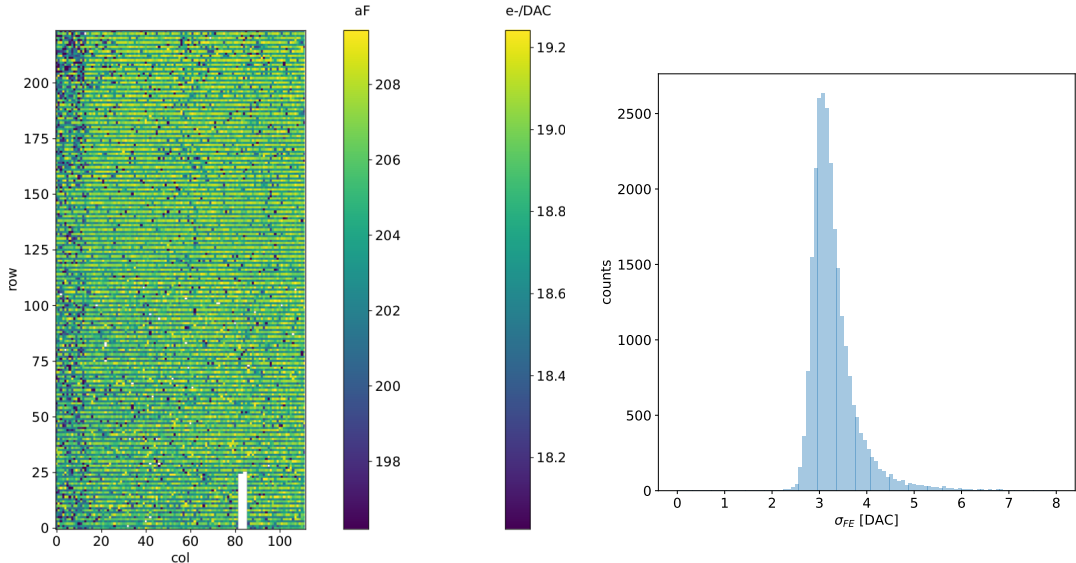


Figure 5.8

1176 5.1.4 Changing the bias

1177 In order to study the behavior of the sensor changing the bias, I perform some injection
 1178 scans in different configurations. The thickness of the depletion has to be considered
 1179 indeed an important parameters for the efficiency of the signal, and in particular it affects
 1180 the charge released by a particle which cross the sensor (since the signal is proportional to
 1181 the thickness of the epitaxial layer). Given that the chip under examination has a gap in
 1182 the low dose epi-layer (look at chapter 3.1) we were not able to change independently the
 1183 bias of the substrate (PSUB) and of the p-well (PWELL), but they must be kept at the
 1184 same value, differently from other chips, where on which some test has been performed, as
 1185 reported in figure 5.9. A 2D map of the measured output voltage amplitude and resulting
 gain in the case of the PMOS and HV are reported.

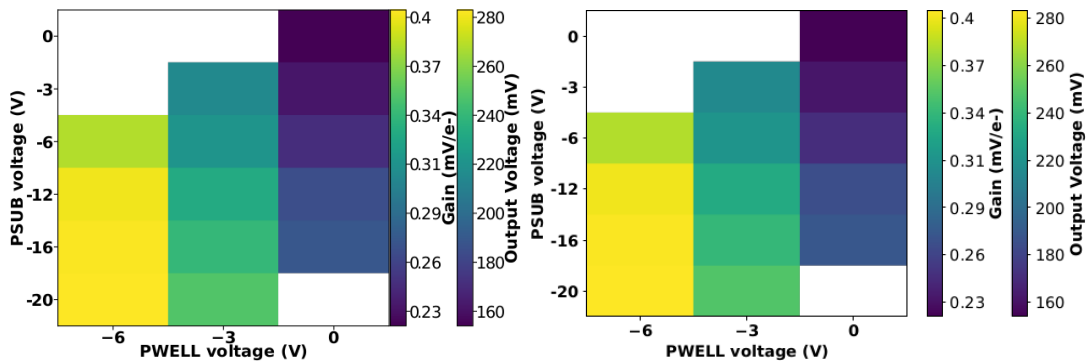


Figure 5.9: 2D map of the output voltage amplitude and gain with respect to the p-well and p-substrate in the case of the PMOS reset front-end (B)

1186
 1187 In order to test the behavior of the chip when not completely depleted, I have performed
 1188 an injection scan with PSUB/PWELL bias at 0 V, -3 V and -6 V, and some acquisitions
 1189 with the Fe55 source. The results of the measurements are reported in table 5.2 and in
 1190 figure ???. Turning down the bias, the depletion region narrows and the efficiency reduces,
 1191 in particular in the pixel corner; in particular the threshold increases of $\sim 1/4$, the noise

	-6 V	-3 V	0 V
Threshold [DAC]	20.04 ± 1.6	21.0 ± 1.6	24.5 ± 1.8
Noise [DAC]	0.613 ± 0.075	0.625 ± 0.078	0.822 ± 0.098
Slope [au/DAC]	0.726 ± 0.027	0.707 ± 0.028	0.573 ± 0.021
Offset [au]	-10.8 ± 1.9	-11.2 ± 1.8	-11.1 ± 1.5

Table 5.2: The errors are the standard deviations of the corresponding distributions. The conversion factor from DAC to electrons is $\sim 20 \text{ e}^-/\text{DAC}$.

of $\sim 1/3$ and the slope, which parameterizes the linearity of the analog output and strictly depends on the gain, decreases of $\sim 1/4$. In figure 5.10(b) are reported the values of the K_α peak position, the normalization of the events above the peak and the rate, everything has been normalized to the value at the reference condition, which is with PSUB/PWELL at -6 V. In order to evaluate the peak position and the normalization I have fit the spectrum in the region on the right with a gaussian. Looking at the spectrum, an other characteristics seems to appear: at lower bias the peak width is bigger than in a full depletion mode. This could be due at a bigger capacity, which influence the noise.

5.1.5 Measurements with radioactive sources

In order to completely validate the operation of the whole sensor¹, I have made some acquisitions with radioactive source, in particular I have used Fe55, Sr90, which is a β^- emettitor with electron endpoint at 0.546 MeV, and cosmic rays, which are supposed to be mostly MIP. In the acquisitions with Sr90 and cosmic rays, I specifically focused on the events whith charge sharing and with more hits than one per events, that are clusters.

The definition of cluster I chose is built only on the time of arrival of hit, in particular I established that all particles with the same timestamp belong to the same cluster. This obviously is a coarse requirement but it gave me the opportunity of using a simple and fast clustering algorithm, which is fine when the random coincidence probability is negligible. Defining R_1 and R_2 as the two events rate, and τ as the dead time of the detector, the random coincidence rate can be found:

$$R_{coinc} = R_1 \times R_2 \times \tau \quad (5.9)$$

As I am going to prove in the next section, the dead time strictly depends on the occupancy of the matrix, even through we can assume a dead time of $\sim 1 \mu\text{m}$, which corresponds to the mean dead time per pixel. However, if in an event a particle hit two different pixels producing a cluster, the total dead time simply doubles. Then, assuming a rate of noise of $\sim \text{Hz}$ on the whole matrix and being the mean rate of the , the random coincidence of two hits coming from Fe-noise, Sr-noise, CR-noise and noise-noise are respectively

In figure ?? I report the histograms of the number of pixels in the cluster and of the dimension of clusters, defined in terms of the max and min coordinates on the matrix as:

$$d = \sqrt{(y_{max} - y_{min})^2 + (x_{max} - x_{min})^2} \quad (5.10)$$

¹As I will explained in chapter ?? these measurements are foundamental also to be compared with the spectrum seen at the testbeam

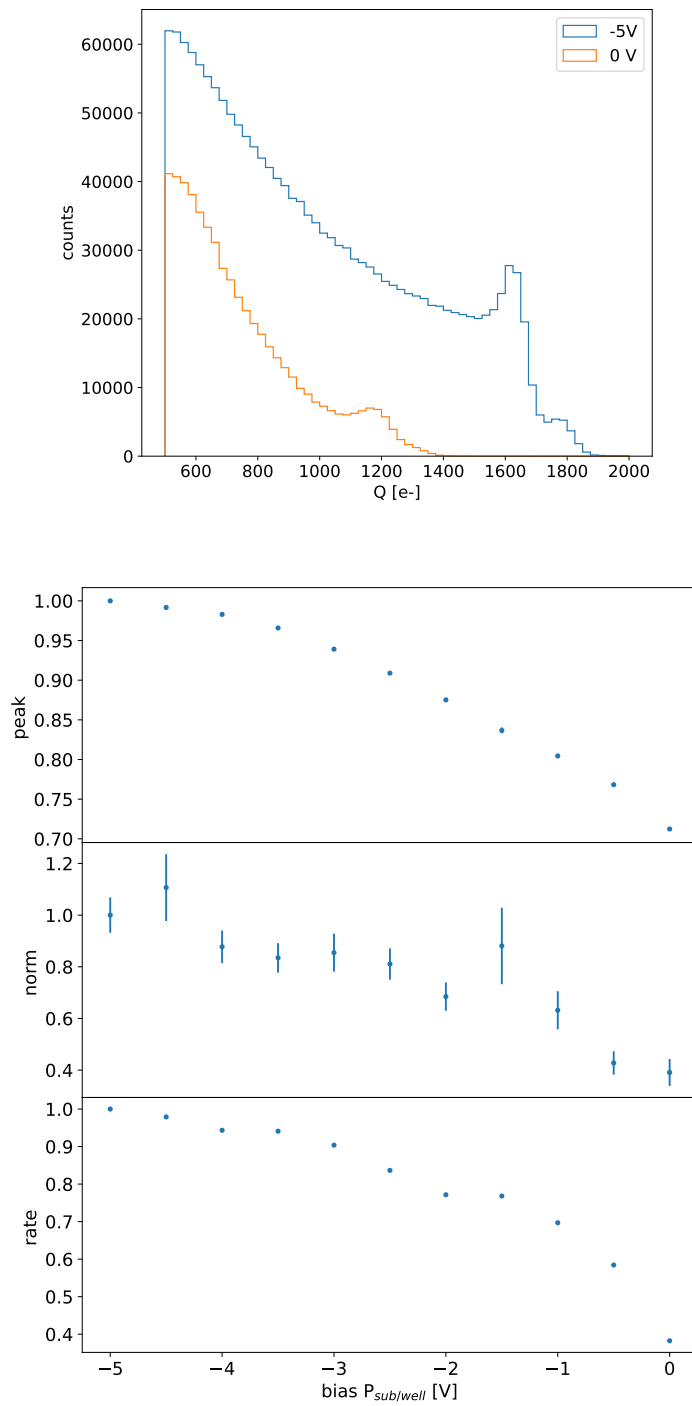


Figure 5.10: Two acquisition with the Fe55 source at different bias.

1220 quello che si nota è che lo Sr fa cluster più grandi mediamente, che arrivano anche a 22
 1221 hit.

1222 Below I have also attached a sample of hitmap of events produced by the three different
 1223 sources.

1224 • PLOT delle hit per cluster

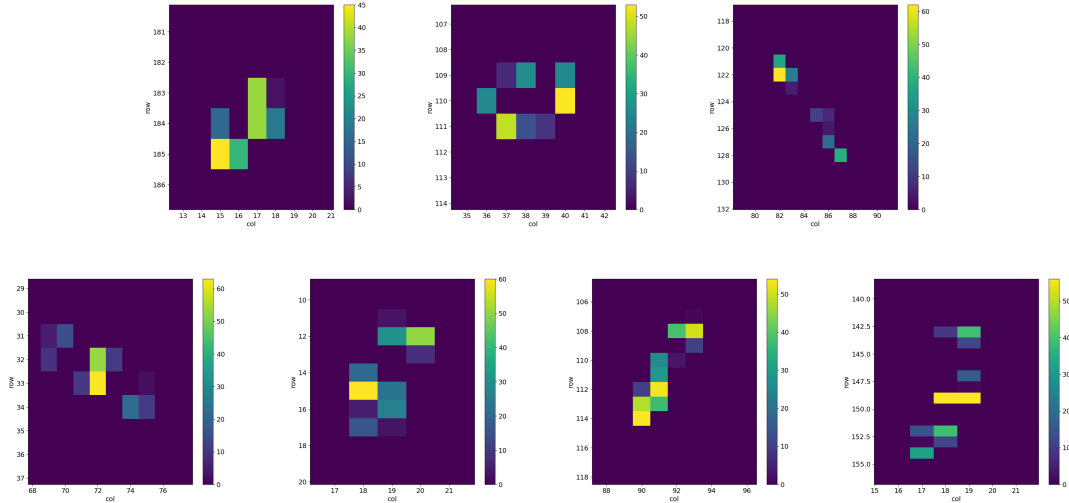


Figure 5.11

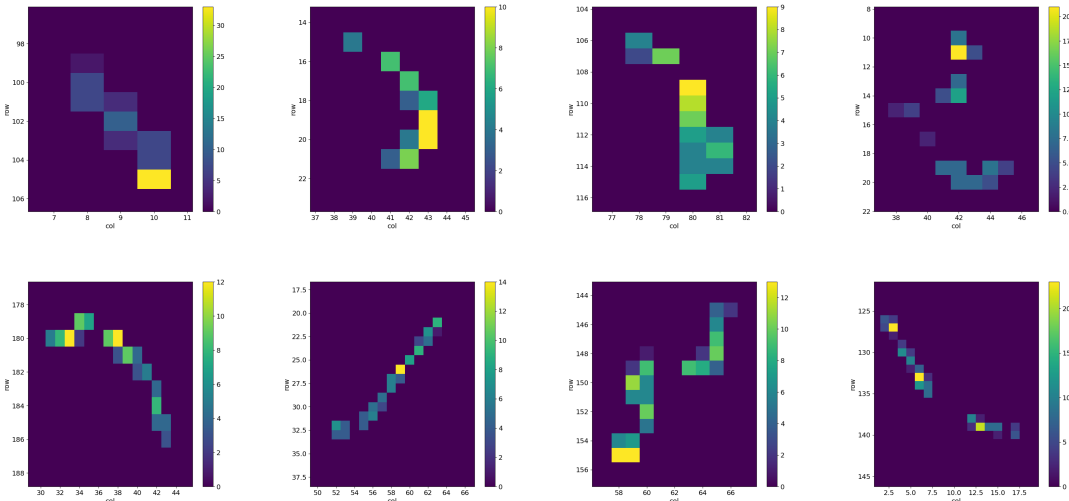


Figure 5.12

- 1225 • esempio di heatmap di cluster
- 1226 • sostituisci in carica in un file del ferro, guarda somma dei cluster, stessa cosa per Sr
1227 e MIP
- 1228 • Spiega che con il flavor HV abbiamo una perdita di segnale, fai vedere uno spettro
1229 di delle misure dell'8 marzo.
- 1230 The signal generated by electrons is similar to the one generated by minimum ionizing
1231 particle (MIPS) **dovrei mettere qualche conto per giustificare questa affermazione**, and the
1232 spectrum is expected to follow a Langau-Gauss distribution. **nelle acquisizioni dei CR ho**
1233 **selezionato solo i cluster, per tagliare via il rumore.**
- 1234 , looking at the cluster dimension and the cluster charge.

1235 **5.1.6 Dead time measurements**

1236 The hit loss is due to analog and digital pile up: the first one occurs when a new hit
1237 arrives during the pre-amplifier response, the second instead when the hit arrives while
1238 the information of the previous hit has not yet been transferred to the periphery. Since
1239 the pre-amplifier response has a characteristic time \sim ToT, the dead time τ_a introduced
1240 by it will be at most 1.6 μ s; using the IRESET and VRESET FE parameters the reset
1241 time can be lowered down, but a **IRESET, puoi diminuire il tempo di scarica ma deve**
1242 **comunque** Regarding the latter contribution instead, since only one hit at a time can
1243 be stored on the pixel's RAM, until the data have completed the path to get out, the
1244 pixel is paralyzed. Moreover since there is no storage memory included on TJ-Monopix1
1245 prototypes, the digital dead time τ_d almost corresponds to the time needed to transmit the
1246 data-packets off-chip.

1247 The exportation of data from pixel to the EoC occurs via a 21-bits data bus, therefore
1248 only one clock cycle is needed and the dead time bottleneck is rather given by the
1249 bandwidth of the serializer which transmits data off-chip from the EoC. In our setup the
1250 serializer operates at 40 MHz, thus to transmit a data packet (27-bit considering the ad-
1251 dition of 6 bits to identify the double-column at the EoC) at least 675 ns are needed. For
1252 what we have said so far, the R/O is completely sequential and therefore is expected a
1253 linear dependence of the reading time on the number of pixels to read:

$$\tau = 25 \text{ ns} \times (\alpha N + \beta) \quad (5.11)$$

1254 where α and β are parameters dependent on the readout chain setting.

1255 To test the linearity of the reading time with the number of pixels firing and to measure
1256 it, I have used the injection circuit which allows me choosing a specific hit rate: I made
1257 a scan injecting a fix number of pulses and each time changing the number of pixels
1258 injected. Indeed the injection mode allows fixing not only the amplitude of the pulse,
1259 which corresponds to the charge in DAC units, but also the time between two consecutive
1260 pulses (DELAY). The hit rate then corresponds to 25 ns/DELAY.

1261 Unfortunately a high random hit rate on the matrix cannot be simulated by the in-
1262 jection because of the long time (\sim ms) needed to set the pixel registers of the injection;
1263 then I was forced to specify at the start of the acquisition the pixels to inject on, and for
1264 convenience I chose those on a same column. In figure 5.13 is shown the dependence of
1265 the efficiency on the DELAY parameter in two different cases. For the 5 pixels example
1266 the efficiency goes down the 90% at a DELAY of \sim 185 clock counts, which corresponds
1267 to 4.625 μ s and to a rate of 216 kHz, while in the 10 pixels example, the efficiency goes
1268 under the 100% at \sim 380 clock counts, which corresponds to 9.5 μ s and to a rate of 105 kHz.
1269 **COME MAI SONO DIVERSE LE CURVE?** From the efficiency curves I have then looked
1270 for the time when the efficiency decreases. In figure 5.14(a) is shown the dead time per
1271 pixels as a function of N with different R/O parameters configuration, the meaning of
1272 which is explained in chapter 3.3. The default value suggested by the designer of the chip
1273 are reported in table 5.3; moving too much the readout parameters from the default ones,
1274 the readout does not work properly, and no hits can be read at all. The problem probably
1275 stays in the firmware setting of the readout which are specially fixed for our chip **Sul**
1276 **repositorio, nei commenti ci sono altri valori possibili per il FREEZE, ma avevamo detto**
1277 **che probabilmente sono relativi ai setting di altri chip.** Despite the single pixel reading
1278 time does not depend on the position on the pixel matrix, within a clock count which

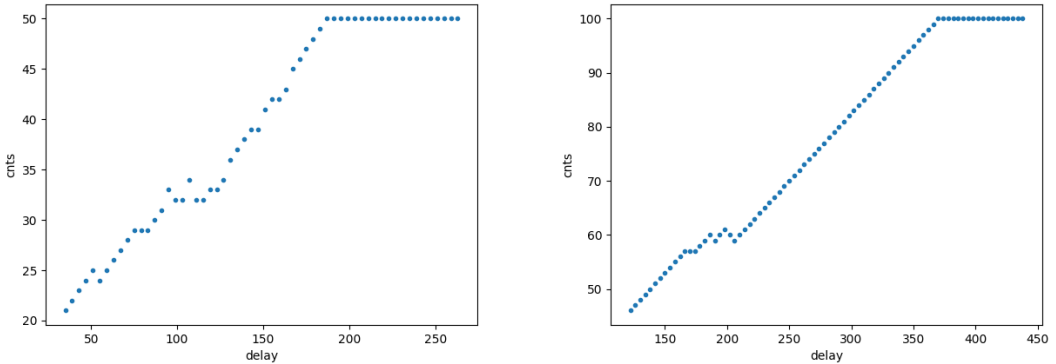


Figure 5.13: Efficiency vs the DELAY parameters. (a) I made a scan injecting 5 pixels with 50 pulses for each DELAY configuration and (b) 10 pixels with 100 pulses for each DELAY

Parameter	Value [DAC]	Value [μ s]
START_FREEZE	64	1.6
STOP_FREEZE	100	2.5
START_READ	66	1.65
STOP_READ	68	1.7

Table 5.3: Default configuration of the R/O parameters

is ~ 25 ns, and it is equal to 106 clock counts, since the τ_d critically depends on the pixel position on the matrix: in particular the reading sequence goes from row 224 to row 0, and from column 0 to column 112, making the pixel on the bottom right corner the one with the longest dead time.

Furthermore to test that there is no dependence of the digital readout time from the charge of the pulse, I have tried to change the amplitude of the pulse injected, but the parameters found were consistent with the default configuration ones. No difference in the α and β coefficients has been observed between the two cases. Referring to eq.5.11, the factor α is proportional to the difference (STOP_FREEZE - START_READ), while the offset β lies between 5 and 15 clock counts.

Per avere una misura veritiera del tempo morto e del hit loss si dovrebbe iniettare casualmente input events are produced by a random hit generator with a specified hit rate, hence following a Poisson distribution. Inoltre faccio notare che il tempo morto è così lungo perché c'è parallelizzazione e neppure un buffer (cosa tipicamente prevista quando li si inserisce nei rivaltori). Ad esempio Obelix, per l'upgrade di Belle2 avrà un buffer a fine matrice.

5.2 ARCADIA-MD1 characterization

Unfortunatly we have found out that the chip we received was not completely functional, then we have been able to make on it only a few electrical and software test. We have then verified the communication of the chip with the DAQ, testing the operations of the FPGA and the breakout board (BB). The problem occurs when the chip is biased, in

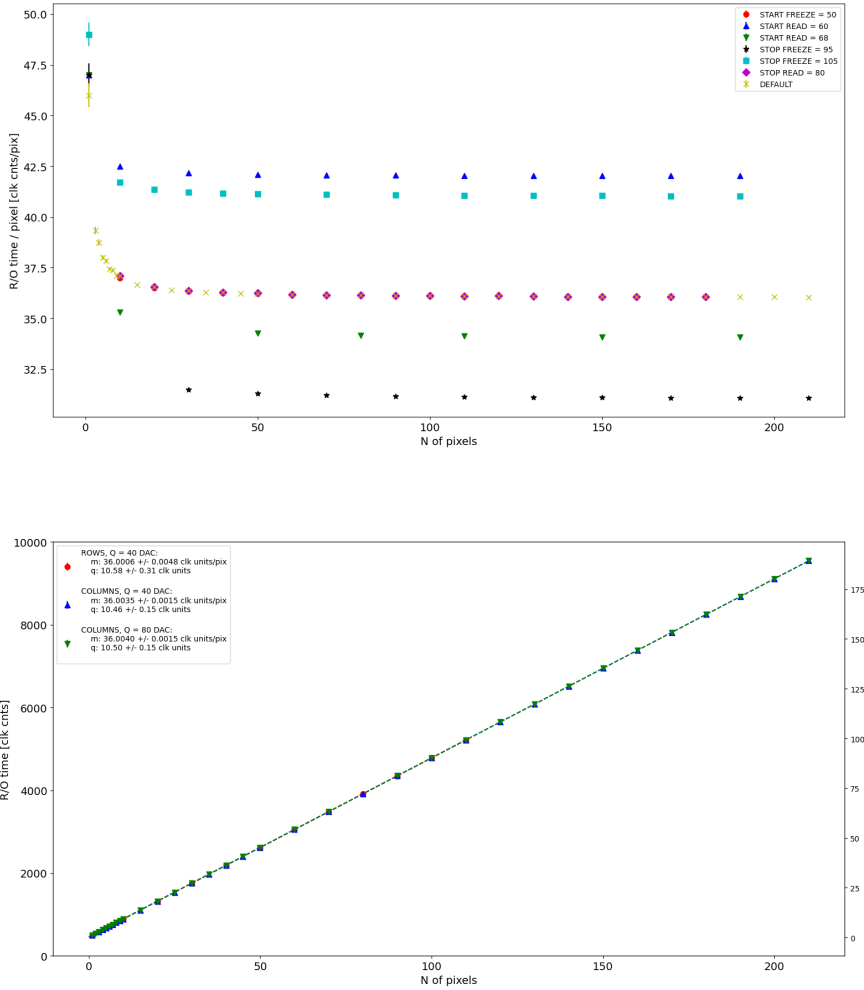


Figure 5.14: (a) Readout time per pixel as a function of the number of pixel injected obtained with different FE setup. (b) Readout time as a function of the number of pixels injected obtained injecting pulses with amplitude of 80 DAC (green), of 40 DAC on the same row (red) and on the same column (blue).

particular, when the HV voltage is lowered down 0 V, the sensor requires too much power and a too high current draw sets. We have discussed the problem with the designers of the chip whose helped us indentifying the motivation of the break: the chip has been glued using too much conductive tape and hence have a short-circuit between the sides and the back, which makes impossible the biasing. Unfortunately, since both the sensor and the FE require at least -10 V to work properly, no measurement was possible except the acquisition of the noise in the FE circuit.

We received then another chip, a minid2, that is a "mini demonstrator" from the second submission. The two chips have the same charateristics but the minid2 is smaller than the MD1, in particular it only have 32×512 pixels, instead of 512×512 . **scrivi il problema della prima sottomissione.**

An exhaustive characterization and testing of the new chip have been going on in the clean room on the INFN, and I am going to show here only some preliminary results. Up to now we used the injection circuit in order to make a threshold scan on a few pixels:

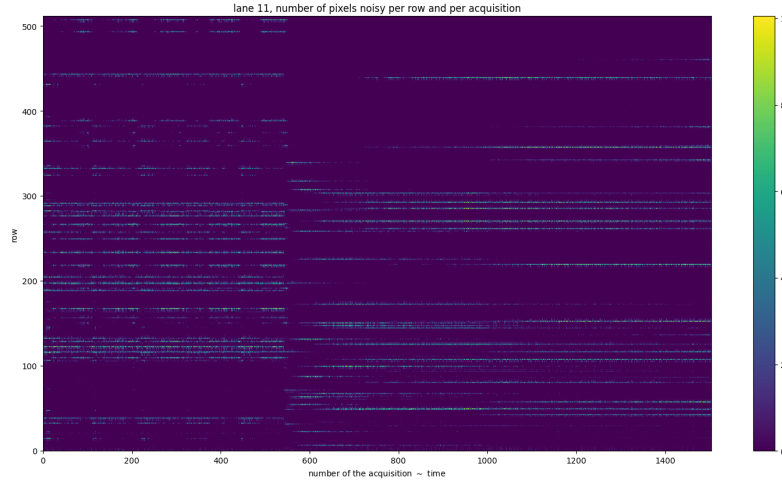


Figure 5.15: Noise in the front end circuit depending on the bias road across the matrix was recorded.

1314 differently from the TJ-Monopix1's characterization where we performed a scan changing
 1315 the injection charge of the pulse, with the minid2 we have instead changed the threshold
 1316 (whose register is VCASN) keeping the charge of the pulse fixed. For each threshold we
 1317 inject 100 pulses of amplitude 10 μ s. The dependence of the efficiency on the threshold for
 two pixels is shown in figure 5.16.

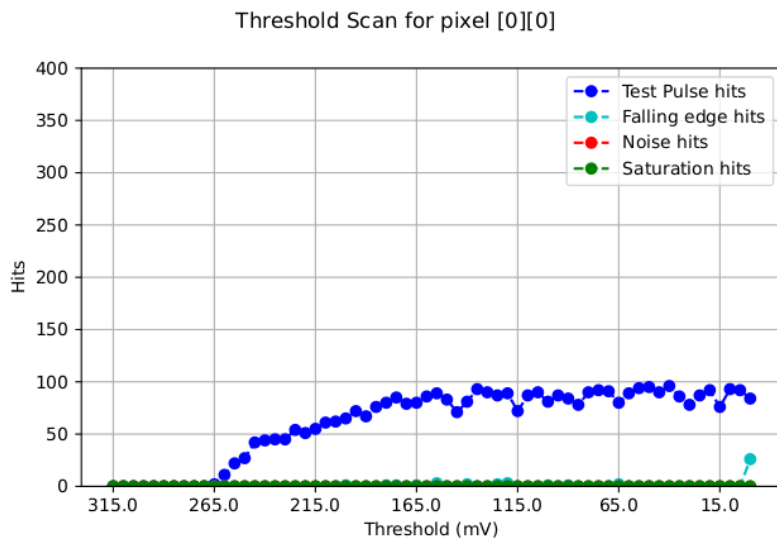


Figure 5.16

1318
 1319 Anche se il comportamento è globalmente ragionevole, con l'efficienza che sale quando
 1320 si abbassa la soglia, viene il sospetto che non stiamo polarizzando bene il sensore e il
 1321 FE dato che anche raggiunto i centi conteggi, si hanno delle fluttuazioni intorno a questo
 1322 valore. Inoltre notiamo che abbassando ulteriormente la soglia si osserva un aumento delle
 1323 hit, dovuto al fatto che si inizia a triggerare sul rumore.

1324 commenta sul fatto che non è stabile anche molto sopra la soglia. Forse è dovuto al
 1325 bias? oppure l'impulso ha qualche problema (non abbiamo settato la durata ecc..)? Che

1326 valore ha in elettroni?

1327 Substantial differences have been observed in both the efficiency and the threshold
1328 among the sections, with VCASN=40 DAC; this suggests that with this particular FE
1329 configuration there is a big threshold dispersion on the matrix. The hitmap of an ac-
1330 quisition with the Fe55 source is shown in figure 5.17: the whole MD1 matrix with only
1331 the bottom region (32 rows) working is represented in (a), while in (b) there is a zoomed
1332 bitmap. The rate seen within the region 8 (green region in the figure (a)) is compatible
1333 with the rate of the same radioactive source measured with TJ-Monopix1, that it \sim 3.3 kHz.
Looking to the Sr90 acquisitions (fig.5.18) many clusters and tracks can be immidiately

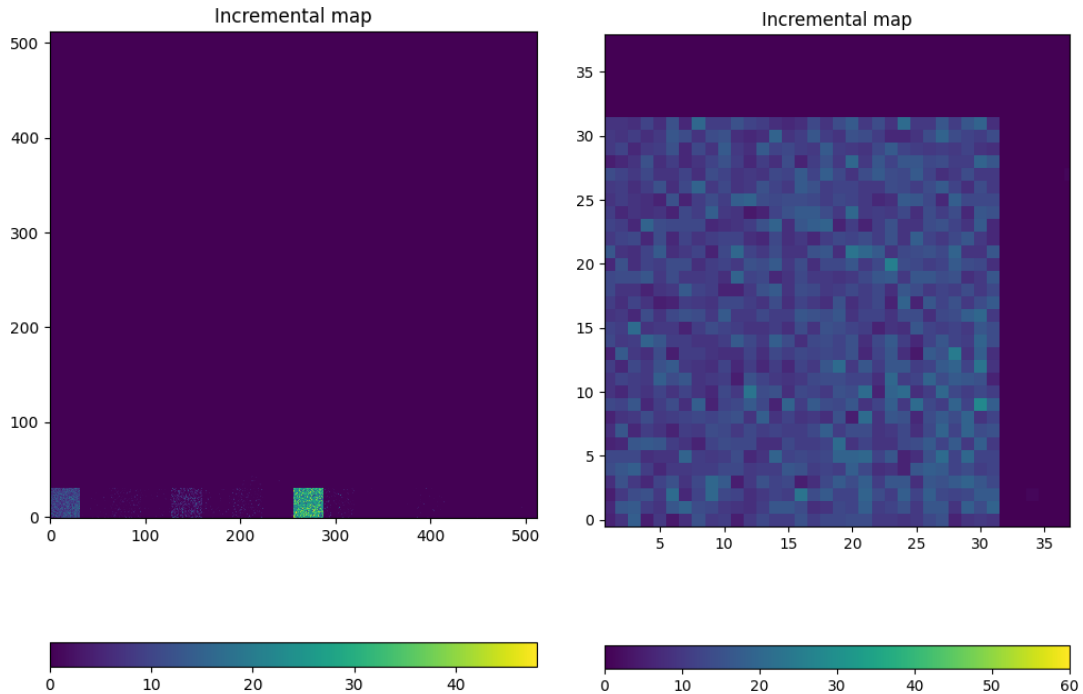


Figure 5.17: Fe55 acquisition with VCASN=40 DAC. (a) All the matrix 512×512 is plotted even if the minid2 has only the rows in range 0-32. (b) A zoom on the first section (col 0-32).

1334

1335 distinguished, confirming what observed with TJ-Monopix1.

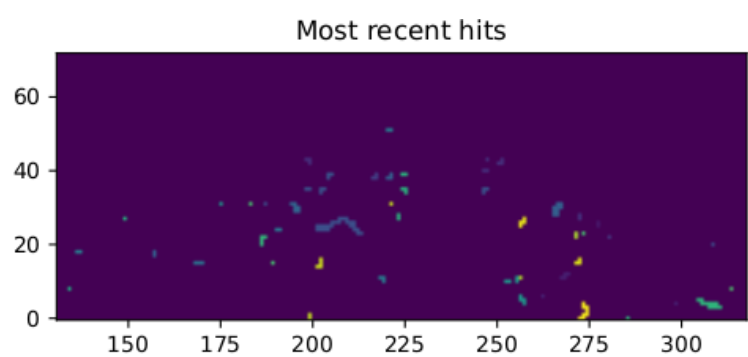


Figure 5.18: Sr90 acquisition with VCASN=40 DAC. The different colours are related with the time of arrival of the hits: in yellow the most recent hits, while in blue the old ones.

₁₃₃₆ **Chapter 6**

₁₃₃₇ **Test beam measurements**

₁₃₃₈ During August 2022 a testbeam took place in Santa Chiara hospital in Pisa, where a
₁₃₃₉ new accelerator designed for both medical research and R&D on FLASH-RT, and for this
₁₃₄₀ reason called "ElectronFlash", have been installed a few months ago. The motivation
₁₃₄₁ of the testbeam measurements were testing TJ-Mopopix1 at high dose rate with a focus
₁₃₄₂ on investigating the possibility of the application in radiotherapy. Despite this particular
₁₃₄₃ device does not seem fitting the requirements imposed for that application, especially
₁₃₄₄ regarding the readout time, the measurements have been useful since help us characterizing
₁₃₄₅ the setup for future advance, and also give us the possibility of a complete characterization
₁₃₄₆ of the chip.

₁₃₄₇ Given that in medical physics the dose is the standard parameter to characterize the
₁₃₄₈ beam, because of its obvious relation with the damage caused in the patient, I am going
₁₃₄₉ to explain the meaning of it by the point of view of the instrumentation. In fact, when
₁₃₅₀ interacting with measuring systems a more common and useful parameter is the rate or
₁₃₅₁ the fluence of particles. The conversion between the two quantity can be found thinking to
₁₃₅₂ the definition of dose: it is the concentration of energy deposited in tissue as a result of an
₁₃₅₃ exposure to ionizing radiation. Assuming total absorption of electrons in water, defined
₁₃₅₄ by law as the ordinary reference medium, the dose can be expressed as:

$$D[Gy] = \frac{NE[eV]}{\rho[g/cm^3]A[cm^2]x[cm]} \quad (6.1)$$

₁₃₅₅ After having applied the conversion of the energy from eV to J and noticed that $E/\rho x$
₁₃₅₆ roughly corresponds to the stopping power S of electrons in water, a simple estimation of
₁₃₅₇ the dose released in water is:

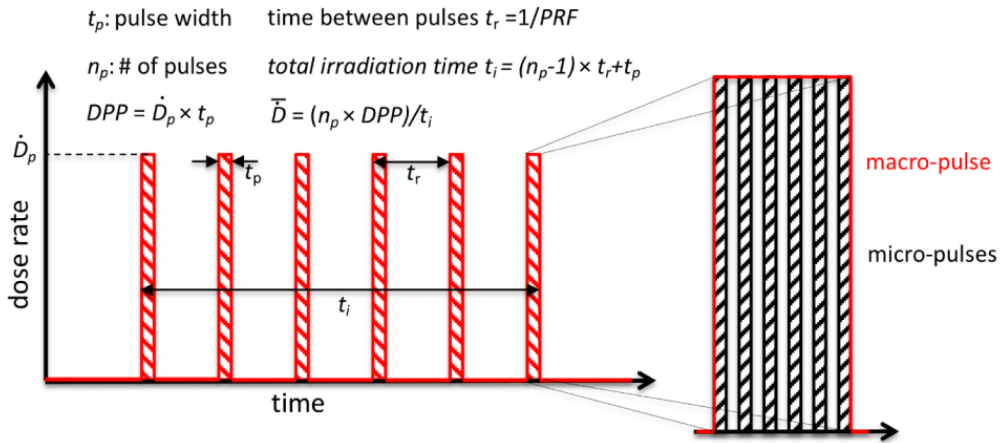
$$D[Gy] = 1.602 \cdot 10^{-10} N[cm^{-2}] S[MeV cm^2/g] \quad (6.2)$$

₁₃₅₈ **6.1 Apparatus description**

₁₃₅₉ In order to shield the outdoor from ionizing radiation the accelerator is placed in a bunker
₁₃₆₀ inside the hospital. The bunker has very thick walls of cementum and both the control
₁₃₆₁ units of the accelerator and of the detector were placed outside in a neighbor room.

₁₃₆₂ **6.1.1 Accelerator**

₁₃₆₃ The ElectronFlash accelerator is an electron Linear Accelerator (LINAC) with two energy
₁₃₆₄ configurations, at 7 MeV and 9 MeV, and it can reach ultra high intensity (40 Gy/pulse)



\bar{D}	Dose rate (mean dose rate for a multi-pulse delivery)	0.005-10000 Gy/s
\dot{D}	Intra pulse dose rate (dose rate in a single pulse)	$0.01-1 \times 10^6$ Gy/s
DDP	Dose in a single pulse	0.04-40 Gy
PRF	Pulse repetition frequency (number of pulses delivered per unit of time)	1-350 Hz
t_p	Pulse width	0.2-4 μ s
n	Number of pulses	single/pulse train

Table 6.1: The parameters that can actually be set by the control unit are the PRF, DDP, t_p and n (in particular singular irradiation or pulse train), while the other changes consequently.

keeping the possibility of accessing many different beam parameters and changing them independently from each other, a characteristic that makes it almost unique worldwide and which is fundamental for research in FLASH-RT, both for the medical aspects¹ and for the studies on detectors. The accelerator implements the standard beam structure used in RT with electrons (fig. 6.1), that is a macro pulse divided in many micropulses; the parameters used to set the dose and their range of values settable by the control unit is reported in table 6.1.

The accelerator is also provided of a set of triod cannons ~ 1.2 m long and with diameters in range from 1 cm to 12 cm and a collimator that can be used as beam shaper to produce a squircle shape. The triode, which is made by plexiglass, must be fix to the gun during the irradiation and is needed for producing, via the scattering of electrons with it, an uniform dose profile (fig.6.2) which is desired for medical purpose.

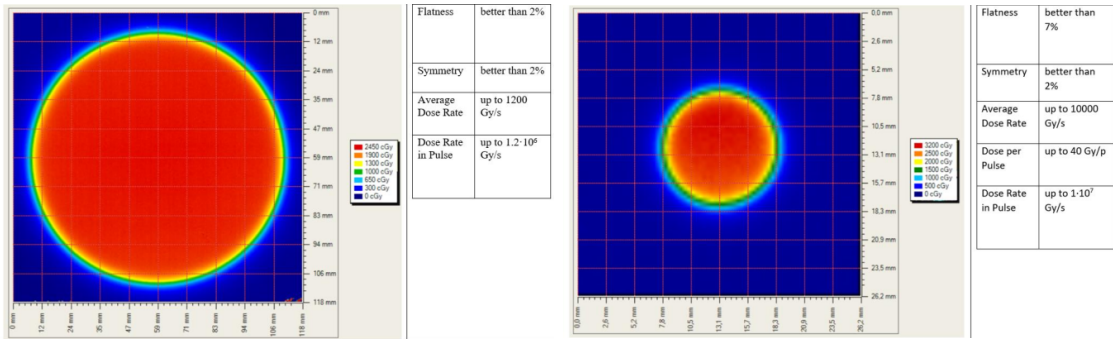


Figure 6.2: Two example of x-y isodose curves for two different triodes, 10 cm and 1 cm respectively, reported by the producer in the manual with the specific of the accelerator (S.I.T. - Sordina IORT Technologies S.p.A.). With the smaller collimator the dose rate in pulse is comparatively higher.

1376

6.1.2 Mechanical carriers

1377 The tested detector consists in one chip, the Device Under Test (DUT), mounted on a board and connected to FPGA with same arrangement of figure 6.5. These boards have been positioned vertically in front of the triode on a table specifically built for the testbeam. The tree board have been enclosed in a box of alluminium with a window on the DUT and with the required holes at the side to enable the biasing via cables and the connection with the DAQ provided via ethernet cable. A trigger signal coming from the control unity and synchronized with the pulses emitted from the beam has been also sent to the FPGA. This digital signal cannot be considered a real trigger, since the TJ-Monopix1 prototype has been designed to be triggerless, but its Time of Arrival (ToA) had allowed the reconstruction of the correct timing during the analysis.

1378 In order to shield the sensor from the whole particles emitted from the gun, two 1389 alluminium collimators have been fabricated: one has been positioned at the triode exit 1390 while the other in front of the DUT. The collimators are $t=32$ mm thick and have a 1391 diameter d equal to 1 mm: assuming a beam divergence bigger than $d/t=1/32 = 1.8^\circ$, 1392 which is the case, the collimator at the triode output was supposed to work as a point 1393 source and to reduce the rate on the DUT of a factor at least $4 \cdot 10^{-4}$. The second one,

¹For example, it is not yet really clear the dependence of the efficacy of the FLASH effect on the whole beam parameters

1394 being near the DUT, was instead supposed to shield the sensor from the electrons which
1395 have passed the first one, except for a region of 1 mm^2 configurable using [come si chiamano](#)
[quei cacciavitini per settare la posizione?](#) sliding trimmer?.

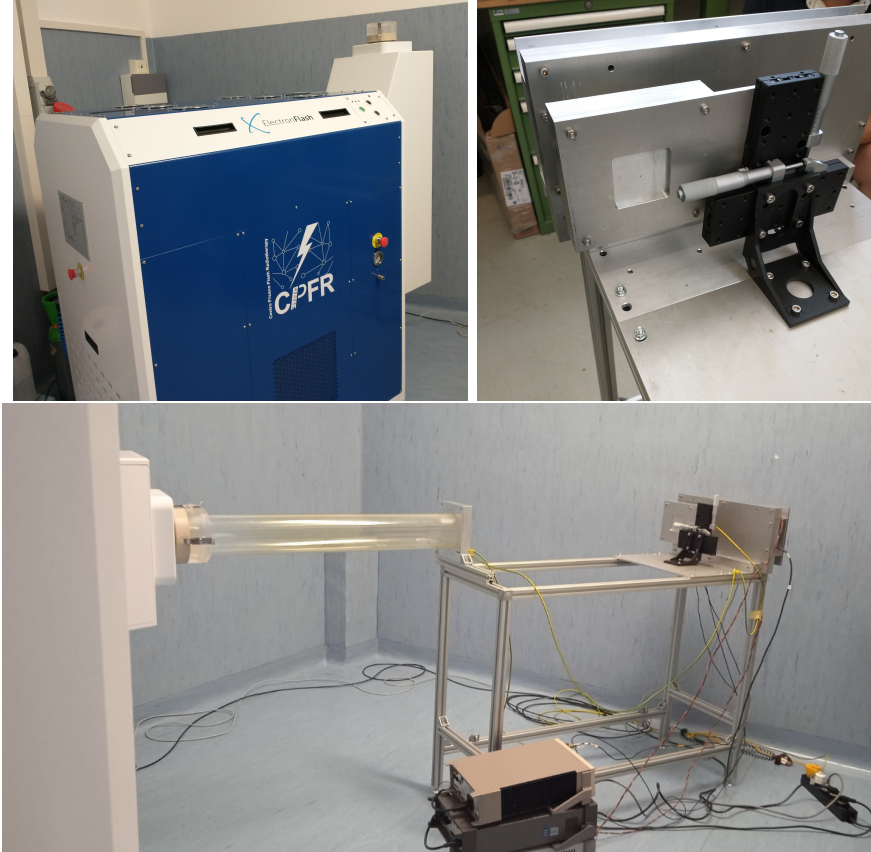


Figure 6.3: Experimental set up. (a) ElectronFlash accelerator: a rotating gantry allows the gun orientation from 0° to 90° (horizontal /vertical). (b) Collimator and DUT box. (c) Whole structure mounted: we used the 10 cm diameter and 1.2 m long triode; the DUT which is in the box behind the two collimators is connected to the power supply units.

1396

1397 6.2 Measurements

1398 Because of the dead time of TJ-Monopix1 it is not possible resolving the bunch sub-
1399 structure and almost no one pixel can read more than a hit per bunch. I recall, indeed,
1400 that the dead time per pixel depends on the location on the priority chain for the readout
1401 and for each pixel $\lesssim 1\text{ }\mu\text{s}$ (fig. 6.5) are needed; therefore only a few pixels at the top of
1402 the priority chain (at the upper left of the matrix) can fire a second time, since they in
1403 principle can be read the first time before the end of the pulse (assuming a pulse duration
1404 in $2\text{ }\mu\text{s}-4\text{ }\mu\text{s}$) and then can be hit again.

1405 Since resolving the single electron track is impossible, a way this sensor could be used
1406 in such context is reducing its efficiency and taking advantage of the analog pile up and
1407 of the linearity of the analog output (ToT), in order to see a signal produced not by the
1408 single particle but by more electrons. Reducing the efficiency and the sensibility of the
1409 sensor is essential in order to decrease the high charge signal produced in the epitaxial
1410 layer: if the sensor is completely depleted the collection efficiency is closer to 1% and if the

whole charges produced by a MIP, $80 \text{ e-}/\mu\text{m}$ about, are collected, the saturation limit is soon reach. Then a condition where there is a partial recombination of the center electron-hole created in the bulk is desiderable. On the other hand, the smaller the output signal value and the higher the rate the detector can cope with: indeed, the rollover constitutes a limit for the usage of the analog output. With the standard configuration of the FE parameters and the epitaxial layer completely depleted, a MIP produces a ToT out of range of representation of 6-bit; so as to obtain smaller output signals one can operate on the reduction of the gain of the preamplifier or on the pulse velocity of returnig to the baseline. Recalling the results in section 5.1.4, I have shown that concerning the PMOS flavor 1, reducing the bias from -6 V to 0 V brings a reduction of efficiency down to 40 %, and a reduction in the gain of a factor $\sim 1/3$, while the reduction of the gain of the preamplifier allows a reduction of circa 10, ma da controllare.

In order to taking advantage of the analog pile up and integrating the charge, for semplicity assume of two electrons, the second one must hit the pixel before the ToT goes under the threshold. The general condition is then $\overline{\Delta T} < \overline{ToT}$, but if a high $P_\mu(n \geq 1)$ is required, a lower $\overline{\Delta T}$ may be desired:

$$P(n \geq 1) = \sum_{n=1}^{\infty} \frac{e^{-\mu} \mu^n}{n!} = 1 - P(0) = 1 - e^{-\mu} \quad (6.3)$$

$$\mu = \frac{\overline{ToT}}{\overline{\Delta T}} \quad (6.4)$$

If a $P_\mu(n \geq 1) = 99\%$ then the $\overline{\Delta T}$ must be $\sim 0.22 \overline{ToT}$. The ToT is in range [0,64] but since the rollover must be avoided, the \overline{ToT} must be lower than 32, and then the minimum rate on the pixel must be 1.25 MHz.

During the testbeam many runs have been performed, spanning the energy, the dose per pulse and the four possible configurations with/without the collimators. We have used the PMOS flavor 1 in the standard configuration: we have biased the PWELL and PSUB at -6 V and set the standard default FE parameters reported in table ???. During all the acquisitions we have used pulses with t_p of 4 μm and with the smallest PRF settable, which is 1 Hz, in order to start in the most conservative working point exluding the digital pile up of events from different bunch: even if the whole matrix turns on and there are 25000 hits, the total readout time corresponding to 25 ms is still lower than the time between two consecutive pulses. The readout starts with the trailing edge of the first pulse going down the threshold, $\sim 50 \text{ clk} = 1.25 \mu\text{s}$ after this moment the FREEZE signal is sent to the whole matrix, and the trasmittion of the data to the EoC begins. The hits read are the ones whose TE occurred during the 50 clk counts; the ones, instead, whose TE occur during the FREEZE are stored in the pixel memory and read during a second readout. Obviously since the readout of the fist sub-pulse finishes much later than the bunch ends up, each pixel can be store only one hit. An example of the two sub-pulses is shown in figure ???: in the acquisition we injected 5 pulses with both the collimators mounted on the table. Looking at the spectrum si vede che lo spettro del secondo pulse ha una coda più lunga a destra: questo è dovuto al fatto che le hit con tot lungo hanno il TE che cade durante il FREEZE e quindi vengono lette durante il secondo impulso. On the other hand the 2D histograms, being uniform and not showing disomogenities, suggest that the collimators do not shield all the particles: this was due to a photon background higher than expected.

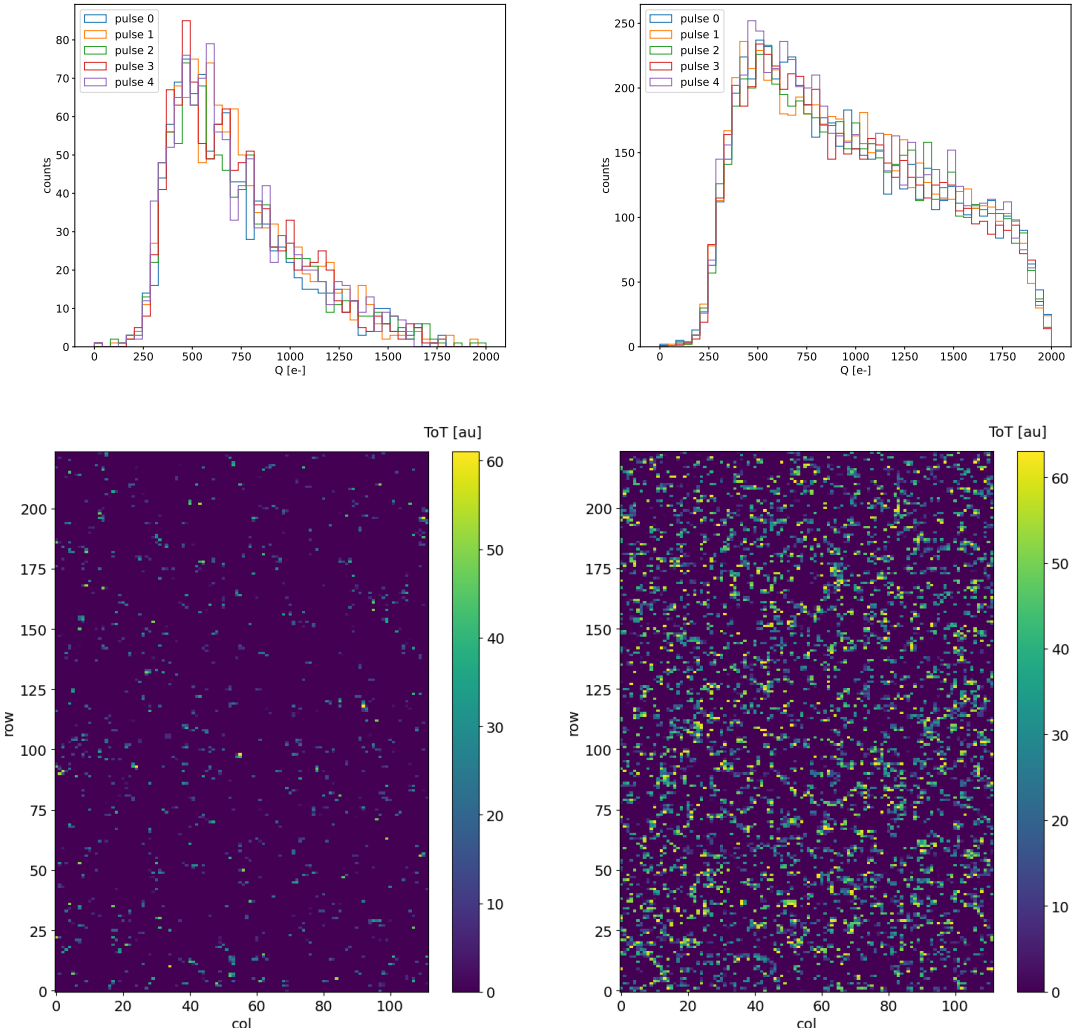


Figure 6.4: Acquisition with both the collimators: 5 pulses at DDP=0.07 Gy. (a) Spectrum of the charge released in the sensor: to apply the conversion I used the information found in the previous chapter. (b) 2D histogram of the ToT of the hits arrived in the sub-pulses.

1453 When we have put aside the collimators, instead, the fluence was too high that the whole
 1454 matrix turns on in 50 clk counts; then the 2 pulses substructure no more appears (fig. 6.6).
 1455 **CONTROLLA PERCHÈ PORTEBBE ESSERE UNA CAZZATA**

1456 The high background we saw although the collimators were mainly produced by elec-
 1457 trons Bremsstrahlung during the transition through the alluminium collimators. **Mancano:**

- 1458 • plot n di eventi che vedo con le diverse configurazioni
 1459 • confronta con misure dello spettro che vediamo senza e con collimatori.

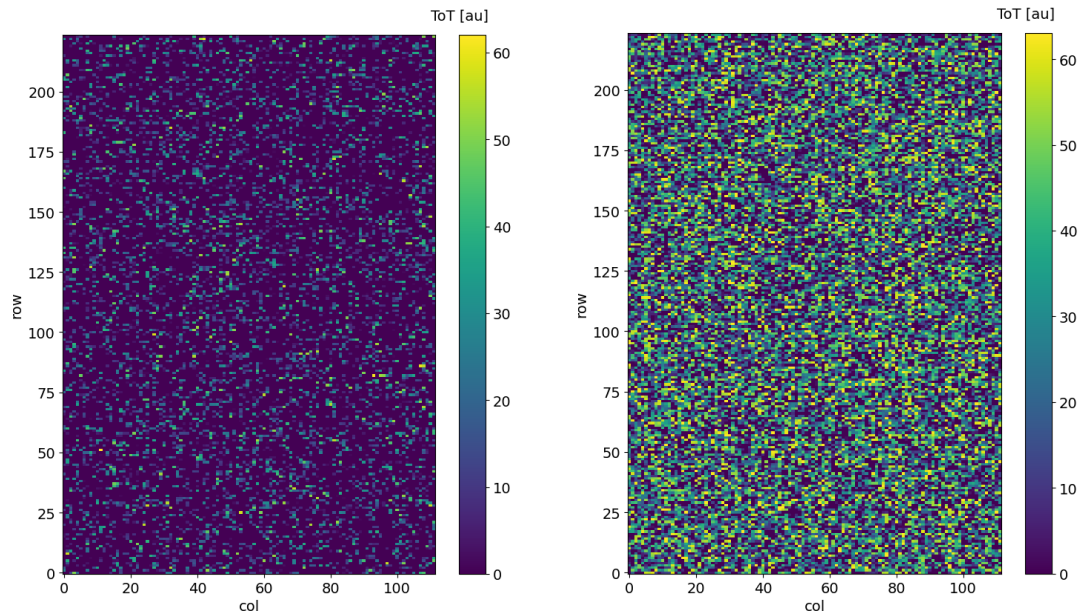


Figure 6.5: Acquisition with both the collimators: 5 pulses at DDP=0.6 Gy. 2D histogram of the ToT of the hits arrived in the sub-pulses. Compared with the previous maps, since the DDP is much higher, more pixels turn on.

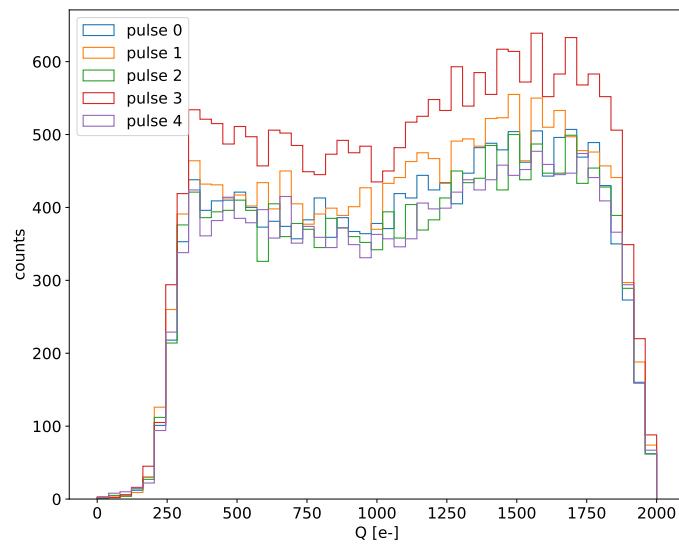


Figure 6.6: Acquisition without any collimator: 5 pulses at DDP=0.04 Gy.

¹⁴⁶⁰ Bibliography

- ¹⁴⁶¹ [1] W. Snoeys et al. “A process modification for CMOS monolithic active pixel sensors
¹⁴⁶² for enhanced depletion, timing performance and radiation tolerance”. In: (2017).
¹⁴⁶³ DOI: <https://doi.org/10.1016/j.nima.2017.07.046>.
- ¹⁴⁶⁴ [2] H. Kolanoski and N. Wermes. *Particle Detectors: Fundamentals and Applications*.
¹⁴⁶⁵ OXFORD University Press, 2020. ISBN: 9780198520115.
- ¹⁴⁶⁶ [3] E. Mandelli. “Digital Column Readout Architecture for 10.1109/NSSMIC.2009.5402399
¹⁴⁶⁷ the ATLAS Pixel 0.25 um Front End IC”. In: (2002).
- ¹⁴⁶⁸ [4] M. Garcia-Sciveres and N. Wermes. “A review of advances in pixel detectors for
¹⁴⁶⁹ experiments with high rate and radiation”. In: (2018). DOI: <https://doi.org/10.1088/1361-6633/aab064>.
- ¹⁴⁷¹ [5] C. Marinas. “The Belle-II DEPFET pixel detector: A step forward in vertexing in the
¹⁴⁷² superKEKB flavour factory”. In: (2011). DOI: [doi:10.1016/j.nima.2010.12.116](https://doi.org/10.1016/j.nima.2010.12.116).
- ¹⁴⁷³ [6] J. Baudot. “First Test Results Of MIMOSA-26, A Fast CMOS Sensor With Inte-
¹⁴⁷⁴ grated Zero Suppression And Digitized Output”. In: (2010). DOI: [doi:10.1109/NSSMIC.2009.5402399](https://doi.org/10.1109/NSSMIC.2009.5402399).
- ¹⁴⁷⁶ [7] A. Dorokhov. “High resistivity CMOS pixel sensors and their application to the
¹⁴⁷⁷ STAR PXL detector”. In: (2011). DOI: [doi:10.1016/j.nima.2010.12.112](https://doi.org/10.1016/j.nima.2010.12.112).
- ¹⁴⁷⁸ [8] Giacomo Contin. “The STAR MAPS-based PiXeL detector”. In: (2018). DOI: <https://doi.org/10.1016/j.nima.2018.03.003>.
- ¹⁴⁸⁰ [9] Nolan Espplen. “Physics and biology of ultrahigh dose-rate (FLASH) radiotherapy:
¹⁴⁸¹ a topical review”. In: (2020). DOI: <https://doi.org/10.1088/1361-6560/abaa28>.
- ¹⁴⁸² [10] Fabio Di Martino et al. “FLASH Radiotherapy With Electrons: Issues Related to
¹⁴⁸³ the Production, Monitoring, and Dosimetric Characterization of the Beam”. In:
¹⁴⁸⁴ *Frontiers in Physics* 8 (2020). ISSN: 2296-424X. DOI: [10.3389/fphy.2020.570697](https://doi.org/10.3389/fphy.2020.570697).
¹⁴⁸⁵ URL: <https://www.frontiersin.org/articles/10.3389/fphy.2020.570697>.
- ¹⁴⁸⁶ [11] M. Dyndal et al. “Mini-MALTA: Radiation hard pixel designs for small-electrode
¹⁴⁸⁷ monolithic CMOS sensors for the High Luminosity LHC”. In: (2019). DOI: <https://doi.org/10.1088/1748-0221/15/02/p02005>.
- ¹⁴⁸⁹ [12] M. Barbero. “Radiation hard DMAPS pixel sensors in 150 nm CMOS technology
¹⁴⁹⁰ for operation at LHC”. In: (2020). DOI: <https://doi.org/10.1088/1748-0221/15/05/p05013>.
- ¹⁴⁹² [13] K. Moustakas et al. “CMOS Monolithic Pixel Sensors based on the Column-Drain
¹⁴⁹³ Architecture for the HL-LHC Upgrade”. In: (2018). DOI: <https://doi.org/10.1016/j.nima.2018.09.100>.

- 1495 [14] I. Caicedo et al. “The Monopix chips: depleted monolithic active pixel sensors with
1496 a column-drain read-out architecture for the ATLAS Inner Tracker upgrade”. In:
1497 (2019). DOI: <https://doi.org/10.1088/1748-0221/14/06/C06006>.
- 1498 [15] D. Kim et al. “Front end optimization for the monolithic active pixel sensor of the
1499 ALICE Inner Tracking System upgrade”. In: *JINST* (2016). DOI: doi:10.1088/
1500 1748-0221/11/02/C02042.
- 1501 [16] L. Pancheri et al. “A 110 nm CMOS process for fully-depleted pixel sensors”. In:
1502 (2019). DOI: <https://doi.org/10.1088/1748-0221/14/06/c06016>.
- 1503 [17] L. Pancheri et al. “Fully Depleted MAPS in 110-nm CMOS Process With 100–300-
1504 um Active Substrate”. In: (2020). DOI: 10.1109/TED.2020.2985639.